

**EXPERIMENTAL AND NUMERICAL EVALUATION OF THE
PERFORMANCE OF A HIGH-SPEED CENTRIFUGAL COMPRESSOR
AT OFF-DESIGN CONDITIONS**

by

William Joseph Brown

A Thesis

Submitted to the Faculty of Purdue University

In Partial Fulfillment of the Requirements for the degree of

Master of Science in Mechanical Engineering



School of Mechanical Engineering

West Lafayette, Indiana

December 2020

**THE PURDUE UNIVERSITY GRADUATE SCHOOL
STATEMENT OF COMMITTEE APPROVAL**

Dr. Nicole Key, Chair

School of Mechanical Engineering

Dr. Terrence Meyer

School of Mechanical Engineering

Dr. Guillermo Paniagua

School of Mechanical Engineering

Approved by:

Dr. Nicole Key

“There’s theory and then there’s application. They don’t always jibe”

- Geordi La Forge

ACKNOWLEDGMENTS

First and foremost, I would like to say thank you to my advisor, Dr. Nicole Key, not only for her guidance and support, but also for providing me with the opportunity to conduct research in a world class facility where I have learned so much over the course of the last two years. I would like to thank my committee members, Dr. Terrence Meyer, and Dr. Guillermo Paniagua for their time and feedback on my thesis. Technical support and guidance provided by Grant Malicoat, Rob McGuire, Toby Lamb, and Andreas Schmid has made it possible to keep this project operational and helped all of the students in the lab to achieve their academic goals.

I would like to thank Honeywell Aerospace for their financial and technical support of the project, and more specifically, I would like to thank Darrell James, Andrew Loudenbeck, and Mark De La Torre for their support and advice during the course of my research, without which, this thesis would not have been possible.

I am very appreciative to all of the members of the lab, who have made it a fun work environment and from whom I have learned a great deal during my time here. I would like to thank the other members of the Honeywell project: Lou, Matt, Trey, and Evan, who have been the best teammates and friends I could have hoped for. I would like to thank Matt in particular, as his work developing a computational model for our project provided me with insights that were critical to my research.

Last, but certainly not least, I would like to thank my family for their continued support throughout my education and for listening to me talk about my research when I'm sure they had little interest. I would like to thank my parents, brother, and grandparents whose support has allowed me to achieve my goals.

TABLE OF CONTENTS

LIST OF TABLES	8
LIST OF FIGURES	9
NOMENCLATURE	14
ABSTRACT.....	16
1. INTRODUCTION	18
1.1 Motivation.....	18
1.2 Transonic Impeller Aerodynamics.....	19
1.2.1 Tip Leakage Flow	20
1.2.2 Boundary Layers in Turbomachinery	21
1.2.3 Blockage	22
1.2.4 Inducer Shock Structure	24
1.2.5 Shock Interaction with Tip Leakage Vortex.....	25
1.2.6 Shock Interaction with Suction Surface Boundary Layer	28
1.2.7 Effect of Transonic Operation on Performance.....	30
1.2.8 Disturbance Propagation in the Impeller	31
1.3 Research Objectives.....	32
2. EXPERIMENTAL SETUP AND METHODOLOGY	34
2.1 Purdue SSCC Research Facility.....	34
2.2 SSCC Facility Instrumentation	36
2.2.1 Steady Instrumentation	36
2.2.2 Health Monitoring	39
2.2.3 Fast Response Instrumentation.....	39
2.3 Experimental Procedures	41
2.3.1 Steady Data.....	41
2.3.2 Transient Data.....	42
2.4 Computational Model	43
3. DATA PROCESSING.....	45
3.1 Performance Data Analysis.....	45
3.1.1 Mass Flow Rate	45

3.1.2	Total Pressure Ratio.....	46
3.1.3	Efficiency.....	46
3.1.4	Impeller Exit Conditions.....	46
3.2	Unsteady Data Processing.....	48
3.2.1	Isentropic Relative Shroud Mach Number	48
3.2.2	Quantification of Kulite Signal Unsteadiness.....	49
3.2.3	Kulite Signal Processing for Sweeps.....	49
3.2.4	Phase Shift of Impeller LE Kulite	50
3.2.5	Ensemble Average of Kulite Data	52
4.	EXPERIMENTAL RESULTS	53
4.1	Transient Data.....	53
4.1.1	Unsteady Data.....	53
4.1.2	Transient Compressor Performance	64
4.2	Steady Data.....	67
4.2.1	Inducer Relative Mach Number.....	67
4.2.2	Steady State Performance	69
4.2.3	Unsteady Pressure Measurements	71
4.2.4	Component Stability	80
4.2.5	Effect of Shock Formation on Tip Clearance Sensitivity	82
4.2.6	Inducer Flow Field.....	84
4.2.7	Summary of Experimental Results	93
5.	NUMERICAL RESULTS	95
5.1	Comparison with Experimental Results.....	95
5.1.1	Impeller Performance	95
5.1.2	Impeller Meridional Shroud Static Pressure.....	98
5.1.3	Inducer Shroud Static Pressure	100
5.2	Impeller Flow Structure	102
5.2.1	Tip Leakage Vortex	103
5.2.2	Blockage	106
5.2.3	Shock Location	112
5.2.4	Shock Interactions	115

6. CONCLUSION.....	120
6.1 Experimental Data	120
6.1.1 Transient Data.....	120
6.1.2 Steady State Data.....	121
6.2 Numerical Results.....	122
6.3 Recommendations for Future Work.....	124
6.3.1 Experimental Suggestions	124
6.3.2 Numerical Suggestions	125
APPENDIX.....	126
REFERENCES	129

LIST OF TABLES

Table 2.1 Summary of steady performance instrumentation	38
Table A.1 Values of coefficients and exponents used in the final correlation	127

LIST OF FIGURES

Figure 1.1 Effect of wall curvature and rotation on boundary layer stability [5]	22
Figure 1.2 Cartoon representation of flow field in a blade passage with low momentum region near the shroud shown in red	23
Figure 1.3 Inducer leading edge shock and interactions	25
Figure 2.1 Axisymmetric inlet plenum with flow spreader and honeycomb	35
Figure 2.2 Purdue SSCC experimental testing facility	36
Figure 2.3 SSCC flowpath instrumentation locations	37
Figure 2.4 SSCC flowpath nomenclature	37
Figure 2.5 Performance data acquisition setup	39
Figure 2.6 Impeller shroud static pressures and meridional Kulites	40
Figure 2.7 Unsteady data acquisition setup	41
Figure 2.8 Compressor total pressure map showing constant throttle survey lines	42
Figure 2.9 Compressor total pressure map showing constant throttle sweeps	43
Figure 2.10 Computation domain used for numerical analysis of compressor stage	44
Figure 3.1 Example of a Campbell diagram showing discrete responses along the 2 nd and 3 rd engine order lines	50
Figure 3.2 Impeller LE Kulite shift	51
Figure 3.3 Illustration of LE Kulite signal shift for one revolution	52
Figure 4.1 Filtered Kulite response during acceleration sweep along mid-choke line from 40% to 100% Nc	54
Figure 4.2 Filtered Kulite response during deceleration sweep along mid-choke line from 100% to 40% Nc	54
Figure 4.3 Filtered Kulite response during acceleration sweep along the op-line from 40% to 100% Nc	55
Figure 4.4 Velocity triangles at the inducer for low (left) and high (right) loading conditions	56
Figure 4.5 Temperature vs entropy curve for Rayleigh flow	57
Figure 4.6 Cartoon of heat transfer through the shroud into the impeller inlet	58
Figure 4.7 Campbell diagram of impeller leading edge Kulite signal for a mid-choke sweep acceleration	59

Figure 4.8 Campbell diagram of Kulite downstream of inducer for mid-choke sweep	59
Figure 4.9 Variance of filtered impeller shroud Kulite signals at various meridional locations for acceleration sweep along mid-choke throttle line	61
Figure 4.10 Variance of filtered impeller shroud Kulite signals at various meridional locations for deceleration sweep along mid-choke throttle line	61
Figure 4.11 Ratio of flow temperature at impeller leading edge to inlet total temperature for acceleration sweep along mid-choke throttle line.....	62
Figure 4.12 Ratio of flow temperature at impeller leading edge to inlet total temperature for deceleration sweep along mid-choke throttle line	63
Figure 4.13 Comparison of impeller leading edge temperature ratio for acceleration sweeps along mid-choke and op-line throttle settings.....	64
Figure 4.14 Impeller efficiency during acceleration sweep along mid-choke throttle line .	66
Figure 4.15 Impeller total pressure ratio during acceleration sweep along mid-choke throttle line.....	66
Figure 4.16 Slope of impeller total pressure ratio for acceleration sweep along mid-choke throttle line	67
Figure 4.17 Isentropic relative Mach number at various locations in the inducer for the mid-choke survey	68
Figure 4.18 Isentropic relative Mach number at various locations in the inducer for the op-line survey	69
Figure 4.19 Impeller Isentropic efficiency for mid-choke throttle line survey where the data points are colored by the leading edge temperature ratio	70
Figure 4.20 Impeller TPR for mid-choke throttle line survey	71
Figure 4.21 Variance of filtered Kulite signal for mid-choke throttle line survey	72
Figure 4.22 Waterfall of impeller leading edge Kulite frequency spectra for mid-choke throttle line survey showing frequency content up to 35 times the rotational frequency	73
Figure 4.23 Waterfall of impeller leading edge Kulite frequency spectra for mid-choke throttle line survey showing frequency content up to 18 times the rotational frequency	74
Figure 4.24 Waterfall of impeller leading edge Kulite frequency spectra for mid-choke throttle line survey showing frequency content up to 10 times the rotational frequency	74
Figure 4.25 Waterfall of vaneless space Kulite frequency spectra for mid-choke throttle line survey showing frequency content up to 35 times the rotational frequency.....	75
Figure 4.26 Waterfall of vaneless space Kulite frequency spectra for mid-choke throttle line survey showing frequency content up to 18 times the rotational frequency.....	76

Figure 4.27 Waterfall of vaneless space Kulite frequency spectra for mid-choke throttle line survey showing frequency content up to 10 times the rotational frequency.....	76
Figure 4.28 Waterfall of leading edge Kulite amplitude spectra along 85% N_c speedline showing frequency content up to 18 engine order	78
Figure 4.29 Waterfall of leading edge Kulite amplitude spectra along 85% N_c speedline showing frequency content up to 10 engine order	79
Figure 4.30 Comparison of variance in leading edge Kulite signal with changing throttle position.....	79
Figure 4.31 Waterfall of leading edge Kulite amplitude spectra along 100% N_c speedline showing frequency content up to 18 engine order	80
Figure 4.32 Effect of throttle position on the impeller leading edge relative Mach number	80
Figure 4.33 Slope of static-to-static pressure coefficient from mid-choke to op-line for multiple regions in the compressor, positive and negative slopes are indicated by the red and blue shaded regions respectively	82
Figure 4.34 Variation in sensitivity of impeller efficiency to decreasing tip clearance for a range of operating speeds.....	84
Figure 4.35 Variation in sensitivity of impeller total pressure ratio to decreasing tip clearance for a range of operating speeds	84
Figure 4.36 Contour of static pressure normalized by inlet total pressure in the inducer at 80% of the corrected design speed.....	86
Figure 4.37 Contour of static pressure normalized by inlet total pressure in the inducer at 85% of the corrected design speed.....	86
Figure 4.38 Contour of static pressure normalized by inlet total pressure in the inducer at 90% of the corrected design speed.....	86
Figure 4.39 Contour of isentropic relative Mach number in the inducer at 80% of the corrected design speed	87
Figure 4.40 Contour of isentropic relative Mach number in the inducer at 85% of the corrected design speed	88
Figure 4.41 Contour of isentropic relative Mach number in the inducer at 90% of the corrected design speed	88
Figure 4.42 Contour of static pressure normalized by inlet total pressure in the inducer at a steady point recorded just prior to stall at 90% corrected speed.....	88
Figure 4.43 Contour of isentropic relative Mach number in the inducer at a steady point recorded just prior to stall at 90% corrected speed	89
Figure 4.44 Relative shroud Mach number through the impeller at four different corrected speeds.....	90

Figure 4.45 Fraction of static pressure rise in the impeller that is done by the inducer across a wide speed range	90
Figure 4.46 Fraction of relative diffusion in the impeller that is done by the inducer across a wide speed range.....	91
Figure 4.47 Contour of rms pressure variation in the inducer at 80% corrected speed for the mid-choke throttle setting	92
Figure 4.48 Contour of rms pressure variation in the inducer at 85% corrected speed for the mid-choke throttle setting	92
Figure 4.49 Contour of rms pressure variation in the inducer at 90% corrected speed for the mid-choke throttle setting	92
Figure 4.50 Contour of rms pressure variation in the inducer at 95% corrected speed for the mid-choke throttle setting	93
Figure 5.1 Numerical and experimental impeller total pressure ratio from 80% to 90% corrected speed.....	97
Figure 5.2 Numerical and experimental impeller isentropic efficiency from 80% to 90% corrected speed.....	97
Figure 5.3 Comparison of experimental and numerical impeller shroud static pressures at four different corrected speeds.....	99
Figure 5.4 Comparison of shroud static pressure normalized by inlet total pressure for experimental and numerical results at the 80% corrected speed and op-line throttle setting	101
Figure 5.5 Comparison of shroud static pressure normalized by inlet total pressure for experimental and numerical results at the 85% corrected speed and op-line throttle setting	101
Figure 5.6 Comparison of shroud static pressure normalized by inlet total pressure for experimental and numerical results at the 90% corrected speed and op-line throttle setting	102
Figure 5.7 Inducer tip leakage flow structure at 80% corrected design speed, the streamlines are colored with relative Mach number to indicate the presence of a shock	104
Figure 5.8 Inducer tip leakage flow structure at 85% corrected design speed, the streamlines are colored with relative Mach number to indicate the presence of a shock	105
Figure 5.9 Inducer tip leakage flow structure at 85.5% corrected design speed, the streamlines are colored with relative Mach number to indicate the presence of a shock	105
Figure 5.10 Inducer tip leakage flow structure at 90% corrected design speed, the streamlines are colored with relative Mach number to indicate the presence of a shock	106
Figure 5.11 Meridional planes used to calculate blockage in the inducer	107

Figure 5.12 Numerically calculated blockage at the impeller leading edge for a range a corrected speeds	108
Figure 5.13 Numerically calculated blockage for locations throughout the inducer at 80%, 85%, 85.5%, and 90% corrected speeds	108
Figure 5.14 Contour of the circumferentially averaged meridional velocity in the impeller at 80% corrected speed (the image is skewed to protect the proprietary nature of the impeller geometry)	110
Figure 5.15 Contour of the circumferentially averaged meridional velocity in the impeller at 80% corrected speed with a free slip boundary condition on the inlet shroud (the image is skewed to protect the proprietary nature of the impeller geometry).....	110
Figure 5.16 Comparison of blockage between 80% corrected speed cases with free-slip and no-slip boundaries on the inlet shroud surface	111
Figure 5.17 Contour of the circumferentially averaged meridional velocity in the impeller at 85.5% corrected speed (the image is skewed to protect the proprietary nature of the impeller geometry)	112
Figure 5.18 Shock structure in the inducer at 85% corrected speed. Planes shown are at 80%, 90%, and 99% span, with the isosurface indicating the region where the Mach number exceeds unity.....	114
Figure 5.19 Shock structure in the inducer at 85.5% corrected speed with isosurface showing the region where the Mach number exceeds unity.....	114
Figure 5.20 Shock structure in the inducer at 90% corrected speed with isosurface showing the region where the Mach number exceeds unity.....	115
Figure 5.21 Tip leakage vortex streamlines at 90% corrected speed, colored by normalized helicity, where red and blue indicate positive and negative values respectively	116
Figure 5.22 Tip leakage vortex streamlines at design speed, colored by normalized helicity, where red and blue indicate positive and negative values respectively	117
Figure 5.23 Limiting streamlines on the suction surface of the main blade at 90% corrected speed, boundary layer separation indicated by the red line	118
Figure 5.24 Limiting streamlines on the suction surface of the main blade at 100% corrected speed, boundary layer separation indicated by the red line	119

NOMENCLATURE

<u>Symbol</u>	<u>Definition</u>
A_{eff}	Effective area at the impeller exit
a	Speed of sound
B	Blockage factor
b_2	Impeller exit blade height
C	Venturi discharge coefficient
CFD	Computational fluid dynamics
CL	Impeller tip clearance
DSA	Digital sensor array
DAQ	Data acquisition device
h	Specific enthalpy
H_n	Normalized helicity
I	Rothalpy
K_{blockage}	Blockage factor at impeller exit
\dot{m}	Mass flow rate
P	Pressure
U	Wheel speed
V	Absolute frame velocity
Q_{in}	Heat transfer into flow
R	Radius
S_r	Strouhal number
T	Temperature
N	Compressor rotational speed in rpm
W	Relative frame velocity

Subscripts

1, 2, 3, ...	Effective area at the impeller exit
0	Stagnation property
θ	Circumferential component
m	Meridional component
c	Corrected to standard day conditions
LE	Leading edge
rel	Relative frame
ref	Reference condition
US	Upstream of venturi throat
LO	Low loading condition
HI	High loading condition

Definition**Superscripts**

Area	Blockage factor at impeller exit
Mass	Mass flow rate

Definition**Greek**

β	Venturi throat diameter ratio
ξ	Absolute frame vorticity
ϵ	Expansion factor
ρ	Density
γ	Density
Ψ_{s-s}	Static to static pressure coefficient
σ	Variance
η	Isentropic Efficiency

Definition

ABSTRACT

The primary objective of this research was to shed light on the changes in performance observed in a high-speed, centrifugal compressor that occur during the transition from subsonic to transonic operating conditions, using experimental data collected on a research compressor developed by Honeywell Aerospace, as well as results from a numerical model of the compressor.

An understanding of the flow behavior in transonic centrifugal compressors is critical as the drive for higher stage pressure ratios while maintaining a compact size results in higher rotational speeds and increased aspect ratios in the inducer of the impeller. Both of these design trends result in higher relative Mach numbers near the impeller leading edge, resulting in the formation of shocks and an increasingly complex flow field. Since it is necessary to maintain high efficiency and adequate surge margin at these conditions—to ensure the compressor is stable across the full operating range—it is important to understand the effects of the transition from subsonic to supersonic flow on performance and stability. Due to the limited availability of research in the open literature regarding transonic centrifugal impellers, especially experimental studies, these behaviors are still not fully understood.

Experimental data collected during steady state operation as well as during speed transients, showed a sudden decrease in the variance of the unsteady pressure field throughout the compressor, but most dramatically in the inducer shroud. Analysis of the performance also showed a significant increase in impeller efficiency of approximately 2 points as speed was increased from 80% to 90% of the design speed. Temperature measurements upstream of the impeller leading edge indicated a dramatic reduction in the degree of flow recirculation in the same speed range, indicating the increase in performance is related to a decrease in the blockage near the impeller leading edge. A low pressure region was also observed in the inducer passage, which disappeared upon transition to the transonic operating regime, this coupled with decreased inducer static pressure rise and relative diffusion at lower speeds, strongly indicates that increased loss in the inducer at lower speeds is responsible for the observed performance deficiency during subsonic operation.

Analysis of the numerical results revealed that the low pressure region in the inducer may be attributable to the interaction between the inlet shroud boundary layer and the low momentum tip leakage flow in the impeller passage, which at lower speeds, results in the tip leakage flow forming a large recirculation region in the inducer passage. It was also determined that the step change in

instability coincides with the inducer shock extending to the shroud and reducing the strength of the interaction between the low momentum regions in the inlet and impeller passage, thereby allowing the tip leakage flow to form into a vortex and preventing the development of the recirculation region in the inducer.

This research provides a possible explanation for the observed instability in the compressor, which may allow for further testing of techniques to mitigate the instability caused by the blockage in the inducer, such as casing treatment, bleed, or flow injection into the inducer shroud.

1. INTRODUCTION

1.1 Motivation

For the past several decades, one of the largest challenges facing engine designers is that of reducing fuel consumption and increasing efficiency. To do this, it is necessary for the compressor to deliver higher pressure air to the combustor and for the compressor itself to operate with higher thermal efficiency. Applications in the aerospace industry have the added requirement of compact size to reduce the weight and cost associated with the engine to further increase the fuel efficiency of the aircraft.

In order to meet these ever-increasing demands for higher pressure ratio, higher efficiency, reduced size, and stable operating range, designers are turning to centrifugal compressors. Centrifugal compressors are desirable for their compact size and high pressure ratio per stage compared with axial compressors, which may require multiple stages to achieve the pressure rise of a single stage radial compressor, however it should be noted that radial compressors are best suited for small inlet corrected flow rates such as turboshaft engines or downstream of axial stages. Unlike axial compressors, which achieve their pressure rise through the process of relative diffusion across multiple stages, centrifugal compressors generate total pressure rise through the centrifugal effect. In the same way that water will stay in the bottom of a bucket when spun around at a sufficiently high angular speed, the impeller of a centrifugal compressor forces air out to a larger radius. Unlike relative diffusion, which provides limited pressure rise across a blade row and can be prone to separation and therefore loss, pressure rise resulting from the increasing flow radius in the impeller is, in a sense free, as there is no loss inherent to the centrifugal effect. In order to further increase the pressure rise generated by a centrifugal stage, one obvious choice for the designer is to increase the rotational speed of the compressor. The increased rotational speed provides for a higher maximum pressure rise through the impeller, however the actual pressure rise achieved, as well as the efficiency and stall margin, are dictated by the blade geometry and detailed design of the impeller. Additionally, as the speed increases, so too does the velocity of the flow in the relative frame, which eventually leads to a transonic operating condition at the impeller inlet, where the Mach number for portions of the flow exceeds unity. This is especially true for aeroengine compressors, where restrictions on the overall diameter of the machine leads to an

increased tip radius at the inducer to accommodate higher flow rates. This increased radius leads to higher relative velocities at the inducer tip, resulting in higher relative Mach numbers. This transonic operating condition leads to shocks in the inducer section of the compressor, causing increased losses and creating a highly complex flow structure involving shock interactions with the boundary layers on both the blade suction surfaces and shroud as well as interactions with the tip leakage vortices. The intrinsically complex nature of these interactions and their highly three-dimensional structure are still not fully understood, largely due to the limited number of transonic centrifugal compressors available for research purposes, especially in the open literature.

1.2 Transonic Impeller Aerodynamics

The desire for higher speed compressors may be understood through the Euler turbomachinery equation (1.1), where work is shown to be equal to the change in the product of wheel speed and tangential absolute flow velocity. For an ideal compressor with axial inflow and radial outflow, the Euler turbomachinery equation can be simplified to show that the work done on the flow is proportional to the square of the exit wheel speed, U_2 .

$$h_{02} - h_{01} = U_2 V_{\theta 2} - U_1 V_{\theta 1} \quad (1.1)$$

Therefore, a seemingly simple method for increasing the work done by the compressor is to increase the rotational speed of the impeller. However, in real compressors, increased speed and pressure ratio also lead to the formation of shocks and increasing pressure gradients, which decrease efficiency and can negatively impact the stability of the compressor. In principle, the desired pressure rise through a centrifugal compressor can be achieved by simply providing the necessary rotational speed for a given exit radius, however the stable operating range, flow rate, and efficiency are strongly influenced by the geometry of the inducer, especially in transonic machines [1]. In order to optimize inducer designs to provide the required performance while maintaining a wide operating range, it is necessary to understand the complex flow structure that exists in the inducer of transonic impellers.

This chapter will review the basic structure of the flow field in transonic centrifugal compressor inducers, the interactions of the shock with the tip leakage vortex and boundary layer, and finally, the effects of the shock on the performance and stability of the compressor.

1.2.1 Tip Leakage Flow

High pressure ratio centrifugal compressor impellers are typically unshrouded due to the large centrifugal load that exists as a result of their high rotational speed. As a consequence, it is necessary for there to be a gap between the blade and shroud to prevent rubbing. It is also necessary to have a larger than ideal tip clearance at some operating conditions due to rates of thermal expansion between the rotor and the shroud. Therefore, to ensure a safe tip clearance is maintained during startup, a larger tip clearance than what is optimal may be required. This gap introduces complexities to the flow field, and since fluids always seek to move from high pressure regions to low pressure regions, the fluid near the pressure side of the blade seeks to move to the lower pressure of the suction side. There are two possible paths by which this can occur: one is for the fluid to migrate along the shroud across the passage, and the other, much shorter, path is for the flow to leak across the tip gap into the adjacent passage. This exchange of fluid from pressure side to suction side across the blade gap is commonly referred to as the tip leakage flow. Upon entering the adjacent passage, the tip leakage flow rolls up as a result of the cross-passage pressure gradient and shearing between the passage primary flow and the tip leakage flow, forming a thin longitudinal vortex that then propagates downstream through the rotor passage. The trajectory of the vortex into the passage is highly dependent on the blade loading, where increased loading pushes the leakage flow further toward the pressure side of the passage. Therefore, when traversing a speedline from choke to stall, one would expect the leakage vortex to shift from near the suction side towards the pressure side as blade loading is increased.

The tip leakage vortex has a significant impact on the performance of the compressor due to increased blockage as well as losses incurred by the flow recirculation near the shroud. A commonly used rule of thumb to quantify the efficiency penalty incurred by increasing tip clearance is that a 1 point increase in the ratio of the tip gap to blade height results in an approximately 1 point decrease in rotor isentropic efficiency. However, a smaller tip clearance is not always better as some numerical comparisons between flows with zero clearance and flows with varying finite clearances show that there is an optimal clearance for which the performance of the compressor with finite clearance is better than that of the zero clearance case. This is thought to be a result of the increased cross passage flow in the shroud boundary layer, since for very low tip clearance cases the flow is no longer able to escape through the tip gap to travel from the pressure to suction side of the blade.

Some studies [2]–[4] have also shown that the interaction between the tip leakage vortex and the passage shock may result in the breakdown of the vortex thereby inducing rotating stall in the compressor. The interactions of the shock with secondary flow structures will be discussed in more detail later in this chapter.

1.2.2 Boundary Layers in Turbomachinery

As with viscous flow over any real surface, boundary layers develop on the surfaces within the flowpath of turbomachines. These boundary layers form on the blade surfaces as well as the hub and shroud as a result of shear between the solid body and the flow over the body. These boundary layers are comprised of low momentum fluid that contribute to blockage in the flowpath of the compressor as well as causing instability due to boundary layer separation and wake shedding leading to regions of high loss within the flow. Early analysis of boundary layers in turbomachinery relied on data collected from flat plate experiments and airfoil cascades, however this does not account for the effect of rotation on the formation of boundary layers in real machines. As a result of the surface's rotation, there are additional accelerations applied to the flow that cannot be accounted for in wind tunnel testing. These neglected accelerations are the centrifugal and Coriolis accelerations, which combine with surface curvature can act to either stabilize or destabilize the boundary layer depending on the direction of rotation and whether the surface curvature is concave or convex. Figure 1.1 is a cartoon depiction of the effect of wall curvature and system rotation on the stability of a boundary layer. If one considers the suction surface of a centrifugal impeller blade downstream of the inducer, the wall curvature is concave, which coupled with the strong adverse pressure gradient, increases the likelihood of boundary layer separation.

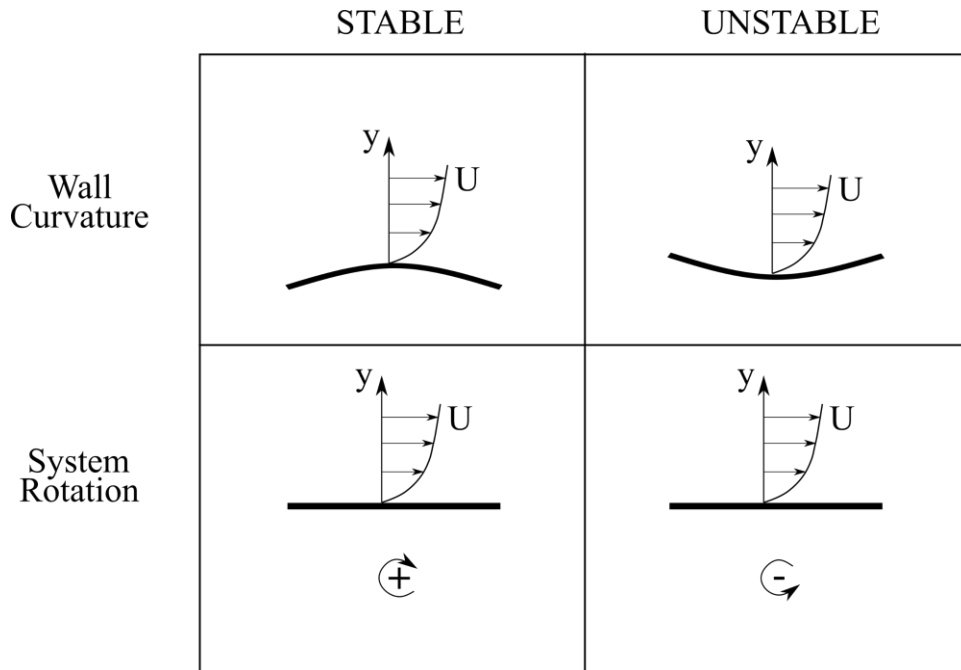


Figure 1.1 Effect of wall curvature and rotation on boundary layer stability [5]

Another factor that often results in the separation of boundary layers is an adverse or positive pressure gradient in the streamwise direction, which essentially acts to resist the motion of the flow, causing reversal of the flow direction in the low momentum fluid near the endwalls or blades and, thus, separation of the boundary layer. Due to the complex three dimensional flow field in the impeller, it is almost a guarantee the boundary layer separation will occur [5]. Separation then results in a region of high loss in the impeller due to recirculation and may also result in the impeller stalling depending on the location of separation within the impeller. A unique problem also arises in the case of transonic rotors, where the interaction between the boundary layers and shock waves may also result in separation, which will be discussed more later in this chapter.

1.2.3 Blockage

The regions of low momentum fluid that frequently occur near the shroud and hub contribute to the overall blockage that exists in the impeller, which can result in local regions of high incidence and lead to flow separation and, thus, stall. Blockage is defined by Hazby and Xu

[6] using equation (1.2) where B , V_m^{Area} , and V_m^{Mass} represent the blockage, area-averaged meridional velocity, and the mass-flow-averaged meridional velocity, respectively.

$$B = 1 - (V_m^{Area}) / (V_m^{Mass}) \quad (1.2)$$

This equation can be understood by considering the cartoon flow field shown in Figure 1.2. If the region of low momentum fluid occupies 20% of the flow path area and has a uniform velocity of half the velocity, V , in the blue region. This would give an area-averaged meridional velocity of $0.9V$, a mass-flow-averaged meridional velocity of $0.94V$, and a blockage of approximately 5 percent. As the meridional velocity of the flow in the low momentum region tends to zero, the value of blockage tends toward the percentage of the area occupied by the low momentum region. This equation can be applied to slices of the flow field taken from numerical simulations to determine the blockage in the impeller at various meridional locations, as was done by the researches in [6].

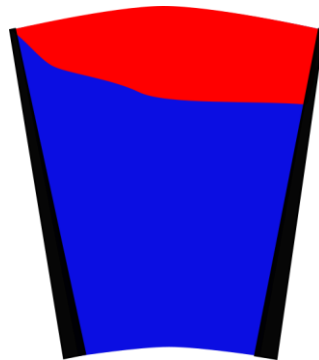


Figure 1.2 Cartoon representation of flow field in a blade passage with low momentum region near the shroud shown in red

In order to mitigate the effect of the blockage in the inducer, studies by Rodgers [1] and Hunziker Et al. [7] showed that a significant improvement in both efficiency and operating range can be achieved through the use of bleed or flow injection near the inducer tip. Hunziker Et al. utilized a system that bled flow from the impeller, downstream of the inducer, and then reinjected the flow upstream of the impeller leading edge. This had the effect of increasing the mass flow through the inducer, which had a stabilizing effect on the shroud and hub boundary layers. Also, due to the fact that the impeller had already imparted some work on the flow that was bled off, it

had a significant circumferential velocity component, which is largely conserved through the bleed channel thereby leading to the addition of co-swirl near the inducer tip, thus reducing the relative Mach number and reducing loss. The net effect was that the compressor could be operated at a higher loading condition on the characteristic, giving an improvement of 2 points of efficiency at the design speed. Similarly, Rodgers reports increases in work factor, stability, and impeller efficiency as a result of inducer shroud bleed. The improvements were present for both recirculated bleed and dumped bleed, where the air bled from the inducer is expelled from the machine. However, the dumped bleed case showed a greater improvement in efficiency as the recirculated flow is reworked by the impeller, thus decreasing the efficiency benefit. In both cases, the mechanism for the improved performance was believed to primarily be a decrease in the blockage near the impeller leading edge tip, and Rodgers concluded that the effectiveness of bleed was related to the degree of shroud curvature and, therefore, the specific speed of the machine, with higher specific speed impellers experiencing a greater benefit.

1.2.4 Inducer Shock Structure

As the flow entering a transonic impeller is accelerated along the suction side of the blade, a shock forms at the point where the turning angle of the flow is greater than what the flow can achieve through an isentropic process for a given relative Mach number, thus resulting in the formation of a shock. The location of the shock is dependent on the inlet relative Mach number, which is in turn dependent on the inlet corrected mass flow rate and the compressor wheel speed. At higher inlet relative Mach numbers, the passage shock is shifted downstream, and conversely at lower inlet relative Mach numbers the shock is shifted upstream towards the leading edge of the inducer. Numerical analyses conducted by Kaneko and Tsujita [8] as well as Hayami Et al. [9], show the effect of mass flow rate on the shock location and strength at design speed in a transonic centrifugal compressor. Both studies showed that as the mass flow rate of the machine was reduced, the shock moved closer to the leading edge and increased in strength. This shift was the result of increased incidence at the leading edge of the impeller, which resulted in increased fluid acceleration on the suction side of the blade, thereby causing a local increase in the relative Mach number and the observed increase in the strength of the shock.

The shock location is also affected by heat transfer into and out of the flow from the shroud, which is more evident during speed transients where there is a more significant gradient

between the temperature of the impeller shroud and the temperature of the flow [10]. Depending on the geometry and design speed of the impeller, it is also possible for passage shocks to form near the leading edge of the splitter blade [11], the mechanism for which is the same as that of the main blade shock described previously. Figure 1.3 shows a cartoon depiction of the inducer of a centrifugal impeller with shocks forming near the leading edge of the blades. Also shown are potential results of the interaction of the shock with the tip leakage vortex as well as a separation bubble formed by the interaction of the shock with the boundary layer on the main blade suction surface. In the case of compressors that choke in the inducer, a passage shock will also form near the inducer throat during operation in choke, however, as the compressor described in this thesis chokes in the diffuser, the effects of a shock at this location will not be discussed in detail.

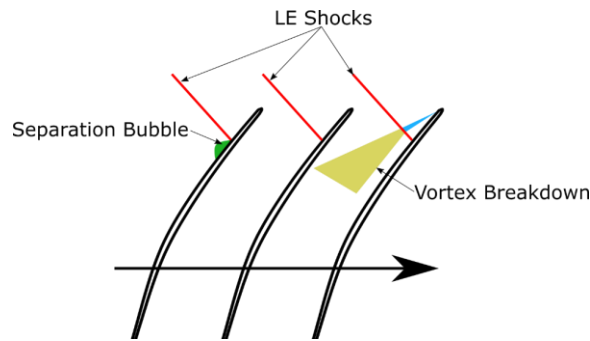


Figure 1.3 Inducer leading edge shock and interactions

The inducer shock also demarcates the point at which information from downstream is no longer able to propagate upstream and affect the inlet flow of the compressor. Since information cannot propagate upstream in supersonic flow, the only information transmitted to the inlet from downstream of the shock is through the boundary layers near the blade surface and casing, where the flow is purely subsonic.

1.2.5 Shock Interaction with Tip Leakage Vortex

Investigations conducted by Ibaraki Et al. [11], [12] into the effect of interactions between the passage shock and the main blade tip leakage vortex in a transonic turbocharger impeller have shown that the strongly adverse pressure gradient created by the passage shock can result in the

breakdown of the tip leakage vortex as it passes through the shock. Vortex breakdown is a somewhat ambiguous term, but it generally refers to a sudden change in the behavior of the vortex core. For example, the studies conducted by Ibaraki Et al. showed that the direction of rotation of the tip leakage vortex reversed after interaction with the shock at the leading edge of the first splitter blade. This breakdown then resulted in increased blockage and loss in the impeller. Breakdown was not observed in the main blade vortex due to the vortex forming downstream of the main blade shock. Zhao Et al. [13] showed similar behavior in a numerical study of a transonic impeller for a marine turbocharger. The results of the study showed that at near stall conditions the interaction of the tip leakage vortex with the passage shock resulted in vortex breakdown. The breakdown of the vortex was shown to be highly dependent on the operating condition, with the near choke operating point not exhibiting vortex breakdown. The researchers concluded that the higher blade loading near stall resulted in an increased ratio of swirl velocity to axial velocity in the tip leakage vortex, which coupled with the fact that the pressure gradient across the shock was similar for both loading conditions led to the vortex breaking down upon interaction with the shock for the near stall condition and breakdown not occurring for the choke condition where the ratio of swirl velocity to axial velocity was lower.

The aforementioned studies by Ibaraki Et al. and Zhao Et al. defined vortex breakdown using normalized helicity given in equation (1.3), where $\vec{\xi}$ is the absolute vorticity vector and \vec{w} is the relative velocity vector. Using this equation, it is possible to determine the direction of vortex rotation relative to the streamwise flow direction, as normalized helicity represents the cosine of the angle between the relative velocity vector and the absolute vorticity vector, the absolute value of normalized helicity will therefore tend toward unity near the vortex core where the vorticity and velocity vectors are nearly parallel. A positive value of helicity is indicative of clockwise rotation relative to the streamwise direction and negative is indicative of counterclockwise rotation. Using this definition, it is possible to describe the location of vortex breakdown as being the point where the scalar quantity of normalized helicity changes sign from positive to negative or vice versa [11], [13].

$$H_n = (\vec{\xi} \cdot \vec{w}) / (|\vec{\xi}| \cdot |\vec{w}|) \quad (1.3)$$

Interaction between a passage shock and a longitudinal vortex will not always result in the breakdown of the vortex as reported by Hah, et al [14]. The result of the interaction is dependent on the strength of the shock as well as the circulation of the vortex. In the case of high vortex circulation, breakdown may occur for a relatively weak shock, whereas for less circulation a strong shock is required to cause breakdown. In the absence of vortex breakdown, the interaction between the shock and vortex will shift the vortex trajectory but will not induce the dramatic increase in loss that results from the breakdown of the vortex in the blade passage. According to criteria for vortex breakdown as a result of shock vortex interaction, developed by Thomer, Et al. [15], it is unlikely that the interaction between an oblique shock and the relatively weak tip leakage vortex would result in the breakdown of the vortex.

A numerical study into the mechanism of blockage generation in the inducer of a transonic impeller was conducted by Kaneko and Tsujita [8], the results of which again showed a strong dependence of the interaction strength on blade loading. At a near-choke operating condition, the pressure gradient across the tip gap is small compared with the design point, resulting in decreased swirl velocity of the tip leakage vortex and increased axial velocity, which according to reference [15], decreases the likelihood of vortex breakdown upon interaction with a shock, with the numerical results showing an expansion of the vortex downstream of the shock but no indication of breakdown. The trajectory of the vortex was also shown to be more streamwise than the higher loading cases, resulting in reduced blockage in the inducer. At design point, the shock shifted upstream in the passage and the associated pressure gradient was stronger, which coupled with the higher swirl velocity of the leakage vortex and resulted in a stronger interaction and increased blockage. Finally, at a near stall operating condition where the pressure gradient of the shock is at its highest and the vortex is both stronger and has a more circumferential trajectory due to the reduced mass flow rate and the higher pressure gradient across the tip, breakdown of the tip leakage vortex upon interaction with the shock was observed, causing a large region of low momentum fluid to accumulate near the shroud of the inducer. Also, the increased blockage as the operating point shifted from choke to stall resulted in increased incidence near the blade tip, which the authors concluded induced the compressor to stall as the incidence becomes sufficiently large that the flow is no longer able to remain attached to the suction surface of the main blade.

A numerical study on the interactions between passage shocks and tip leakage vortices in axial, mixed flow, and centrifugal compressor rotors conducted by Schlechtrem and Lötzerich [4]

showed that tip leakage breakdown caused by shock interaction was less likely to occur in centrifugal and mixed-flow compressors due to the high degree of flow acceleration near the shroud in such machines. This acceleration stabilizes the vortex and can prevent breakdown from occurring. This conclusion is supported in a study published by Ibaraki Et al. in 2003 [16], which showed that the interaction between the tip leakage vortex and shock in a centrifugal impeller did not lead to vortex breakdown, but it did result in an increase in total pressure loss caused by the size of the leakage vortex increasing after the vortex interacted with the shock. The study also showed that steady CFD was able to qualitatively capture the flow structures resulting from the shock interaction with reasonably good agreement with experimental Laser Doppler velocimetry (LDV) measurements. The CFD results did differ somewhat from the LDV measurements taken near the shroud, and the authors were unsure if the source of the discrepancy was an error in the numerical model or experimental data.

A study conducted on an impeller with a high inducer relative Mach number of 1.6 was conducted by Higashimori Et al. [17]. The study consisted of both LDV and CFD analyses and showed that the interaction between the oblique shock at the leading edge of the main blade and the main blade tip leakage vortex resulted in a large region of reversed flow at mid-passage near the shroud. The reversed flow region was observed in the LDV measurements but was not present in the CFD analysis, which the authors believe was due to the grid being too coarse in the region near the shock or unaccounted for errors in the LDV measurements. As with the study mentioned previously, the CFD and LDV results were in good agreement except in close proximity to the shroud.

1.2.6 Shock Interaction with Suction Surface Boundary Layer

In a similar manner, as the adverse pressure gradient caused by the passage shock can have a negative impact on the stability of the tip leakage vortex, it may also lead to the destabilization of the boundary layer on the blade suction surface. The effect of the adverse pressure gradient is higher at the suction surface of the blade than in the passage due to the velocity having a local maximum near the suction side of the blade, therefore, resulting in a stronger shock in this region. The sudden increase in pressure across the shock can cause the blade surface boundary layer to separate, thereby increasing the blockage in the blade passage and creating a region of increased loss. If the pressure gradient is not sufficient to cause separation of the boundary layer, it may also

result in an increase in the boundary layer thickness, which still leads to increased blockage in the blade passage. A similar interaction also occurs between the passage shock and the impeller shroud boundary layer, which can also result in boundary layer growth or separation.

An experimental investigation into the effect of the interaction of the leakage vortex, endwall boundary layers, and leading edge shock in a transonic compressor rotor was conducted by Hah Et al. [18]. The results of the investigation showed that the interaction did not result in the breakdown of the leakage vortex, but it did result in significant cross-passage flow near the shroud downstream of the shock. The authors believe that the shock interaction with the endwall boundary layer resulted in a region of low momentum fluid. This low momentum region destabilized the compressor and caused the tip leakage vortex to oscillate and eventually spill over into the adjacent passage inducing the compressor to stall. A study by Ibaraki Et al. [11] showed unsteady wake shedding from the main blade suction surface as a result of boundary layer separation induced by the adverse pressure gradient of the main blade shock. The separation was confined to the region near the shroud on the suction surface, and the boundary layer reattached to the blade a few percent chord downstream of the separation.

The previously mentioned study by Higashimori [17] showed a significant thickening of the casing boundary layer as a result of the shock interaction, but a similar thickening of the blade suction surface boundary layer was not present in the LDV results. However, CFD analysis did show thickening of the suction surface boundary layer downstream of where the oblique leading edge shock impinged on the blade.

Langford Et al. [19] conducted linear cascade testing to simulate the flow in an axial transonic stator row, where a shock tube was used to introduce a single traveling shock wave into the stator flow field. The results of the study showed that the shock induced separation of the blade suction surface boundary layer. The size of the separated flow was highly dependent on the strength of the shock, with the strongest shock generating a blockage of 14.3% and the weakest shock tested causing a blockage of less than 3%.

Studies conducted in references [8] and [9] showed that unsteady oscillatory motion of the shock wave originating near the blade leading edge of a transonic airfoil is a result of the shock interaction with the boundary layer on the suction surface of the blade. Lee [20] describes the oscillatory behavior as resulting from pressure waves generated by the motion of the shock propagating downstream through the detached flow on the blade suction surface, which contribute

to unsteadiness in the blade wake. This unsteadiness in the wake then propagates back upstream in the blade passage and contributes energy back into the oscillation of the shock, thereby creating a self-sustaining cycle by which the shock oscillates. This theory implies that the unsteady shock motion should have a period similar to the time required for a pressure wave to propagate from the shock location to the trailing edge of the blade and then back upstream to the shock location. This periodicity exists in both wind tunnel testing of isolated airfoils as well as in numerical and experimental analysis of a transonic compressor. The results also indicated that the unsteady motion of the shock does not contribute significantly to the shock losses, with the unsteady motion increasing the loss in the tip region by just 1%. This indicates that it is not necessary to perform unsteady simulations to accurately capture losses and increased blockage associated with interactions between the shock and secondary flow structures.

1.2.7 Effect of Transonic Operation on Performance

Centrifugal compressors typically display an inverse relationship between efficiency and inlet relative Mach number. As the relative Mach number at the inducer increases, the strength of the shocks formed also increases, thereby increasing the entropy generated across the shock. The increase in shock strength also increases the strength of the interactions between the shock and secondary flow structures, which may result in breakdown of these structures into regions of recirculating flow. Recirculation introduces significant loss, as the impeller is continuously adding work to this flow, but since the flow is trapped in the recirculating region, it does not contribute to the overall pressure rise of the machine. Zhao Et al. [13] stated that the inducer shock leads to increased loss through three mechanisms. Interaction between the shock and the impeller primary flow, interactions between the shock and tip leakage vortex leading to vortex breakdown, and interactions between the shock and suction surface boundary layers lead to flow separation and increased blockage. The losses resulting from interactions between the shock and secondary flow structures were found to be on the order of 30 times greater than the losses generated by interaction with the primary flow.

Based on a review of inducer design strategies by Rodgers [1], it would be expected for a transonic centrifugal impeller to exhibit lower efficiency and a narrower operating range than would be typical for a subsonic impeller. The geometry of the impeller, and especially the inducer, become of greater importance when operating with relative Mach numbers exceeding unity. Slight

changes in the amount of turning and blade thickness can significantly impact the strength of the shock and, therefore, the losses incurred. A study on the effect of blade thickness on the performance of a transonic centrifugal compressor conducted by Skoch [21] showed that a reduction in the inducer tip thickness from 0.027 in. to 0.016 in. resulted in a 2 point increase in isentropic efficiency. Other studies [22], [23] have shown similar improvements in efficiency and stall margin as a result of bleeding and injecting flow into the inducer shroud. This exemplifies the sensitivity of the performance of a transonic compressor to relatively small changes in the flow field and blade geometry at the inlet. As the inducer is responsible for the majority of the relative frame diffusion occurring in the impeller [24], [25], it is also the region responsible for the majority of the loss found in the impeller. This means that minor changes to the inducer flow field resulting from shock interactions and instability can have a strong detrimental impact on the performance of the impeller and therefore the entire compressor.

1.2.8 Disturbance Propagation in the Impeller

A numerical study on the effect of a circumferential pressure distortion at the outlet of a centrifugal compressor was conducted by Fatsis Et al. [26]. The pressure distortion at the impeller exit was intended to be representative of a potential field from the volute tongue in a vaneless diffuser and was simulated using a 3D Euler based solver as viscous effects were not of interest to the study. The results showed the propagation of the distortion upstream through the impeller passage as a compression wave, which was then reflected at the impeller leading edge and traveled back downstream as an expansion wave. The frequency of the distortion (in this case the rotational speed in revolutions per second) was related to the propagation time of the pressure wave using the Strouhal number given in equation (1.4), where f is the frequency of the distortion in the rotating frame, L is the length of the impeller passage, and a is the speed at which the wave propagates in the passage, which is also the local speed of sound.

$$Sr = fL/a \quad) \quad (1.4)$$

The effect of the circumferential distortion at the impeller exit was shown to propagate upstream of the leading edge and result in a circumferential variation in the incidence at the impeller inlet

corresponding to the downstream distortion. The upstream distortion was out of phase with the prescribed downstream distortion due to the finite propagation time of the pressure wave through the impeller. The effect of the distortion on the incidence at the leading edge was found to be greatest for a Strouhal number of 0.5, which corresponds to the period of the distortion being equal to the time required for the pressure wave to travel to the impeller leading edge and back. This results in constructive interference between the returning pressure wave from the previous revolution and the newly formed wave. This resonance increases the effect of the pressure distortion throughout the impeller passage, rather than the newly formed wave being attenuated by the returning wave. Due to the imposed pressure distortion, the flow in the impeller was choked for only a portion of the circumference. It was, however, shown that in the choked passages, the distortion is unable to propagate upstream of the shock and may only modify the flow field by shifting the position of the shock within the passage. The results also showed a second resonance at a Strouhal number of 1, which the authors could not conclusively explain, but believed that it may be the result of the effective length of the passage, L , being reduced by the presence of the shock. The results of this study demonstrate the role the passage shock plays in isolating a portion of the inducer from downstream disturbances, as well as how these disturbances at the impeller exit can impact the flow field in the inducer.

1.3 Research Objectives

The objective of this research is to use data collected on the Honeywell Single Stage Centrifugal Research Compressor (SSCC) tested at the Purdue University High-Speed Compressor Research Laboratory to improve the understanding of the effects of the transition to transonic operation on the performance and stability of a centrifugal compressor, which despite numerous studies is still not well understood. The steady state data were collected at stable operating points along constant throttle lines starting in a fully subsonic regime and terminating in the transonic regime. Unsteady data were also collected during speed sweeps to investigate the effect of the subsonic to transonic transition region on the transient performance of the compressor. Additionally, steady state numerical simulations were also performed on the compressor stage across a wide speed range to allow for a more detailed view of the flow field and interactions within the compressor at multiple speeds. These simulations allow for a more detailed view of the flow field and the behavior of the tip leakage vortex and boundary layers before and after

interaction with the shock, as well as how the flow field changes in subsonic and transonic operating regimes.

2. EXPERIMENTAL SETUP AND METHODOLOGY

In order to characterize the effect of transonic inlet conditions on performance, it is necessary to obtain both steady and unsteady data at subsonic and transonic operating conditions. The following sections detail the experimental setup used to collect the data, as well as the procedures followed during the collection of these data.

2.1 Purdue SSCC Research Facility

The data used in this thesis were collected on the SSCC research article tested at the Purdue University High-Speed Compressor Research Laboratory, as shown in Figure 2.2. The facility consists of a 1400hp, variable speed, low-voltage AC motor mated to a 30.46:1 speed increasing gearbox. The motor is powered via a liquid cooled variable frequency drive, which is capable of holding the speed of the motor within 0.1 rpm of the set speed, which is approximately 0.007% of the compressors design speed. The gearbox transmits power to the compressor via a crowned quill shaft to allow for increased tolerance in misalignment between the gearbox and compressor.

Atmospheric air is drawn into the compressor through a large settling chamber outside of the test cell via a bell-shaped inlet fitted with a filter to prevent ingestion of foreign objects. The flow passes through an ASME standard venturi flow meter to measure the inlet mass flow rate of the compressor, after which it passes through a 90° elbow and enters into a smaller plenum that is fitted with a conical flow spreader and honeycomb flow straighteners, shown in Figure 2.1 to ensure uniform, axisymmetric flow at the compressor inlet. The flow then enters the compressor inlet radially before being turned back to axial just upstream of the impeller. The compressor speed is corrected to standard day conditions using the total pressure and total temperature measurements taken at the inlet rakes shown in Figure 2.3. The speed correction also considers the ambient relative humidity [27], which is measured using a hygrometer located in the inlet duct upstream of the venturi flow meter. The humidity correction allows for repeatable performance across the wide range of ambient weather conditions that exist in central Indiana, where the facility is located. The compressor speed is monitored using a monopole sensor located above a keyed shaft, such that a magnetic proximity probe sees a step change in shaft displacement once per revolution.

The compressor consists of an impeller with 17 main blades and 17 splitter blades with a tip diameter of approximately 10 inches operating at a design speed of approximately 45,000 rpm giving a total pressure ratio of approximately 6.5 for the stage. The impeller is followed by a vaneless space with a radius ratio of 4.5% and a vaned diffuser with 25 aerodynamically shaped vanes. After exiting the diffuser, the flow is turned back to axial and a vaned deswirl is used to reduce the circumferential component of the velocity. Downstream of the compressor is a rotating collar type throttle, through which the flow enters a collector plenum and is then discharged to outside the test cell. Flow is bled from the machine at the hub near the impeller trailing edge, which is then exhausted through a venturi to measure the mass flow rate of the bleed air, which is adjusted using a pneumatically controlled valve. All of the steady data used in this thesis were collected with a bleed flow rate of 1% the inlet mass flow rate. A unique feature of this research compressor is the ability to continuously adjust the exducer tip clearance during operation by shifting the rotating assembly forward and aft, enabling the tip clearance to be maintained at a constant value, which allows for both testing at various tip clearances, as well as maintaining a constant tip clearance for all steady points to reduce the number of variables that are influencing the compressors performance at various operating points. The tip clearance is continuously monitored by 4 capacitance probes each at the inducer, knee, and exducer distributed around the circumference. Further details about the SSCC facility may be found in reference [28].

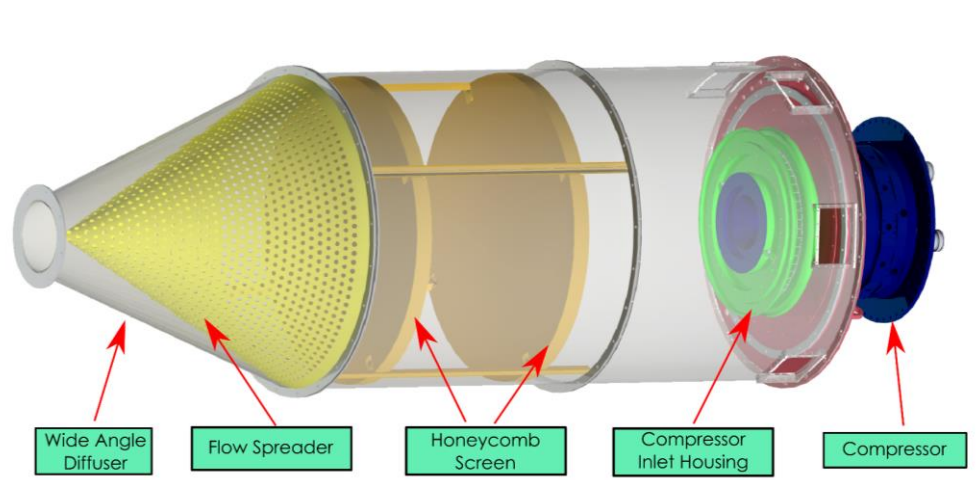


Figure 2.1 Axisymmetric inlet plenum with flow spreader and honeycomb

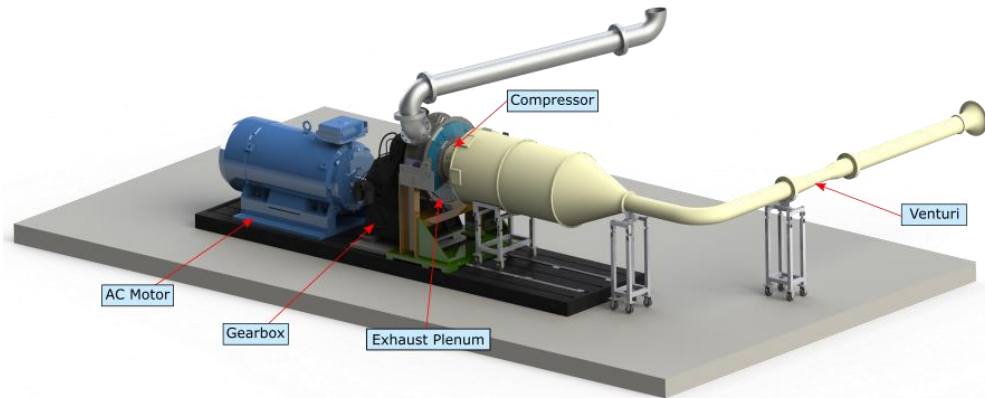


Figure 2.2 Purdue SSCC experimental testing facility

2.2 SSCC Facility Instrumentation

The primary objective of this research was to investigate the change in impeller performance observed during the transition from subsonic to transonic operating conditions. To do so, it is necessary to ensure that the data are repeatable, and that the compressor is operating at steady state conditions. Performance data were also acquired during speed transients. These data are not representative of steady state performance, but they allow a qualitative view of the compressor behavior throughout the operating range.

2.2.1 Steady Instrumentation

To measure compressor performance there are total pressure and total temperature rakes located in the inlet and exit of the compressor flowpath. There are 4 rakes with 6 elements each in the radial section of the inlet, with 5 total pressure elements distributed from hub to shroud and a single total temperature element located at mid-span on each rake. The exit flow total conditions are measured with 8 total pressure and 4 total temperature rakes, with 3 elements each, at the exit of the deswirl, where the rakes are distributed circumferentially such that the rakes are at 4 different pitchwise locations relative to the deswirl vanes. Additionally, there are 6 total pressure rakes with 3 elements each distributed circumferentially at the diffuser exit.

Component performance is monitored with static pressures placed along the impeller shroud and along the hub of the diffuser as shown in Figure 2.3. Additionally, there are two bare-bead thermocouples placed on the shroud just upstream of the impeller leading edge, which

measure the flow temperature, and can be used to give an indication of flow recirculation or stall upstream of the impeller. A summary of the pressure and temperature measurements used to characterize performance is given in Table 2.1

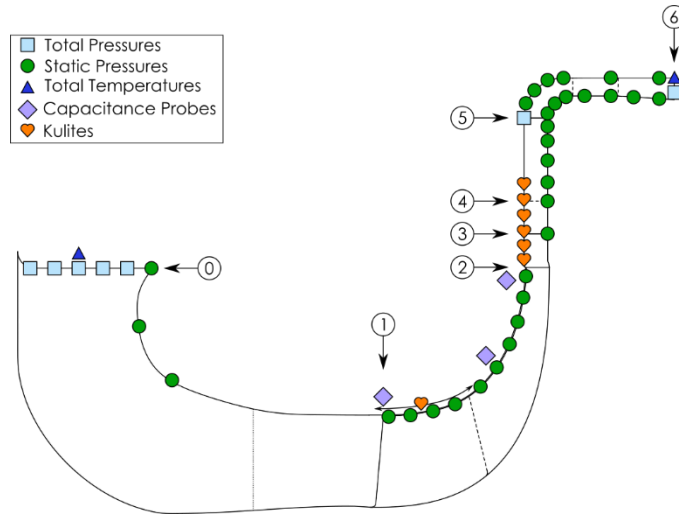


Figure 2.3 SSCC flowpath instrumentation locations

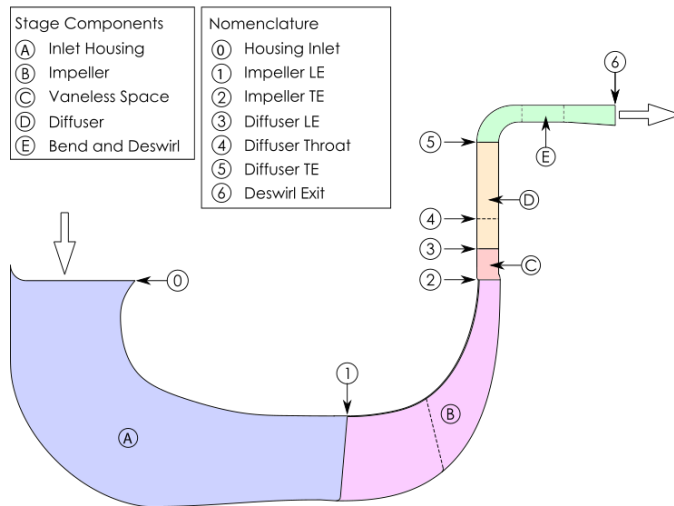


Figure 2.4 SSCC flowpath nomenclature

Table 2.1 Summary of steady performance instrumentation

Location	Total Pressure	Total Temperature	Static Pressure
Inlet	20	4	6
Impeller	0	0	22
Diffuser	18	0	48
Bend and Deswirl	24	12	34
Total	62	16	110

All of the static and total pressures used for monitoring compressor performance are read using Scanivalve DSA 4000 enclosures with 16 DSA 3016 modules giving a total of 256 differential pressure measurements. The static pressure in the inlet housing are read using 2.5 and 5.0 psid range modules while the remainder have a 100psid range. All of the DSA measurements have uncertainties of $\pm 0.06\%$ of the full scale range of the respective module. The DSA reference pressure and backface bleed venturi total pressure are measured with Rosemount absolute pressure transducers with a range of 13-15 psia and an uncertainty of 0.05% of the full scale range. The differential pressures of the venturi flow meters used to monitor the bleed flow rates are read with redundant Rosemount differential pressure transducers with 0-3 psid ranges. The voltage signals from the capacitance probes, thermocouples, hygrometer, and health pressure transducers are read using two Agilent 34980 enclosure with two 40-channel multiplexers, which give temperature measurements with 2.2°C of uncertainty for the k-type thermocouples used for measuring total and static temperatures in the compressor. A diagram of the performance data acquisition setup is given in Figure 2.4.

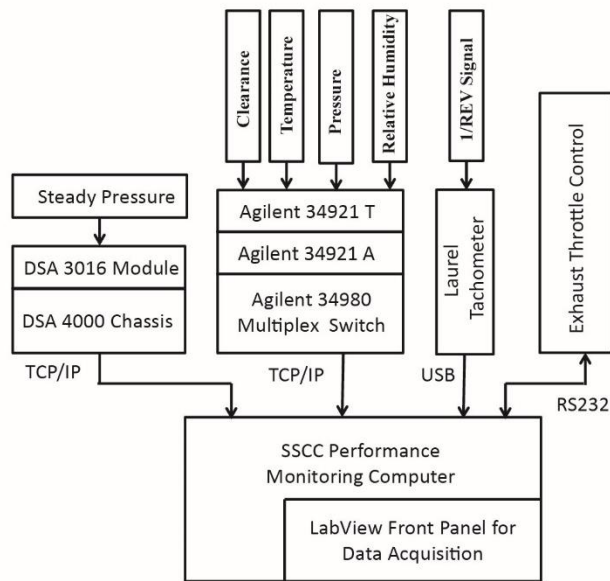


Figure 2.5 Performance data acquisition setup

2.2.2 Health Monitoring

The health of the compressor and driveline is monitored using an array of pressure transducers, thermocouples, and flow meters that monitor the oil pressures, oil flow rates, oil temperatures, bearing temperatures, and air pressures for the gearbox and compressor. The facility features a secondary air system which provides buffer air for air-oil carbon seals as well as labyrinth seals used to seal air from entering and exiting the compressor flowpath. There is also a thrust piston used to balance the thrust load generated by the compressor to maintain the net thrust on the bearings within their design range. Additional information for the secondary air and oil systems can be found in [1].

2.2.3 Fast Response Instrumentation

In order to resolve time varying flow features, the compressor is fitted with 38 Kulite fast-response pressure transducers located in the impeller shroud, vaneless space, and diffuser flowpath. There are 11 meridional impeller transducers extending from just upstream of the impeller leading edge to just downstream of the leading edge of the splitter, additionally there are 3 transducers distributed circumferentially at the same axial location as the leading edge sensor,

which allows for the characterization of rotating stall in the inducer of impeller. The meridional distribution of the impeller shroud Kulites is depicted in Figure 2.6. The remaining Kulites are distributed evenly between two diffuser passages and at two radius ratios in the vaneless space.

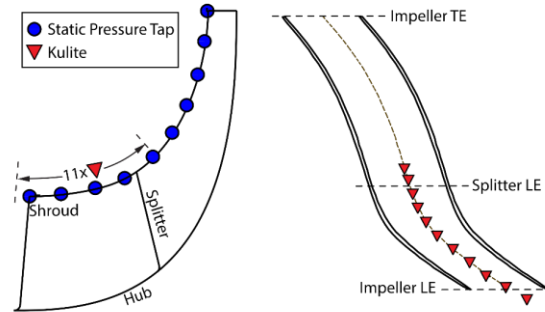


Figure 2.6 Impeller shroud static pressures and meridional Kulites

The data acquisition setup for the unsteady pressure transducers is shown in Figure 2.7 and consists of Precision filter PF28118 cards which amplify and filter the raw voltage signal from the Kulite to prevent quantization error and aliasing. To prevent aliasing the data are low-pass filtered with a 190kHz cutoff for steady points and a 40kHz cutoff during sweeps, which both satisfy the Nyquist criterion to prevent aliasing of the signal. The output of the precision filter is then sampled by an NI DAQ model 6358, which allows simultaneous sampling of all channels at up to 1.2MHz. During normal operation and sweeps, the Kulites are sampled continuously at 100kHz, which is approximately 4 times the blade pass frequency at design speed and more than sufficient to capture surge and rotating stall (which are relatively low frequency phenomenon) while preventing the file sizes from becoming unusably large. When collecting detailed data at steady operating points, the Kulites are sampled for 5 seconds at 1MHz, which allows for a sufficiently large number of samples per passage to characterize the flow field in the impeller when operating at design speed.

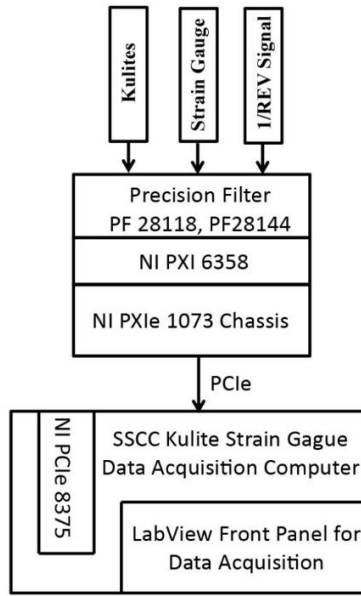


Figure 2.7 Unsteady data acquisition setup

2.3 Experimental Procedures

The data used for this thesis consist of both data collected with the compressor operating at steady state and during sweeps from 40% to 100% corrected speed. Steady-state data were acquired from 70% to 95% speed, which covers both subsonic and transonic operating regimes, with smaller speed steps of 0.5%Nc being used in the transition region between 80% and 90% corrected speed. The following sections outline the procedure used to collect these data.

2.3.1 Steady Data

Steady data were collected after the compressor achieved a stable operating condition, which was determined by monitoring the response of thermocouples embedded in the impeller shroud and backface. Once these temperatures reached equilibrium, the performance data were recorded. Data were collected along nine speedlines from 40% to 100% corrected speed as shown in the compressor map in Figure 2.8. Additional data were collected along the two throttle lines shown in red, from 70% to 95% corrected speed. Data were recorded in 1% Nc increments from 70% to 75% after which the step size was decreased to 0.5% Nc from 75% to 92% and then the step sized was increased back to 1% Nc from 92% to 95% to limit the exposure of the instrumentation to the high temperatures and pressures that exist at higher speeds. After each speed

step, the aerodynamic seals, backface bleed flow rate, and tip clearance were adjusted to ensure consistency across the full speed range. The surveys were performed at two throttle conditions which will be referred to as the mid-choke and op-line loading conditions for the remainder of this thesis.

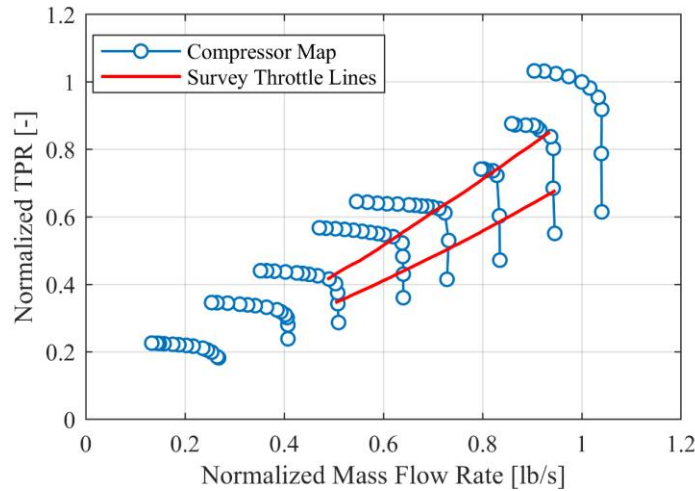


Figure 2.8 Compressor total pressure map showing constant throttle survey lines

2.3.2 Transient Data

Transient data were collected for two sweeps at the same throttle settings as the two throttle line surveys shown in the previous section. Due to the effects of heat transfer during speed transients [10] the loading conditions are not identical for the steady and unsteady data, but the transient data were sufficient to define a speed range for the steady survey while also providing a qualitative view of the compressor’s behavior across a broad speed range. Figure 2.9 shows the compressor total pressure map with the two speed sweeps shown in red, as with the steady survey, sweeps were performed at both the mid-choke and op-line loading conditions. Aero seals, bleed flow rates, and impeller tip clearance were not perfectly set during the sweeps due to the relatively short duration of the sweeps. Therefore, secondary effects from varying tip clearance and changing bleed rates are present in the transient data. For these reasons, the transient data are treated as strictly qualitative.

Due to limitations with the sampling rates of the steady performance instrumentation, the sampling rate for the steady data is orders of magnitude lower than that of the unsteady data, i.e. ~ 0.5 Hz compared with 1MHz. As a result, in order to use the two datasets together it is necessary

to map the steady data to be the same signal length as the unsteady data for the sweep. This is done using the only common measurement between the two data sets, which is the compressor rotational speed. The speed measurements from the steady and unsteady data are then used to align the two signals, such that they correspond to the same time span of testing. This mapping allows for observations to be made about how the unsteady signals respond to changes in corrected speed, mass flow rate, total pressure ratio, etc.

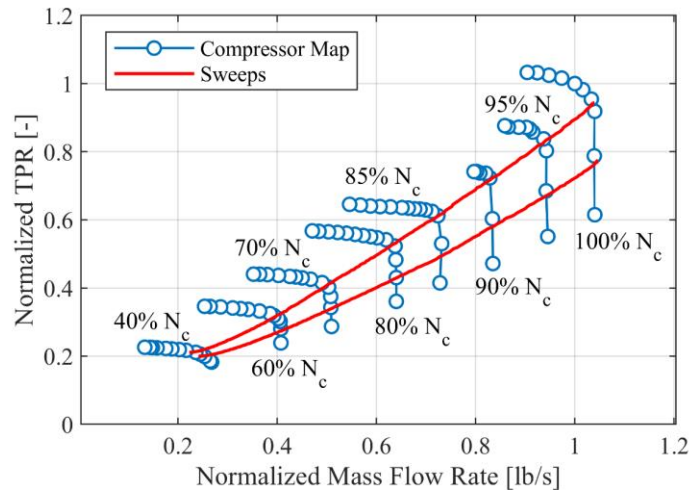


Figure 2.9 Compressor total pressure map showing constant throttle sweeps

2.4 Computational Model

Due to the size limitations within the flowpath of an engine-scale centrifugal compressor, it is not always possible to insert probes to capture minute flow details, without the use of laser anemometry (for which this research article is not instrumented). Instead, the use of numerical simulations in conjunction with experimental results are used to fill in the gaps where it is not possible to collect data. The computational model used is shown in Figure 2.10. For the sake of computational efficiency, only a single passage of the impeller, diffuser, and vaned deswirl were simulated. The two-equation BSL turbulence model was used in all domains, and heat transfer was accounted for by applying an experimentally measured shroud temperature profile to the impeller shroud in the model. The inlet boundary was set to a uniform total pressure and total temperature corresponding to standard day conditions of 14.7 psi and 59°F. For the outlet, a mass flow rate boundary condition was used which was set to be the same as the experimentally measured mass flow rate for the corresponding corrected speed. The shroud temperature in the impeller was

defined using experimental measurements of the shroud metal temperature taken at the leading edge, knee, and exducer at the same speed as the simulation in order to capture the effects of heat transfer into and out of the impeller flow. Further details on the development and validation of the computational model as well as a grid independence study can be found in the thesis in reference [29]. Simulations were performed at a range of corrected speeds around the region of interest determined from experimental results. The speed range of interest was from 80% to 90% N_c , with special attention to the region around 85% N_c as this is near where significant changes in behavior were observed during testing. Based on the results of other studies, as cited in the previous chapter, a steady simulation is able to accurately capture the key flow features in the impeller as well as those that result from interactions of the shock with the leakage vortex and boundary layers. Due to the high level of unsteadiness in the flow at speeds between 83% and 85% N_c , there was some difficulty achieving numerical convergence. As it is impossible to differentiate whether the results of the non-converged solutions are representative of the actual flow field or whether they are numerical artifacts, only the solutions from fully converged simulations will be presented in this thesis.

Experimental and Computational results were processed in the same manner to ensure a consistent comparison across the two data sets. Also, all figures depicting the geometry of the SSCC rig have been skewed to obscure any proprietary design features.



Figure 2.10 Computation domain used for numerical analysis of compressor stage

3. DATA PROCESSING

The following chapter will discuss the data analysis techniques used to process the compressor performance data and unsteady data for both steady state and transient compressor operation.

3.1 Performance Data Analysis

3.1.1 Mass Flow Rate

The mass flow rate through the compressor is calculated using an ASME standard venturi flow meter. The pressure drop across the venturi and the venturi inlet total pressure are measured using highly accurate Mensor digital pressure transducers, which allow for the mass flow rate to be calculated with uncertainties on the order of 1e-3 lb/s. The flow rate is calculated using equation (3.1), where C is the discharge coefficient of the venturi determined through calibration, β is the ratio of the throat diameter to the upstream diameter, ϵ is the expansion factor, d is the throat bore diameter, ΔP is the pressure drop across the flow meter, and ρ is the air density.

$$m_i = C / \sqrt{1 - \beta^4} \epsilon \pi / 4 d^2 \sqrt{2 \Delta P \rho_{us}} \quad (3.1)$$

The mass flow rate calculation uses real gas properties of air, which includes the measured relative humidity, to determine air density. There are also thermocouples attached to the venturi to read the throat metal temperature, which allows the mass flow calculation to compensate for variations in the throat diameter caused by thermal expansion.

The mass flow rate is corrected to standard day conditions using equation (3.2), where ρ_{ref} and a_{ref} are the density and speed of sound at standard day conditions of 59°F and 14.7 psi, and ρ_{us} and a_{us} are the density and speed of sound retrieved from REFPROP using the measured static temperature and pressure upstream of the venturi as well as the measured relative humidity.

$$m'_c = (\rho_{ref} a_{ref}) / (\rho_{us} a_{us}) \quad (3.2)$$

These corrections for temperature, pressure, and humidity ensure that data may be repeated across a wide range of ambient weather conditions. The mass flow rates for the bleed flows are calculated in the same manner as they are also measured using venturi flow meters.

3.1.2 Total Pressure Ratio

The compressor total pressure ratio is simply the ratio of the area-averaged total pressures measured at the inlet rakes and the deswirl exit rakes.

$$TPR = P_{06}/P_{01} \quad (3.3)$$

3.1.3 Efficiency

The efficiency is calculated using equation (3.4), where h_{06} and h_{01} represent the stagnation enthalpy at the deswirl exit and inlet rakes, respectively, and h_{06s} represents the isentropic exit enthalpy assuming the exit temperature and pressure were achieved without entropy generation.

$$\eta = (h_{06s} - h_{01})/(h_{06} - h_{01}) \quad (3.4)$$

The values of enthalpy are retrieved using the NIST-developed MATLAB program REFPROP, which takes the total temperature and total pressure as inputs. The enthalpy for state 6s is determined using the total pressure at station 6 and the specific entropy at station 1 as the inputs to REFPROP.

3.1.4 Impeller Exit Conditions

Due to the large size of Kiel head total pressure elements relative to the impeller exit flowpath, there are no total pressure nor total temperature measurements taken at station 3. The impeller exit total pressure is calculated using an iterative procedure which is outlined in this section.

First, the tangential velocity at the impeller trailing edge is calculated using equations (3.5) and (3.6). It is assumed that the diffuser and deswirl are adiabatic, such that the total temperature measured at the deswirl exit is the same as that at the impeller trailing edge. Additionally, since enthalpy is a weak function of pressure, the total pressure at the deswirl exit is used for the initial guess of impeller exit total pressure.

$$h_{0i} = Refprop(P_{0i}, T_{0i}) \quad (3.5)$$

$$V_{\theta 2} = ((h_{06} - h_{00}) + U_1 V_{\theta 1})/U_2 \quad (3.6)$$

Next, the meridional velocity at the impeller exit is calculated using equations (3.7) through (3.9) where, for the initial calculation, density is calculated using temperature and pressure and for all further iterations density is calculate using enthalpy and pressure. The effective area at the impeller exit is calculated using the impeller trailing edge radius R_2 , the exit blade height b_2 , exducer tip clearance CL_{Axial} , and an empirical value of blockage at the impeller exit $K_{blockage}$. The effective area, calculated density, and measured mass flow rate are then used to calculate the meridional velocity.

$$\rho_i = Refprop(T_i, P_i) \text{ or } Refprop(h_i, P_i) \quad (3.7)$$

$$A_{eff} = 2\pi R_2 (b_2 + CL_{Axial}) K_{blockage} \quad (3.8)$$

$$V_{m2} = \dot{m} / (\rho_2 A_{eff}) \quad (3.9)$$

Next, the absolute velocity is calculated using equation (3.10), which is then used in equation (3.11) to calculate the static enthalpy at station 2. The density is then recalculated using the static enthalpy and used in equation (3.12) to calculate the speed of sound. Finally, the absolute velocity and speed of sound are used to calculate the Mach number which is then used to update the initial guess of the impeller exit total pressure. Equations (3.7) through (3.13) are then used to iteratively calculate the Mach number until the change in Mach number over an iteration is less than 0.0001.

$$V_2 = \sqrt{V_{m2}^2 + V_{\theta 2}^2} \quad (3.10)$$

$$h_2 = h_{02} - (V_2^2)/2 \quad (3.11)$$

$$a_2 = Refprop(\rho_2, P_2) \quad (3.12)$$

$$M_2 = V_2/a_2 \quad (3.13)$$

The converged Mach number is then used to calculate a final value of impeller exit total pressure with equation (3.14). This can then be used to calculate important performance parameters such as impeller isentropic efficiency and impeller total pressure ratio.

$$P_{02} = P_2 (1 + (\gamma - 1)/2 M_2^2)^{\gamma/(\gamma - 1)} \quad (3.14)$$

3.2 Unsteady Data Processing

3.2.1 Isentropic Relative Shroud Mach Number

The shroud Mach number in the impeller is calculated from both steady and unsteady static pressure measurements. This was done by assuming isentropic flow through the impeller, which implies that rothalpy is conserved. The Mach number is then calculated using equations (3.15) and (3.16) [24],

$$I_1 = h_{01} - (U_1^2)/2 \quad (3.15)$$

$$M_{rel} = \sqrt{(2(I_1 - h_s - U^2/2)/a)} \quad (3.16)$$

where h_s is the specific enthalpy retrieved from REFPROP using the measured static pressure and the specific entropy at the rotor inlet, which is also retrieved REFPROP using the inlet total pressure and total temperature, a is the speed of sound for real air retrieved from REFPROP, I_1 is the rothalpy at the impeller inlet, and U is the wheel speed at the radius of the static pressure measurement.

Due to the relative inaccuracy associated with the fast-response pressure transducers sensing measuring absolute pressure, only the dynamic pressure components from the Kulites are used in the Mach number calculation. The absolute pressure at the Kulite locations was determined through linear interpolation of the impeller shroud static pressure taps. The mean pressure was then removed from the Kulite signal, and the interpolated shroud static pressure was used to offset the unsteady signal. This method gives a more accurate value for the Mach number, since the absolute ambient pressure measured by the Kulites has been observed to vary by more than one psi across different sensors when the impeller is stationary.

3.2.2 Quantification of Kulite Signal Unsteadiness

The unsteadiness of the Kulite signal is used as a means to quantify the unsteadiness in the flow field near the impeller shroud. The unsteadiness was analyzed by first removing the mean of the signal, such that only the dynamic pressure component remained, and then the signal was filtered to remove all content at and above the blade passing frequency. The variance of the signal was then calculated using equation (3.17), where σ represents the variance of the signal, x_i is the i^{th} element of the signal, and n is the total number of elements in the signal. The variance is calculated for transient data by segmenting the signal into chunks that are 8,192 samples long, and then calculating the variance for each segment using equation (3.17).

$$\sigma = \sum_{i=1}^n (x_i - \mu)^2 \quad (3.17)$$

3.2.3 Kulite Signal Processing for Sweeps

Due to the change in absolute pressure during speed transients, it is not possible to remove the DC component of the Kulite signal by subtracting the mean of the signal as is done at steady points. Instead, the signal was filtered with a band pass filter with a low-pass frequency of 10Hz, which effectively removes the absolute pressure from the signal. Similarly, the blade pass frequency is also variable during the sweep, so the upper cutoff frequency was set to 3kHz, which is lower than the blade pass frequency at the minimum speed during the sweep. This ensures that the high frequency content associated with the blade pass frequency and its harmonics are removed from the signal for the entire speed range.

The frequency content of the Kulite data during speed transients is also of interest. This data is analyzed using Campbell diagrams, an example of which is shown in Figure 3.1. Campbell diagrams are most commonly used to analyze mechanical vibration data from strain gauges or accelerometers, but in this case, they are used for the analysis of fast-response pressure data from Kulites. The diagram is made by segmenting the Kulite signal into chunks with a length of 8,192 samples using a Hann window with 50% overlap between the segments. The segment size of 8,192 samples was chosen as it is large enough to provide high resolution in the frequency domain, while also being a short enough duration that the compressor rpm does not vary meaningfully for each segment. The segments are then transformed to the frequency domain using a discrete Fourier transform and the average rpm is calculated for each using the once-per-revolution signal from the

monopole sensor on the compressor shaft. The amplitude spectra are presented on a scatter graph at a constant location on the abscissa for each segment. The result is that the abscissa represents the rotational speed of the compressor, with frequency on the ordinate. The amplitude of the response is then shown by both the color and size of the points on the diagram. Since the plot is of frequency vs rpm, it is possible to show the engine order as lines of constant slope. These diagrams will be used to show how the frequency content of the signal varies across the operating range of the compressor, especially in the region where the compressor transitions from subsonic to transonic operation. Since, these plots will be used for analyzing aerodynamic signals rather than mechanical data, percent of corrected design speed will be used instead of rpm for the abscissa.

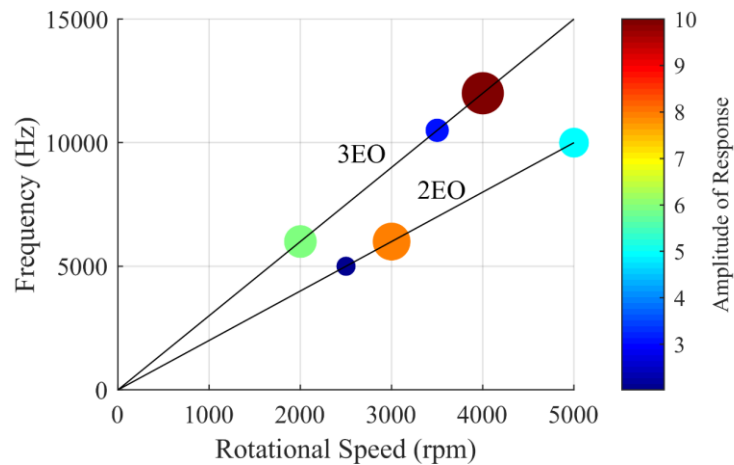


Figure 3.1 Example of a Campbell diagram showing discrete responses along the 2nd and 3rd engine order lines

3.2.4 Phase Shift of Impeller LE Kulite

Due to the sensors being subjected to high temperatures and pressures, especially during surge, a number of the Kulites in the compressor no longer give reliable signals. One of these Kulites is located at the leading edge of the impeller main blade. In order to reconstruct the signal, another Kulite at the same axial location is shifted in time such that it is effectively in the

same circumferential location as the failed meridional Kulite. A cartoon representation of the shift is shown in Figure 3.1Figure 3.2

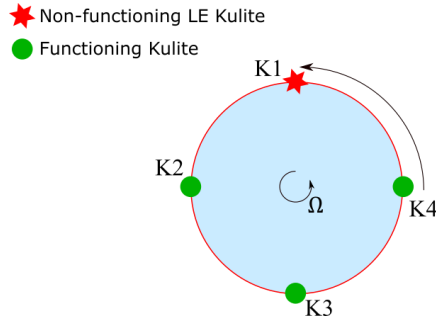


Figure 3.2 Impeller LE Kulite shift

The shift is performed by creating two time vectors, one for the unshifted meridional Kulites, and another for the Kulite shifted through α degrees around the circumference. Each time vector represents one impeller revolution, the duration of which is given by t_{rev} and is determined by the time between the rising edge of the pulses from the monopole signal. The time vectors are calculated as shown in equations (3.18) and (3.19).

$$t_1 = t_0 : t_{rev} \quad (3.18)$$

$$t_2 = (t_0 - \alpha/360 \cdot t_{rev}) : (t_{rev} - \alpha/360 \cdot t_{rev}) \quad (3.19)$$

A similar method for shifting a Kulite through a known angle was used in [30], but rather than circularly shifting the signal such that the end of a revolution is shifted to the beginning, as was done in the reference, this method simply chunks the signal and shifts it by a fraction of a revolution. Figure 3.3 gives an example of the shift, where the dotted line is the shifted portion of the signal of Kulite K4 in Figure 3.2 and the dashed line is the portion of the signal corresponding to the next impeller revolution. The dotted portion of the signal is shifted to the right such that it overlaps with the blue signal, representing the non-functioning Kulite K1. This method ensures that the blade passing events for all of the meridional Kulites corresponds to the same blade i.e. for the shifted signal blade one passes all of the Kulites simultaneously.

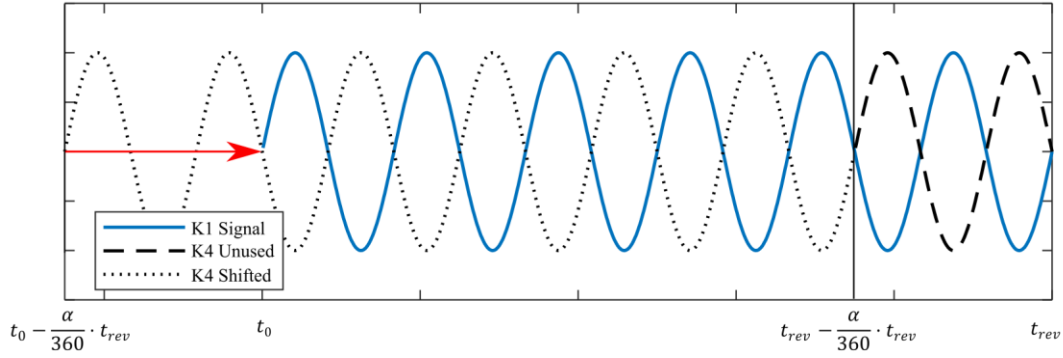


Figure 3.3 Illustration of LE Kulite signal shift for one revolution

The drawback of shifting the signals lies in the fact that the shift is based on the rotational speed of the compressor and any flow features that are not rotating at the wheel speed or a harmonic thereof will remain out of phase. For example, the method described would not ensure that a rotating stall cell would pass all of the Kulites simultaneously as this would require shifting by the rotating speed of the stall cell. It is, therefore, preferable for all of the Kulites to be placed in the desired location rather than attempting to adjust their relative location after the fact during data processing. The phase shifting method presented here was applied to the contours of the inducer inlet shown in later chapters, as the pressure transducer at the impeller leading edge was not operational when these data were acquired, another sensor at the same meridional location, but different circumferential location, was used to replace it.

3.2.5 Ensemble Average of Kulite Data

While variation from one revolution to another may be of some interest e.g. in the case of rotating stall, these variations can also make it more difficult to pick out stationary features of the flow field. For this reason, it is often beneficial to average the unsteady pressure signals across multiple revolutions. This is done by using the once-per-revolution signal from the monopole to establish a “trigger”, such that the signal can be divided into a discrete number of revolutions. The signals from each of these revolutions, called ensembles, are then averaged with each other to give a single signal that is representative of the average pressure around the impeller shroud, often referred to as an ensemble average.

4. EXPERIMENTAL RESULTS

4.1 Transient Data

4.1.1 Unsteady Data

The effect of changing Mach number on compressor performance can be observed from transient data recorded during speed sweeps from 40% to 100% of the compressors corrected design speed, which covers the region where the inducer transitions from subsonic to transonic operation. The data presented in Figure 4.1 and Figure 4.2 show the filtered responses of Kulites at different locations in the compressor. The locations for each figure are clockwise from top left: Inducer, Exducer, Vaneless Space, Diffuser Passage, as shown in the graphic in the top left of each plot. The inducer Kulite is located at the leading edge of the impeller, and the exducer Kulite is the last in the row of meridional Kulites along the impeller shroud as shown in Figure 2.6. Both Figure 4.1 and Figure 4.2 depict data from sweeps along the mid-choke throttle line, and therefore are representative of the maximum mass flow rate for a given speed. Figure 4.3 presents data collected from an acceleration sweep at the op-line throttle position and, therefore, represents a lower mass flow and higher loading condition. The data shown in the figures have been filtered to remove the DC component as well as all frequencies associated with the blade passing, as discussed in the previous chapter.

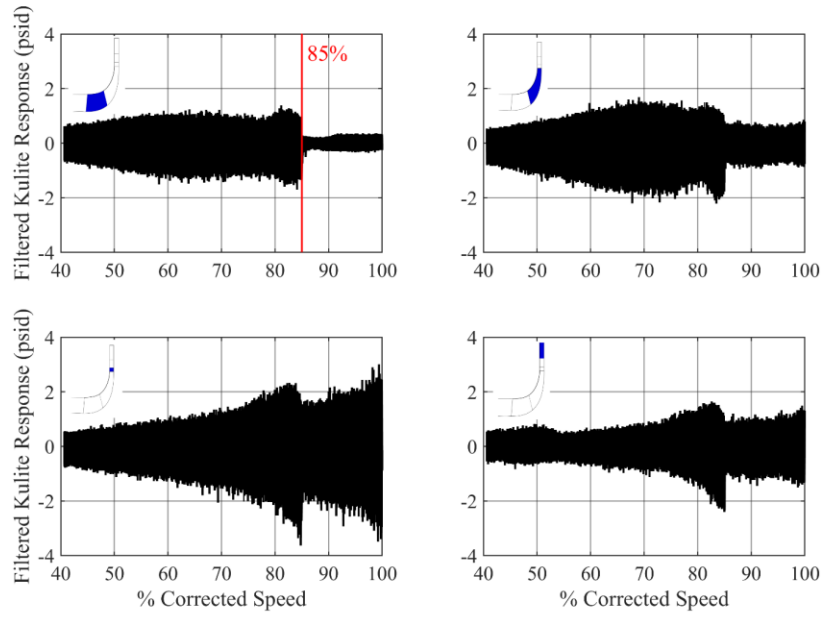


Figure 4.1 Filtered Kulite response during acceleration sweep along mid-choke line from 40% to 100% Nc

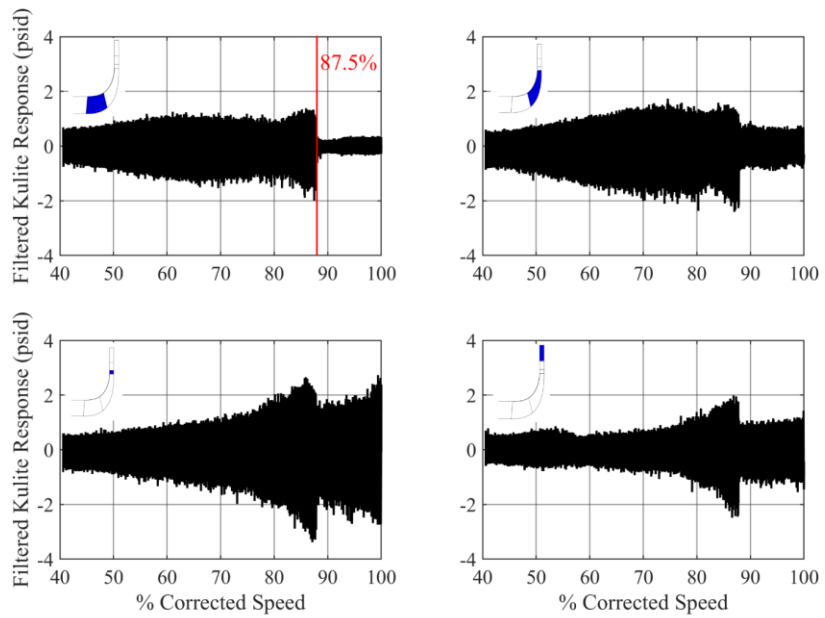


Figure 4.2 Filtered Kulite response during deceleration sweep along mid-choke line from 100% to 40% Nc

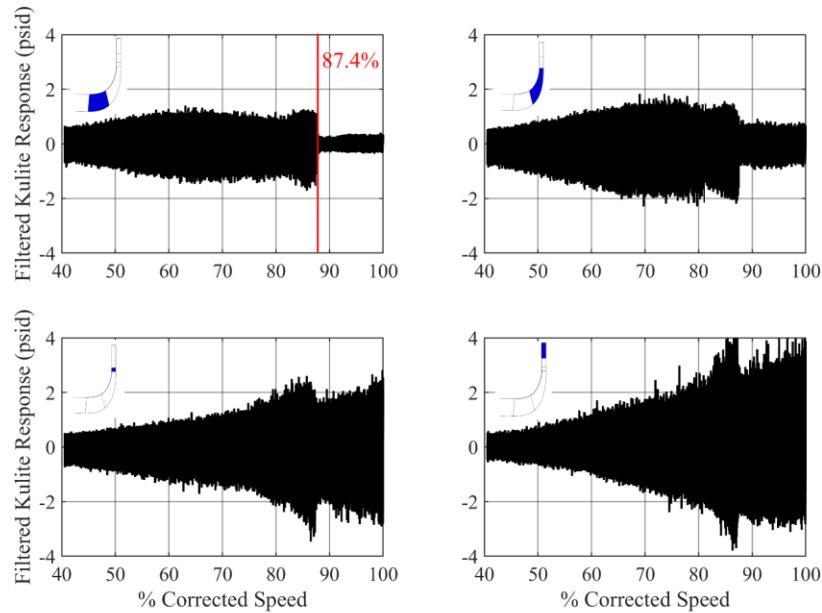


Figure 4.3 Filtered Kulite response during acceleration sweep along the op-line from 40% to 100% N_c

An immediate observation that can be made from the data shown: there is a sudden decrease in the amplitude of the signal at the speed highlighted by the red vertical line. This step-change in amplitude is most pronounced in the inducer of the compressor but is present throughout the impeller and diffuser. It should also be noted that the decrease in unsteadiness in the vaneless space and diffuser are temporary, as it continues to increase with speed immediately after the transition, whereas the impeller Kulites remain at a relatively steady level for the remainder of the sweep. Another observation is that the transition occurs at different speeds for deceleration and acceleration sweeps as well as for the higher and lower loading conditions. As this change in response is believed to be driven by the inducer shock, the mechanism of which will be discussed in more detail later, the dependence of the transition speed on loading can easily be explained by the effect of the throttle position on the inlet relative Mach number.

Velocity triangles for the inlet of an inducer with axial in-flow are shown in Figure 4.4, where the velocity triangle on the left represents the choke condition and the right represents a higher loading condition. As the throttle is closed, the axial velocity at the inducer decreases resulting in increased incidence and decreased relative velocity, and therefore decreased relative Mach number. However, the increased positive incidence that results from the reduction in mass

flow rate, locally increases the relative Mach number of the flow on the suction side of the blade. Due to the relatively small change in mass flow between the mid-choke and op-line throttle conditions, the difference in relative Mach number is relatively minor. The experimental results demonstrate a reduction in the transition speed of 2.4 points for the mid-choke case compared with the op-line case. Although the relative Mach number is locally higher at the suction surface for the higher loading condition, the shock is drawn forward in the inducer passage as a result of the increased positive incidence on the blade leading edge. This effect on the shock location is the opposite of that which occurs with increasing speed, where the shock is drawn further into the passage. This disparity in behavior may explain why the transition speed increases for the condition where the flow has a higher relative Mach number. Additionally, the lower mass flow rate for the higher loading condition will cause a global decrease in the relative Mach number due to the lower inlet axial velocity. It's possible that this effect is offsetting the locally higher Mach number on the suction surface, thus causing the increase in transition speed for the op-line condition.

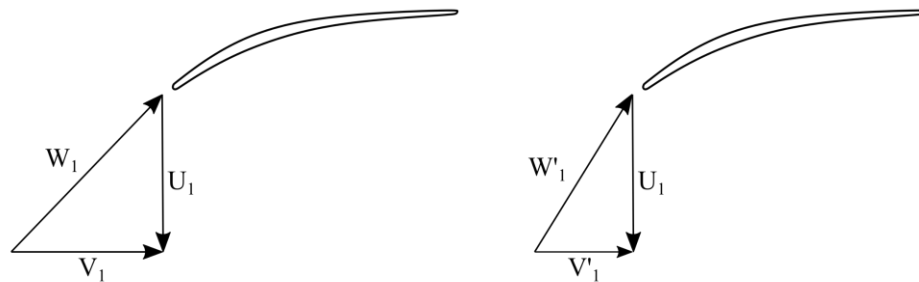


Figure 4.4 Velocity triangles at the inducer for low (left) and high (right) loading conditions

The cause for the change in the transition speed with the direction of the sweep is slightly more complicated and requires consideration of the effects of heat transfer on subsonic and supersonic flow. Consider one-dimensional flow with heat transfer, known as Rayleigh flow, as shown by the T-S diagram in Figure 4.5. Heat transfer is able to drive the flow Mach number toward or away from unity depending on the direction of heat transfer and whether the flow is subsonic or supersonic.

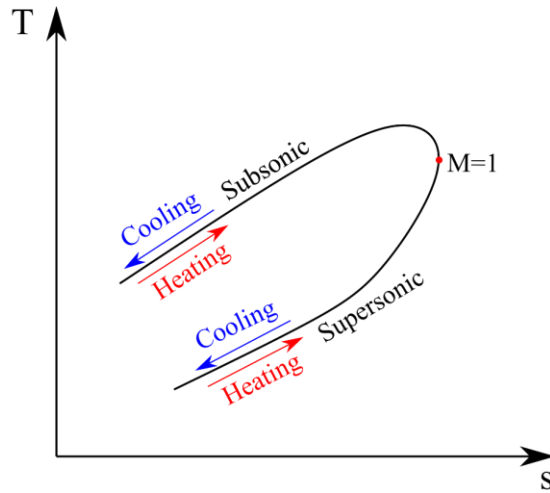


Figure 4.5 Temperature vs entropy curve for Rayleigh flow

The temperature of the flow within the compressor is primarily dependent on the rotational speed and as such responds relatively quickly to changes thereof. In contrast, the casing temperature responds more slowly to changes in compressor speed due to the high heat capacity of the metal comprising the shroud. Therefore, during deceleration from 100% speed, the temperature of the casing lags that of the flow and results in increased heat transfer into the inducer flow. Since the inducer has relatively low pressure rise and the compressor is ingesting air at ambient conditions, the flow temperature in the inducer remains low relative to the temperature of the casing, which is conducting heat from the hot exducer flow through the shroud to the inducer region as depicted in Figure 4.6. This results in heat transfer into the supersonic flow in the inducer, thus driving the flow Mach number to unity at a higher speed than for an adiabatic case. During the deceleration sweep, the shroud metal temperature is lower than for accelerations, thereby reducing the rate of heat transfer into the flow. The direction of heat transfer is the same for both acceleration and deceleration, but the reduced rate for the deceleration case results in an inlet relative Mach number lower than that of the adiabatic case for any given speed. Based on this understanding, it would be expected that the subsonic to transonic transition will occur at a lower rotational speed for the acceleration sweep than for the deceleration, which is supported by the Kulite data presented.

This explanation can be extended to predict the relative transition speed for the steady data, which were collected after the compressor reached a quasi-equilibrium state. The gradient between

the temperature of the shroud and that of the flow is greater for the steady case than for the decel case, therefore resulting in increased heat transfer into the flow for the steady case and thus, driving the Mach number in the inducer to unity at a lower speed than either the accel or decel cases. However, the difference between the acceleration and steady cases will likely be much lower than the difference between the acceleration and deceleration cases as the difference in the temperature gradient is much smaller.

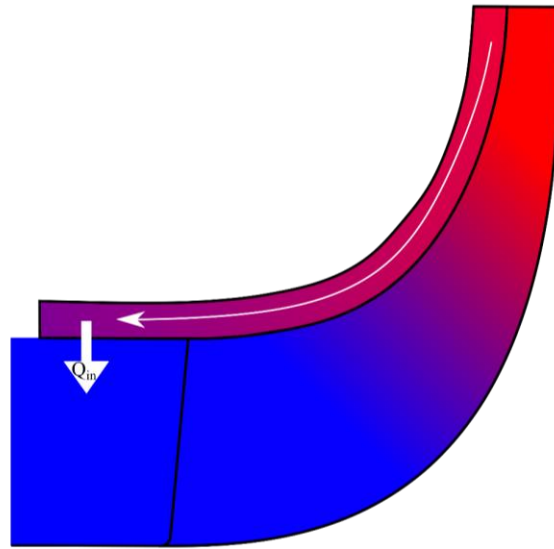


Figure 4.6 Cartoon of heat transfer through the shroud into the impeller inlet

The frequency content of the Kulite data is also analyzed to aid in understanding the behavior of the flow field in the impeller during speed transients. This is done through the use of Campbell diagrams, as discussed in the previous chapter. Figure 4.7 and Figure 4.8 show the frequency content of two Kulite signals for a speed sweep from 40% to 100% N_c along the mid-choke line, one at the impeller leading edge and one just downstream of the splitter leading edge. The diagram for the inducer Kulite shows that prior to transitioning into transonic operation, the signal is not dominated by the main blade passing frequency, but rather, it is comprised heavily of frequencies from 0 Hz to just above the main blade pass frequency. This structure begins to change just below the speed indicated by the red vertical line, where the blade passing frequency gradually becomes dominant and the lower frequency content suddenly disappears from the signal. Additionally, just prior to the transition speed, a low frequency rotating instability forms in the compressor, which vanishes upon reaching the transition speed. The diagram for the Kulite downstream of the inducer is significantly different from that of the leading edge Kulite. As this

transducer is located above the splitted portion of the impeller, the dominant frequency for the entire speed range is twice that of the leading edge signal. More significant, however, is that the sub blade pass frequency content is present for the entire duration of the sweep and does not disappear after the transition speed is reached.

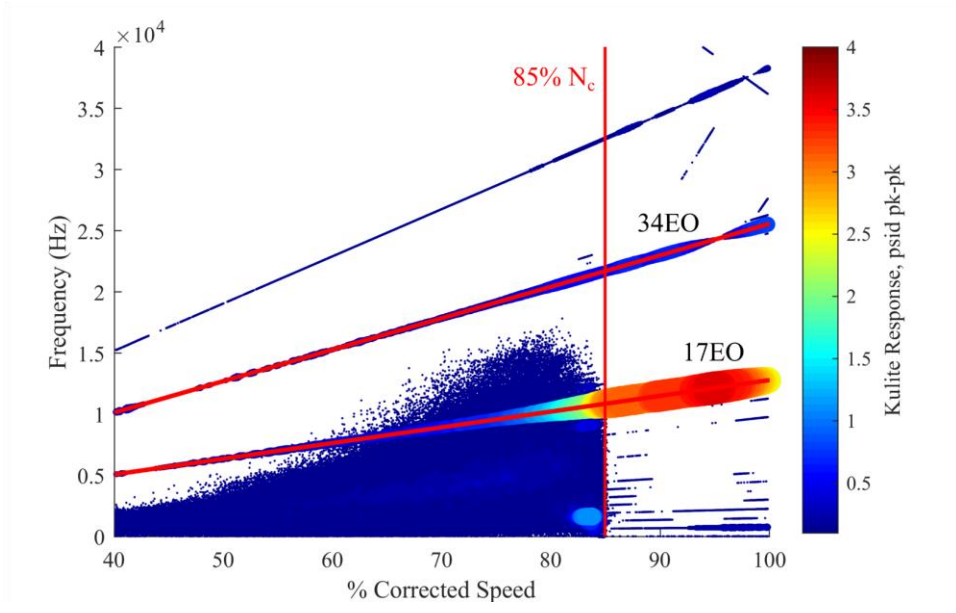


Figure 4.7 Campbell diagram of impeller leading edge Kulite signal for a mid-choke sweep acceleration

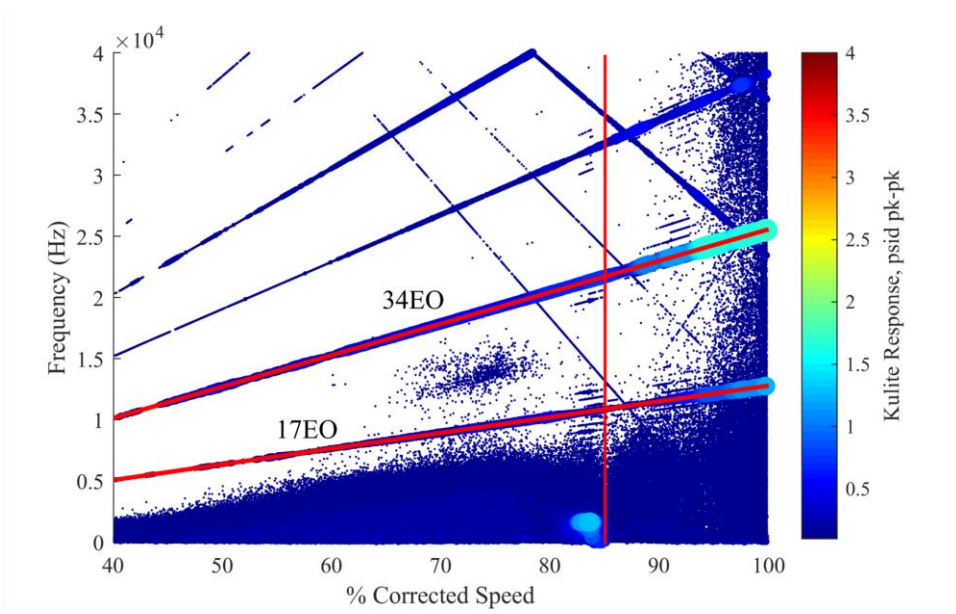


Figure 4.8 Campbell diagram of Kulite downstream of inducer for mid-choke sweep

The transition speed at which the unsteadiness decreases is at least partially dependent on the meridional location of the Kulite. Figure 4.9 shows the variance of the 4 impeller shroud Kulites for the duration of the mid-choke acceleration sweep. The curve has been smoothed with a 100 point moving average (1 millisecond) to allow easier comparison between Kulites. The red vertical line in the figure represents the speed at which the maximum variance occurs in the Kulite upstream of the impeller leading edge. The figure shows that the inflection point in the variance curve shifts to higher speeds as you move downstream through the inducer. Also, the variance of the Kulite furthest downstream remains higher than that of the inducer Kulites after reaching the transition speed. This is likely due to the fact that this Kulite is quite far downstream of the inducer shock, whereas the others are just downstream or upstream of the shock depending on the inlet relative Mach number. A similar trend is observed for the deceleration sweep shown in Figure 4.10, however the variation is much smaller than that seen for the acceleration sweep. This is possibly an effect of the varying rate of heat transfer locally affecting the flow Mach number in the inducer as well as hysteresis in the formation of the shock. Since the shroud temperature increases through the impeller, the rate of heat transfer will also increase. the effect of which is amplified by the higher shroud temperatures present in the deceleration sweep leading to the observed hysteresis in the transition speed of the various Kulites. The magnitude of the unsteadiness also increases through the impeller, which is simply a byproduct of the increasing static pressure through the impeller resulting in the higher magnitude pressure fluctuations as the location shifts downstream.

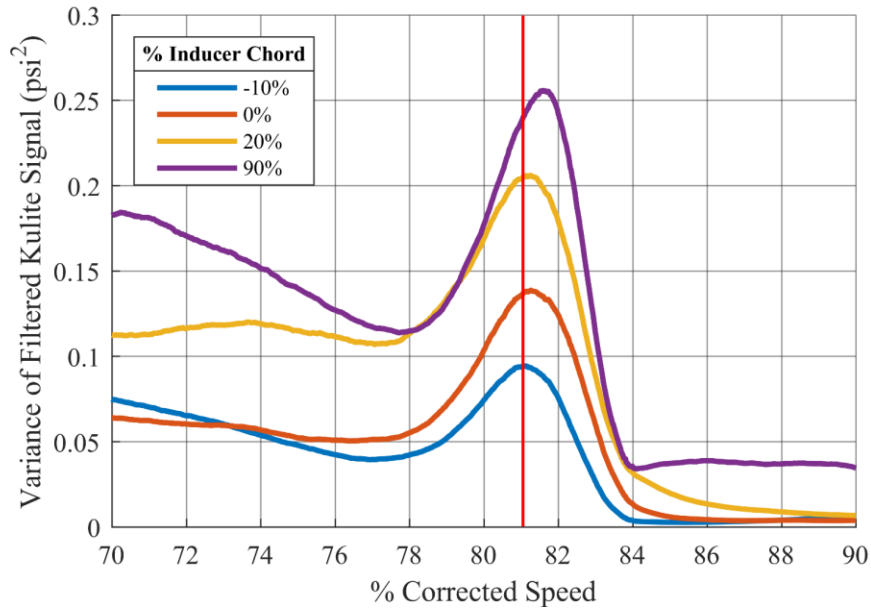


Figure 4.9 Variance of filtered impeller shroud Kulite signals at various meridional locations for acceleration sweep along mid-choke throttle line

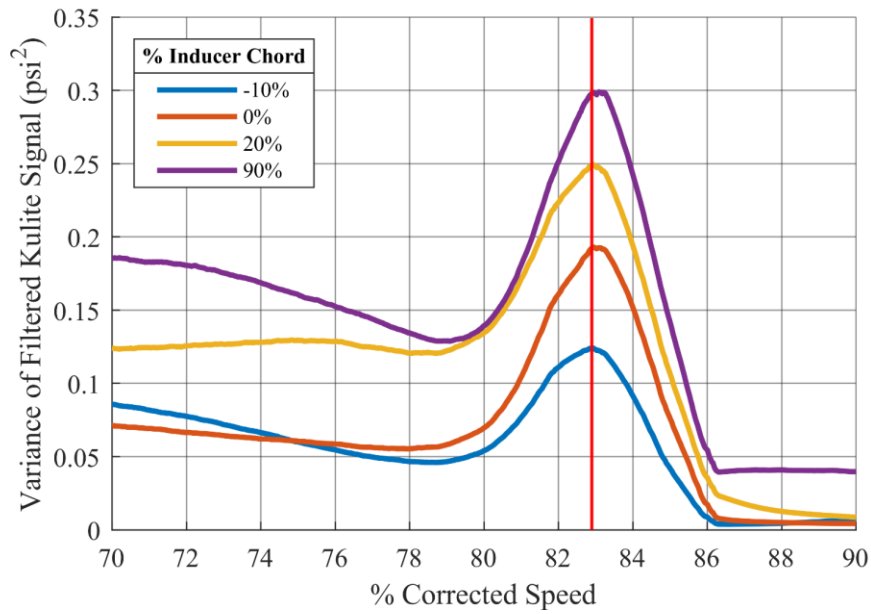


Figure 4.10 Variance of filtered impeller shroud Kulite signals at various meridional locations for deceleration sweep along mid-choke throttle line

Using the bare-bead thermocouples located just upstream of the impeller leading edge, it is possible to characterize the relative degree of recirculation [1] based on the ratio of the flow

temperature to the inlet temperature. If there is a high degree of recirculation, the ratio will be higher as the recirculating flow has work input from the impeller as well as increased heat transfer from the shroud due to the longer residence time. The leading edge flow temperature can also be used as an indicator of rotating stall in the inducer, as the stall cell has a higher flow temperature due to the recirculating flow within it. Figure 4.11 shows a trace of the temperature ratio for the mid-choke acceleration sweep. The results indicate that the recirculation in the impeller inlet is highest for speeds at and below $\sim 75\% N_c$, above which there is a steep decline. The recirculation then remains relatively low from $\sim 85\% N_c$ through the compressor's design speed. It is not immediately clear if this behavior is related to the transition observed in the Kulites, as the decrease in recirculation begins at a lower speed than the decrease in low frequency oscillations observed previously. While the decrease in the Kulite unsteadiness occurs at a higher speed, the speed at which the transition in temperature ratio begins, is nearer the speed where the main blade passing frequency becomes dominant in Figure 4.7, which is approximately $75\% N_c$.

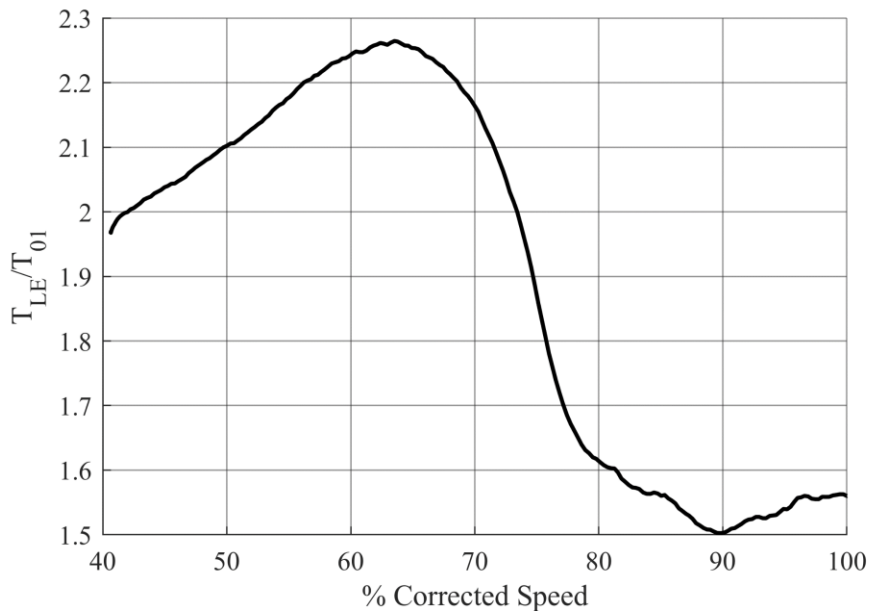


Figure 4.11 Ratio of flow temperature at impeller leading edge to inlet total temperature for acceleration sweep along mid-choke throttle line

Figure 4.12 depicts the temperature ratio during a deceleration sweep, for which the decrease in the magnitude of recirculation in the inducer begins at a slightly higher corrected speed, $\sim 70\% N_c$ vs $\sim 65\% N_c$ for the accel case. This shift in speed indicates that the phenomenon driving the change in recirculation has hysteresis which may be due to the change in the magnitude of heat

transfer, which is one of the dominant differences between the acceleration and deceleration cases. These results indicate that both the change in recirculation and the change in the unsteady pressure field in the inducer are being driven by the same flow phenomenon, which is believed to be related to the development of the shock in the inducer. It should also be noted that the magnitude of the temperature ratio is higher for the deceleration case, which is likely from the higher casing temperature resulting in an increased flow temperature at the inducer due to the higher rate of heat transfer for the deceleration compared with the acceleration case.

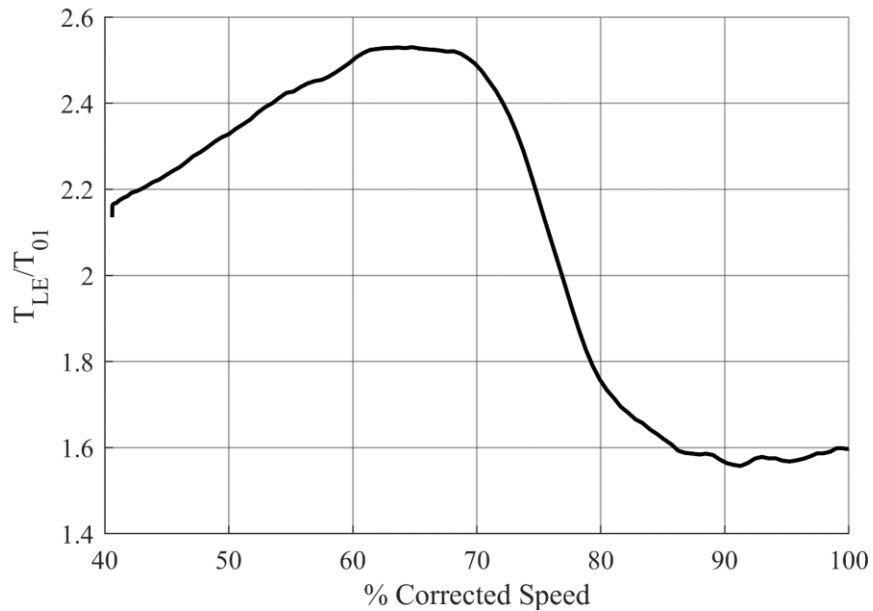


Figure 4.12 Ratio of flow temperature at impeller leading edge to inlet total temperature for deceleration sweep along mid-choke throttle line

Similarly, Figure 4.13 compares the temperature ratio for two acceleration sweeps at different throttle positions. The inflection point of the op-line sweep occurred at a lower speed than that of the mid-choke sweep, which would indicate a similar dependence on mass flow rate as discussed previously for the change in the Kulite response during speed transients.

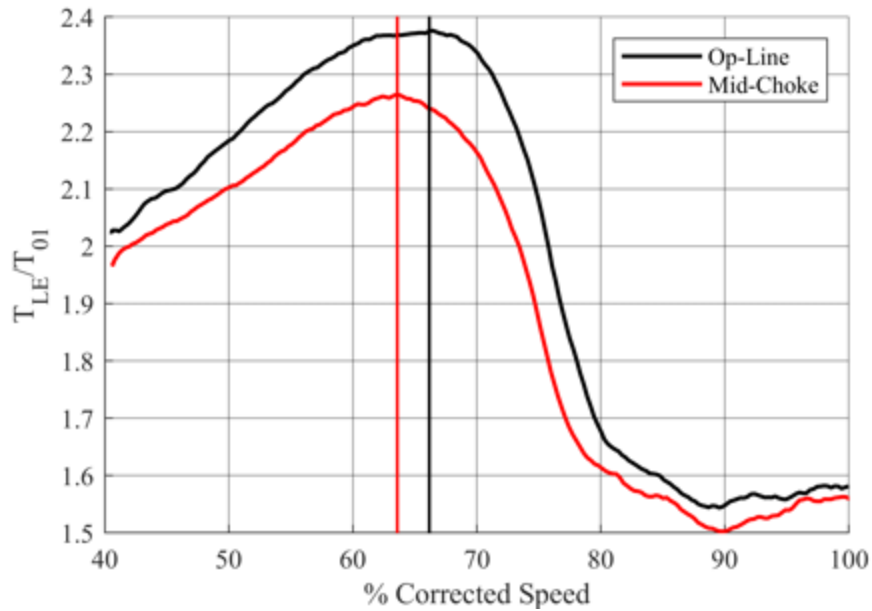


Figure 4.13 Comparison of impeller leading edge temperature ratio for acceleration sweeps along mid-choke and op-line throttle settings

4.1.2 Transient Compressor Performance

The effect of the subsonic-to-transonic transition is not isolated to variations in the unsteady pressure field, as there is also a significant change in the overall performance of the impeller. Figure 4.14 shows that there is a nearly three percent increase in the transient isentropic efficiency of the impeller from 75% to 90% of the design speed. Additionally, the speed at the beginning of the efficiency increase corresponds to the speed at which the main blade passing frequency begins to dominate at the impeller leading edge as depicted in Figure 4.7. The transient performance data should only be used qualitatively, as the compressor performance is affected by more than just the inlet relative Mach number during a sweep. Unlike when steady data were collected, several parameters affecting performance vary during the sweep, including tip clearance, bleed flow rates, and casing temperatures, all of which will have an impact on performance and are compounded by the relatively slow response of the thermocouples used to calculate efficiency. However, while the values of the deltas may be different than the steady data, the overall trend should be consistent, allowing some observations to be made. As the compressor approaches the transition speed, there are two significant changes: the main blade passing frequency begins to dominate the inducer flow field, and the impeller isentropic efficiency begins to increase. After

reaching a maximum efficiency at approximately 88% N_c , the efficiency briefly levels off before decreasing as the design speed is approached. It would appear that the initial change in the flow field during the transition to the transonic regime is beneficial to the impeller, but as the speed continues to increase the adverse effects of high inlet relative Mach numbers begin to dominate and the performance decreases as speed continues to increase. This decrease in efficiency at higher speeds is likely due to increasing shock losses or increased strength of the shock interactions causing greater loss through the impeller.

Figure 4.15 depicts the behavior of the impeller total pressure ratio during an acceleration sweep along the mid-choke throttle line. Rather than seeing the steep increase near the transition speed that was observed with efficiency, the total pressure ratio smoothly increases with speed. This result is not surprising, as the total pressure rise through the impeller is governed primarily by the rotational speed as discussed in Chapter 1. There is, however, a change in the slope of the total pressure ratio curve near the 85% transition speed, highlighted in red, where the rate of increase in total pressure ratio becomes nearly linear, rather than the quadratic increase at speeds below 85% N_c . This change in slope is likely associated with the total pressure loss caused by the shock in the inducer. As the compressor operating speed increases, so too does the strength of the shock, leading to increased total pressure loss, which results in the reduced rate of increase of impeller total pressure as compared with the subsonic regime. It should also be noted that although the total pressure loss is increasing in this region, the impeller efficiency is still increasing. This would indicate that the additional loss incurred due to the formation of the shock is mitigated by the change in the structure of the impeller flow field, resulting in a net increase in impeller efficiency during and after the transition from subsonic to transonic operation. However, as the speed continues to increase above ~95% N_c the impeller efficiency begins to decrease, which would indicate that the losses associated with the shock or its interactions become dominant and result in lower efficiency. Figure 4.16 allows for the change in slope to be analyzed more quantitatively, where the slope of the impeller total pressure rise is shown as a function of the corrected speed. The region highlighted in red corresponds to that of Figure 4.15. The rate of change of the slope of the TPR curve begins to increase at approximately 75% N_c , which corresponds to the speed at which the efficiency begins to increase. Upon reaching the transition speed at 85% N_c , it decreases slightly and then remains relatively constant for the remainder of the acceleration. Therefore, the step decrease in instability and the decrease in the slope of the total

pressure rise are likely a result of the same phenomena and both occur near the speed at which the impeller becomes transonic. Therefore, the formation of the shock has a deleterious effect on the impeller total pressure rise, while having a beneficial effect on the stability of the machine.

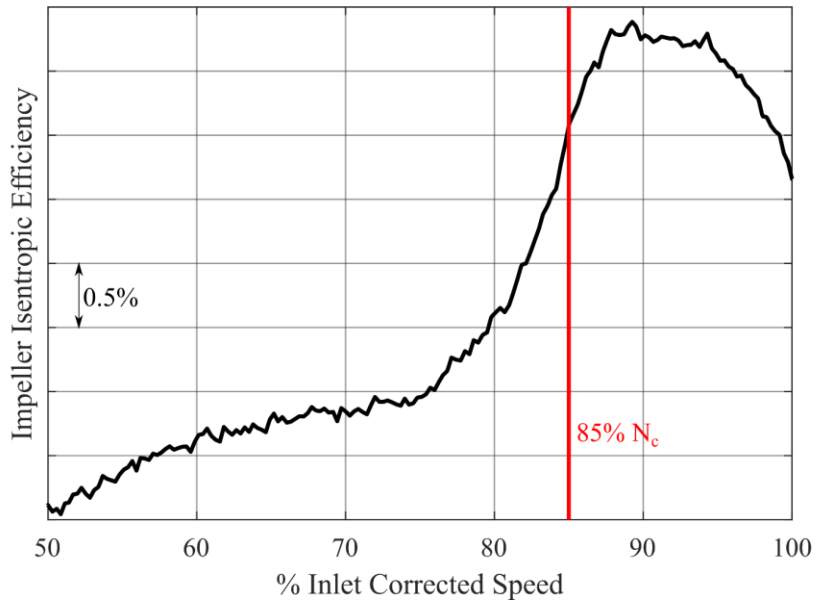


Figure 4.14 Impeller efficiency during acceleration sweep along mid-choke throttle line

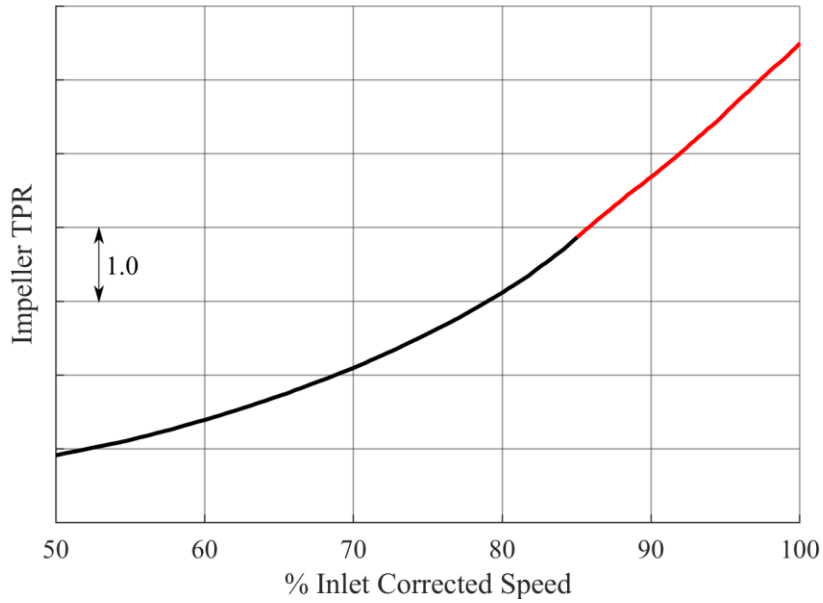


Figure 4.15 Impeller total pressure ratio during acceleration sweep along mid-choke throttle line

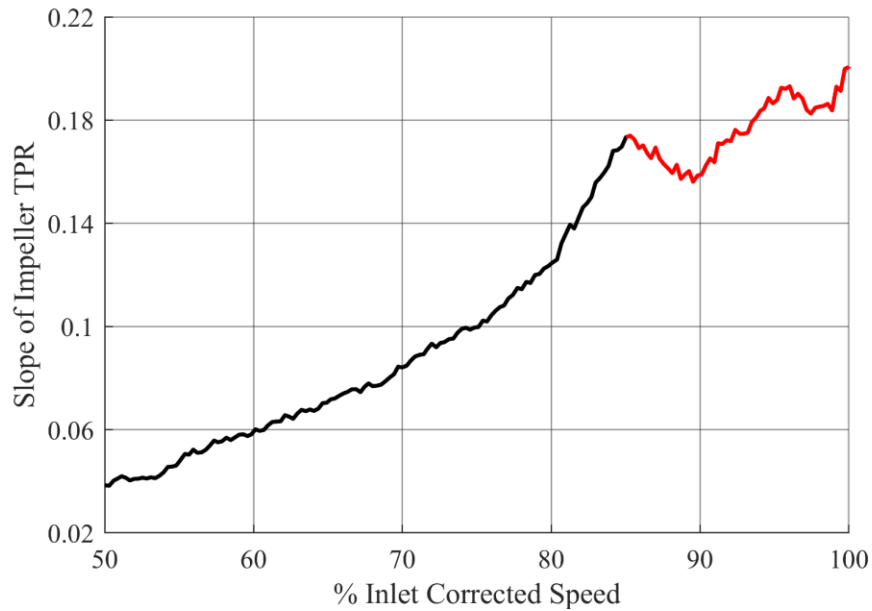


Figure 4.16 Slope of impeller total pressure ratio for acceleration sweep along mid-choke throttle line

4.2 Steady Data

In order to gather a more detailed view of the effect of the subsonic to transonic transition on compressor performance, steady state points were acquired in 0.5% N_c speed increments from 75% to 92% N_c along the two throttle lines, as shown in Figure 2.8. Since these data were recorded after the compressor temperatures had equilibrated, they provide a more representative view of the compressor's steady state performance at a given speed and throttle setting.

4.2.1 Inducer Relative Mach Number

Using the method described in section 3.2.1, it is possible to calculate the shroud isentropic relative Mach number at a Kulite location. To determine the maximum Mach number in the blade passage, the signal is ensemble averaged, and the minimum pressure in the average is used in the Mach number calculation. This minimum pressure corresponds to the region near the blade suction surface where the pressure is lowest and the Mach number is highest in the passage. Figure 4.18 and Figure 4.17 depict the isentropic relative Mach number at the impeller shroud in 4 different meridional locations for the mid-choke and op-line throttle conditions, respectively. From the results for the survey at the choke throttle setting, the leading edge Mach number reaches unity at

around 85% of the compressor’s design speed. This also corresponds to the speed at which the impeller instability decreases, providing further support for the sudden decrease in instability being related to the formation of the shock. The sharp increase in Mach number at 89% N_c for the 10% inducer Kulite corresponds to the speed at which the shock shifts downstream of the Kulite and, thus, exposes the Kulite to the lower pressure, higher velocity flow upstream of the shock. The lack of a corresponding increase in the leading edge Kulite would indicate that the shock never passes over this location and, therefore, must initially form downstream of the impeller leading edge. The Mach number at the furthest downstream location shown remains well below unity for the entire speed range, which is a result of the local speed of sound increasing through the blade passage due to the increased flow temperature and pressure. These Mach numbers are calculated using the assumption of isentropic flow in the impeller and do not account for the effects of heat transfer on the flow Mach number. Therefore, while giving an approximate value for the transition speed, the actual speed at which the compressor transitions from subsonic to supersonic flow is likely slightly lower than that calculated, due to the effects of heat transfer discussed previously.

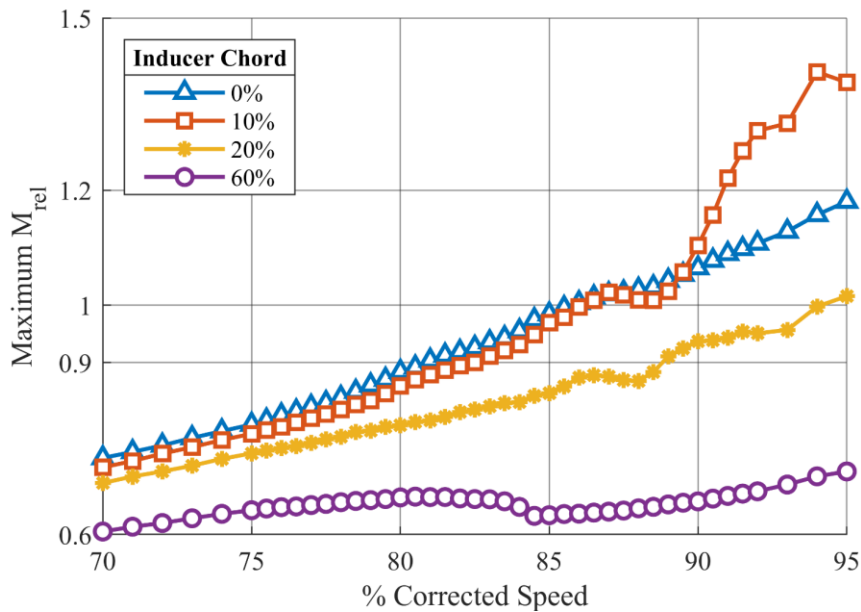


Figure 4.17 Isentropic relative Mach number at various locations in the inducer for the mid-choke survey

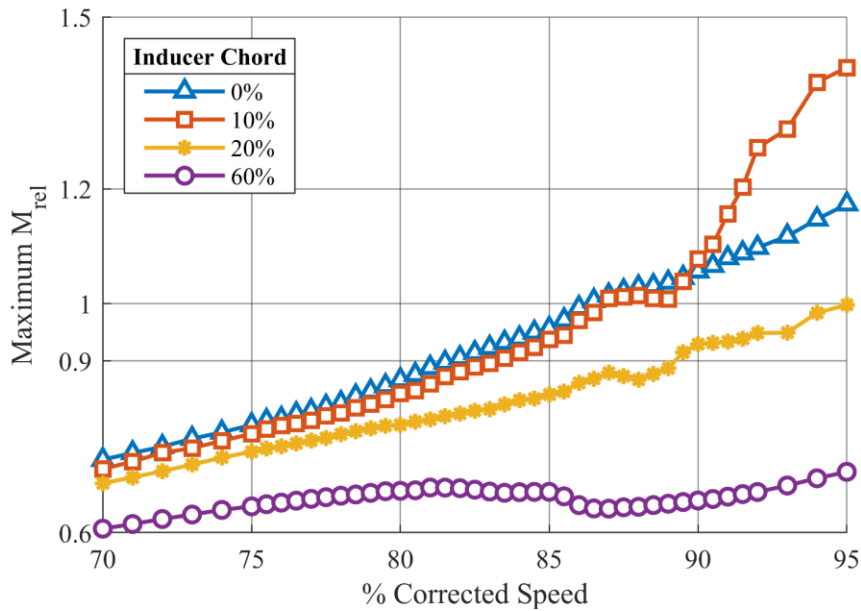


Figure 4.18 Isentropic relative Mach number at various locations in the inducer for the op-line survey

4.2.2 Steady State Performance

This section reviews the trends in performance observed for steady state testing along the two throttle lines and compares the results with the transient data results. Figure 4.19 depicts the isentropic efficiency of the impeller for the mid-choke throttle line survey, as well as the ratio of the leading edge flow temperature to the inlet total temperature. Similar to what was observed in the transient data, there is a 2.5 point increase in efficiency from 75% to 90% N_c , and the beginning of the efficiency increase coincides with the decrease of the temperature ratio. This would indicate that the efficiency increase is driven by the destruction of the flow recirculation upstream of the impeller leading edge. The inflection point in the efficiency curve occurs at a lower speed for the steady data than for the acceleration shown in Figure 4.14, which agrees with the idea that heat transfer is causing the shift in transition speed observed in the acceleration, deceleration and now also in the steady data. Also, the efficiency peaks at approximately 90% N_c followed by a decrease in efficiency are likely the result of increased losses associated with the impeller shock and its interactions with secondary flow structures. As with the transient data,

after its sudden decrease, the shroud temperature ratio remains relatively low for the remainder of the survey.

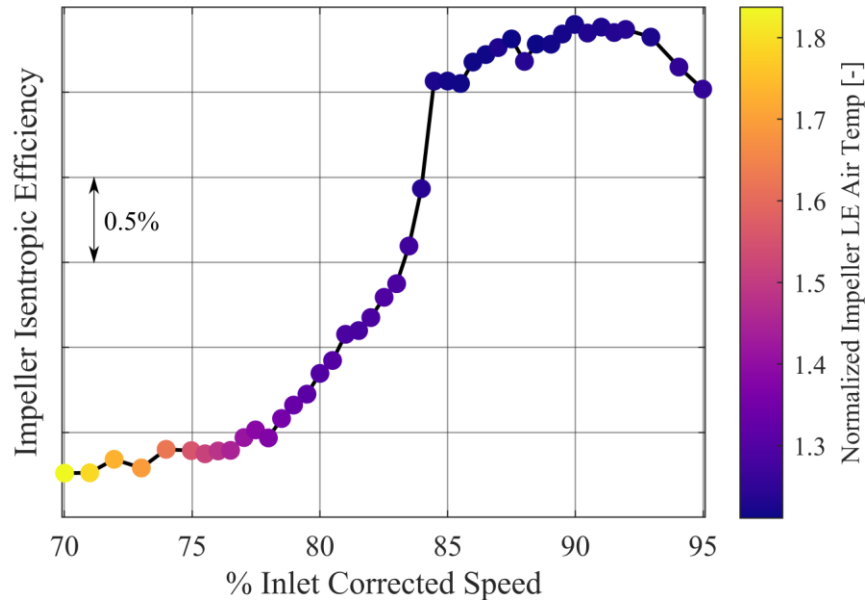


Figure 4.19 Impeller Isentropic efficiency for mid-choke throttle line survey where the data points are colored by the leading edge temperature ratio

Similarly, the impeller total pressure ratio shown in Figure 4.20 exhibits the same change in slope, however for the steady data, the change occurs at a slightly lower speed than for the transient data (84.5% vs 85%). The impeller total pressure ratio curve becomes nearly linear above the transition speed, as was observed in the transient data. This would indicate that the observed phenomena are not related to the non-equilibrium conditions present during the speed transient, but they are an effect of changes in the flow field related to the shift from a subsonic to transonic regime.

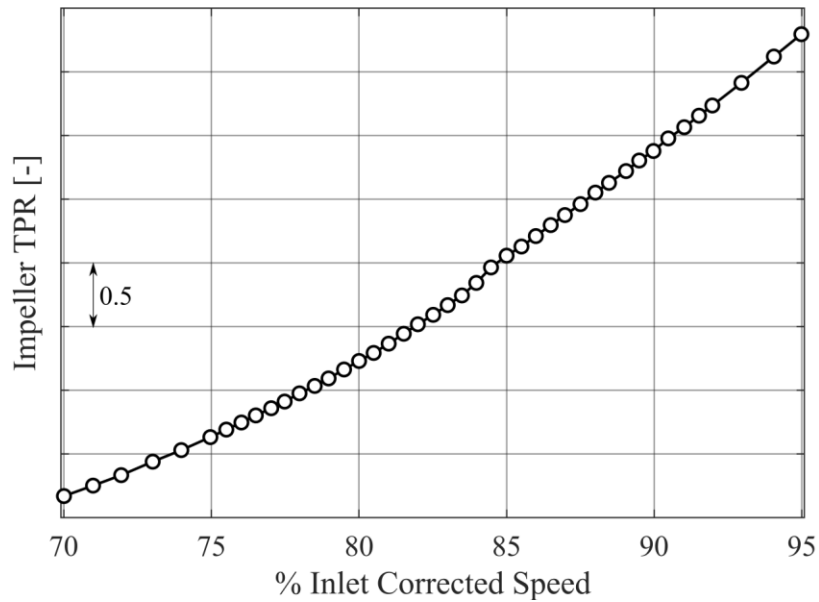


Figure 4.20 Impeller TPR for mid-choke throttle line survey

4.2.3 Unsteady Pressure Measurements

The observed change in the Kulite response during speed transients is also present in the steady state data. The results in Figure 4.21 show that the peak unsteadiness occurs at a slightly higher speed than for the acceleration sweep, but the sharp decrease still occurs at $\sim 84\% N_c$, which corresponds closely with the inflection point in the efficiency in Figure 4.19. As shown previously, upon transition to the transonic regime, the flow unsteadiness decreases significantly, especially at the sensors located near the impeller leading edge. The furthest downstream Kulite showed a similar decrease but remained at a higher level of variance after the transition than the Kulites located further upstream. This may indicate that the source of the unsteadiness is downstream of the inducer and upon formation of the shock, this unsteady flow field is no longer able to propagate as far upstream through the impeller.

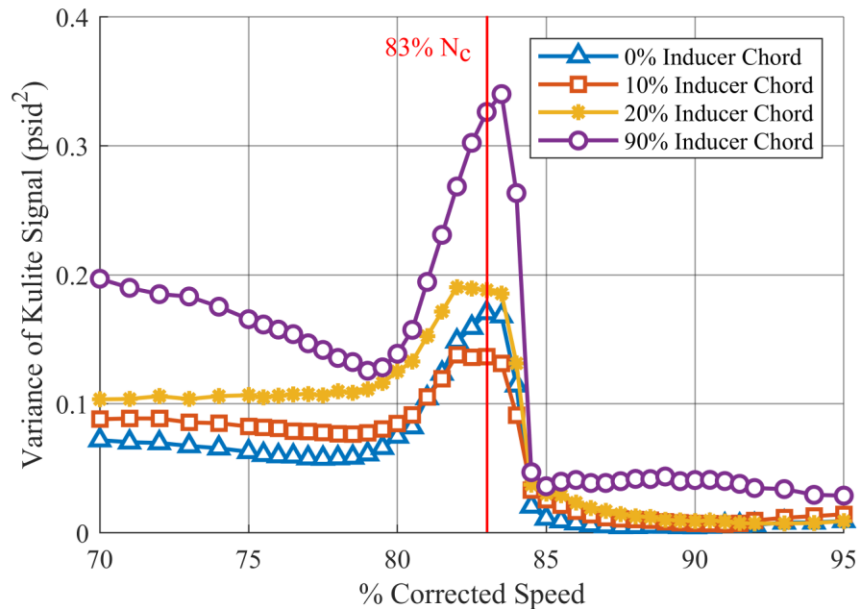


Figure 4.21 Variance of filtered Kulite signal for mid-choke throttle line survey

Rather than using Campbell diagrams, as was done with the transient data, because the steady points having larger discrete steps in speed, the frequency content of the Kulite signals was analyzed using waterfall plots. These three-dimensional plots show the frequency on the x-axis, corrected speed on the y-axis, and the response amplitude on the vertical axis. As with the Campbell diagrams, this visualization allows for the determination of the major frequency components in the flow, and whether discrete frequency components or broad band frequency content govern the behavior of the flow. Figure 4.22 through Figure 4.24 show the amplitude spectra for the impeller leading edge Kulite for the survey along the mid-choke throttle line, with the amplitude corresponding to the 80% to 85% N_c speed range highlighted in red. The first figure clearly shows the amplitude of the 17 engine order blade passing event undergoing a significant increase in amplitude at 75% N_c and increasing until 85% N_c after which it maintains a relatively steady amplitude. There is very little frequency content above the blade passing frequency with the exception of the first harmonic shown at 34 engine order. Figure 4.24 provides a magnified view of the sub 10 engine order frequency content. This shows a broadband low amplitude content exists in the flow at speeds below 85% N_c , as was evident in the transient Campbell diagrams. However, the waterfall plots show a region of higher amplitude content around the 8 engine order frequency, which was not present in the transient data. It is possible that the instability is the result

of the upstream propagation of a disturbance from the exducer of the impeller where the flow field is more turbulent compared with the inducer. This downstream instability could then propagate upstream and destabilize the inducer resulting in the observed pressure fluctuations near the impeller leading edge. As was observed in the study by Reference [26], a pressure wave propagating through the impeller resulted in significant changes in the flow field at the impeller leading edge, especially when the rotational speed and the frequency of the propagating wave resulted in resonance. This may be the cause of the observed instability in this case, however without unsteady pressure measurements in the rotating domain, it is not possible to track these disturbances through the impeller. There is a larger magnitude peak at approximately 1.5 engine order, which is the result of a rotating instability in the inducer. This was also seen in both the acceleration and deceleration sweeps. The sub 17 engine order responses all rapidly decay above 84% N_c , indicating that the formation of the shock in the inducer is removing these features from the impeller flow field.

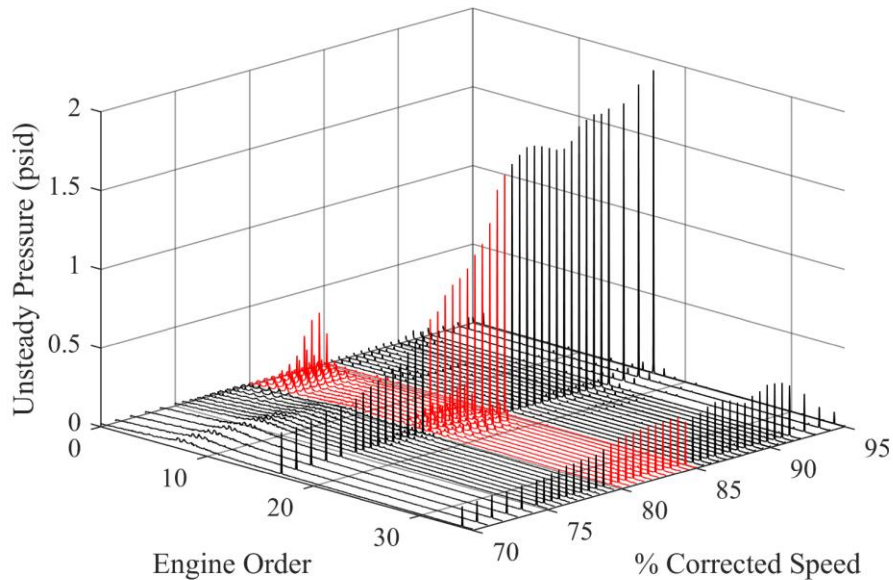


Figure 4.22 Waterfall of impeller leading edge Kulite frequency spectra for mid-choke throttle line survey showing frequency content up to 35 times the rotational frequency

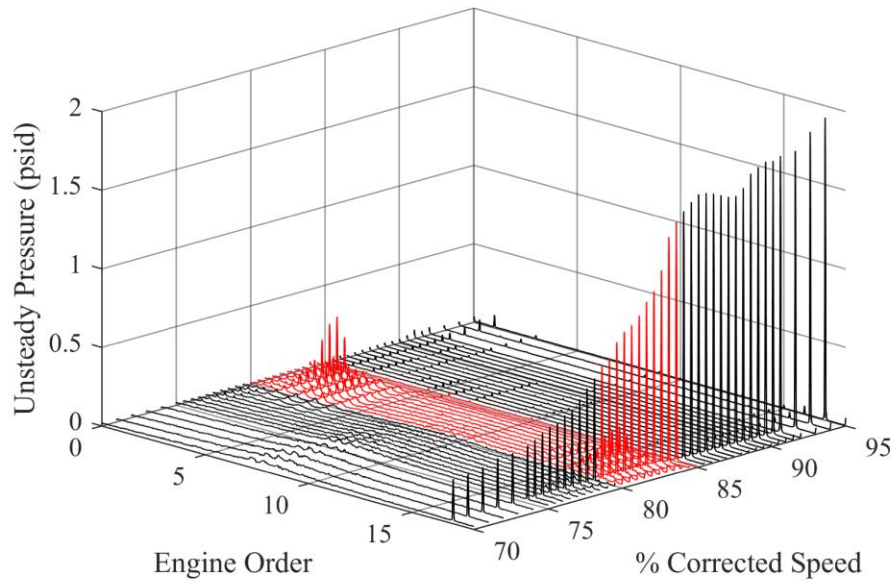


Figure 4.23 Waterfall of impeller leading edge Kulite frequency spectra for mid-choke throttle line survey showing frequency content up to 18 times the rotational frequency

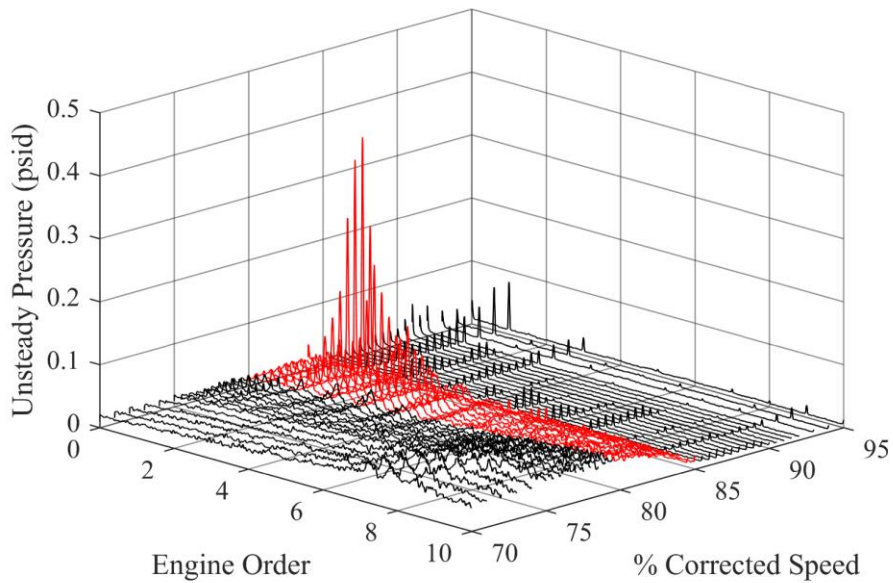


Figure 4.24 Waterfall of impeller leading edge Kulite frequency spectra for mid-choke throttle line survey showing frequency content up to 10 times the rotational frequency

Figure 4.25 through Figure 4.27 show the amplitude spectra of a Kulite located in the vaneless space between the impeller trailing edge and diffuser leading edge. Unlike the spectra of the inducer Kulite discussed previously, the flow field is dominated by low frequency components for the entire speed range with the blade passing frequency (34 engine order in the exducer) remaining relatively low throughout. As with the impeller Kulites, the peaks at approximately 1.5 engine order correspond to a rotating instability that propagates through the compressor, which upon reaching the transition speed of $\sim 84\% N_c$ disappears from the signal. However, unlike the impeller Kulite, the broadband, low-frequency components of the signal remain after transition and are observed to increase in amplitude for the remainder of the speed range as shown in Figure 4.27. This supports the hypothesis that the disturbance is originating downstream of the inducer and propagating upstream to the impeller leading edge resulting in the observed instability.

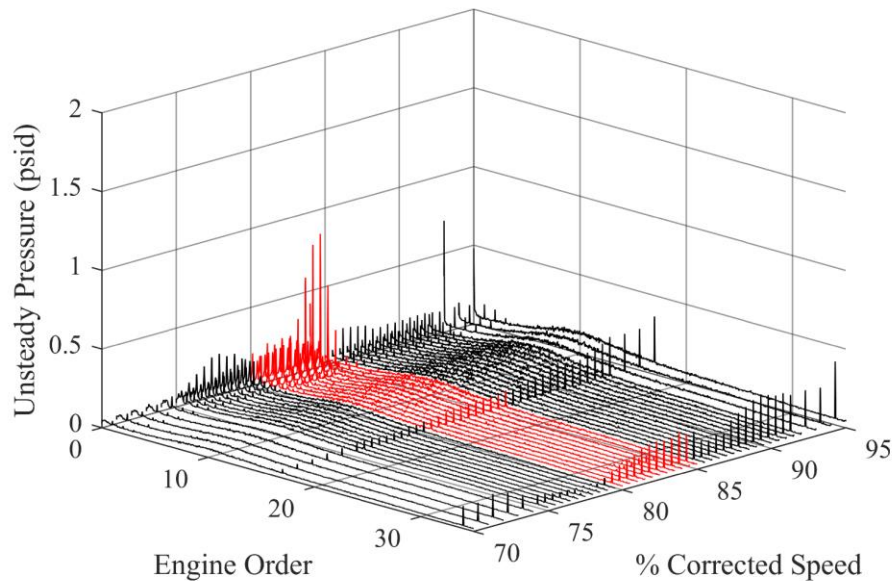


Figure 4.25 Waterfall of vaneless space Kulite frequency spectra for mid-choke throttle line survey showing frequency content up to 35 times the rotational frequency

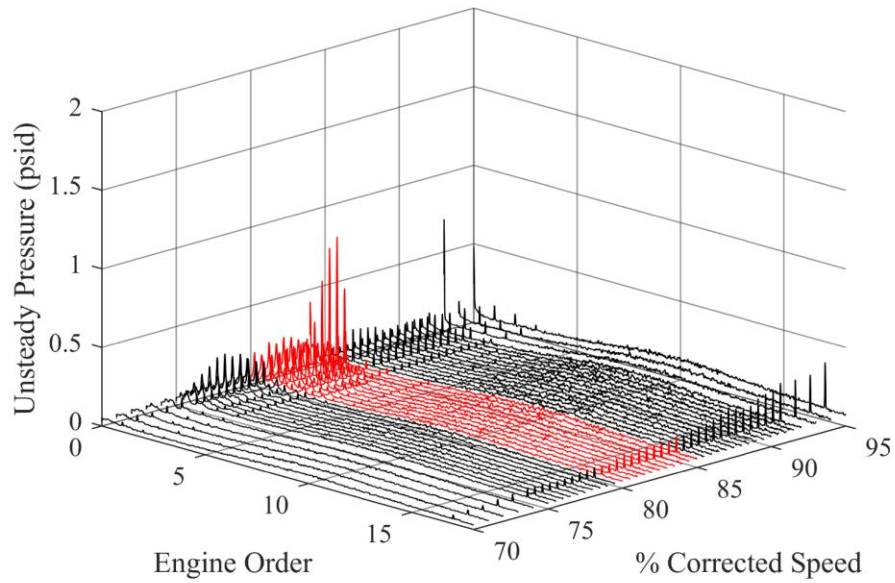


Figure 4.26 Waterfall of vaneless space Kulite frequency spectra for mid-choke throttle line survey showing frequency content up to 18 times the rotational frequency

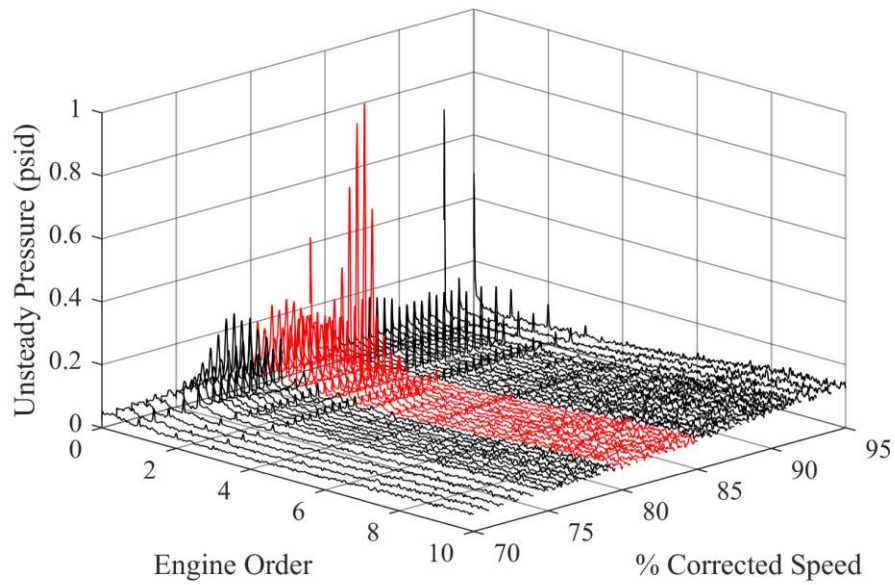


Figure 4.27 Waterfall of vaneless space Kulite frequency spectra for mid-choke throttle line survey showing frequency content up to 10 times the rotational frequency

To further investigate the effect of throttle position on the unsteadiness in the flow field, a waterfall of Kulite spectra was made for points along the 85% N_c speedline. Figure 4.28 and Figure 4.29 show the spectra of the leading edge impeller Kulite response corresponding to steady points from choke to the last stable point prior to stall. There are a few interesting features that are worth noting. First, the 1.5 engine order response disappears as the compressor is throttled out of choke and up to the op line, as shown in Figure 4.29. Second, the amplitude of the response corresponding to the blade passing frequency decreases from choke to stall, as shown in Figure 4.28. Finally, the broadband, low-frequency content increases in amplitude as the compressor is throttled along the speedline. The first observation can be explained by considering the trend shown in Figure 4.30, where the speed at which the variance peaks increases with increasing throttle position. Due to the relatively high amplitude of the 1.5 engine order response, the peak of the variance plot is dominated by this response, and it can, therefore, be concluded that the formation of the 1.5 engine order response shifts to higher speeds as the compressor is throttled. Consider a speedline to represent a vertical line in Figure 4.30, where the response is present when the compressor is choked. Then as the throttle is closed, the speed at which the response occurs will eventually be shifted above the current operating speed, and the response will decay as was observed in Figure 4.29. The behavior of the blade passing frequency component is unexpected as this response approximately corresponds to the pressure differential from the suction surface of the blade to the pressure surface, and as was shown in Figure 4.4, decreasing mass flow rate should result in increased incidence and, therefore, increased blade loading due to the greater fluid acceleration to the suction surface of the blade. Figure 4.31 shows a similar waterfall for the 100% N_c speedline, where the expected behavior is observed, that is, the pressure differential across the blade increases as the throttle closes. Because, as shown in Figure 4.28, the increasing incidence at the impeller leading edge is not resulting in the expected change in blade loading, another factor must be dominating the behavior in the impeller for the lower speed case. The decreasing mass flow rate is driving the decrease in the blade passing frequency response, which agrees with the observations from Figure 4.23, where the amplitude of the blade passing response was shown to increase dramatically in the 80% to 85% N_c speed range.

As it has been established that the formation of the shock in the inducer has a significant impact on the behavior of the impeller, it is possible that the observed changes in the 17 engine order response are the result of the decreasing mass flow rate altering the structure of the shock. If

the mass flow rate is decreased sufficiently along the 85% speedline, the impeller may be driven back into a subsonic operating regime causing the extent of the shock to decrease. This is supported by the increase in amplitude of the broadband content in the Kulite signal which is believed to originate downstream of the inducer and is only able to propagate upstream when the shock is absent. It is also possible that the decreased shock strength resulting from the lower mass flow rate is causing a reduction in static pressure rise and, therefore, resulting in the observed decrease in the blade passing frequency response. The effect of throttling on the relative Mach number is shown in Figure 4.32, where the relative Mach number at the impeller leading edge is shown to decrease with decreasing flow coefficient along the 85% speedline. It should be noted that the Mach number shown is not fully representative of the actual Mach number as it assumes isentropic flow in the inducer, however the trend remains valid. As will be discussed in more detail in the next chapter, the flow near the shroud may be subsonic even though the impeller is operating in a transonic regime due to endwall effects reducing the relative velocity in this region.

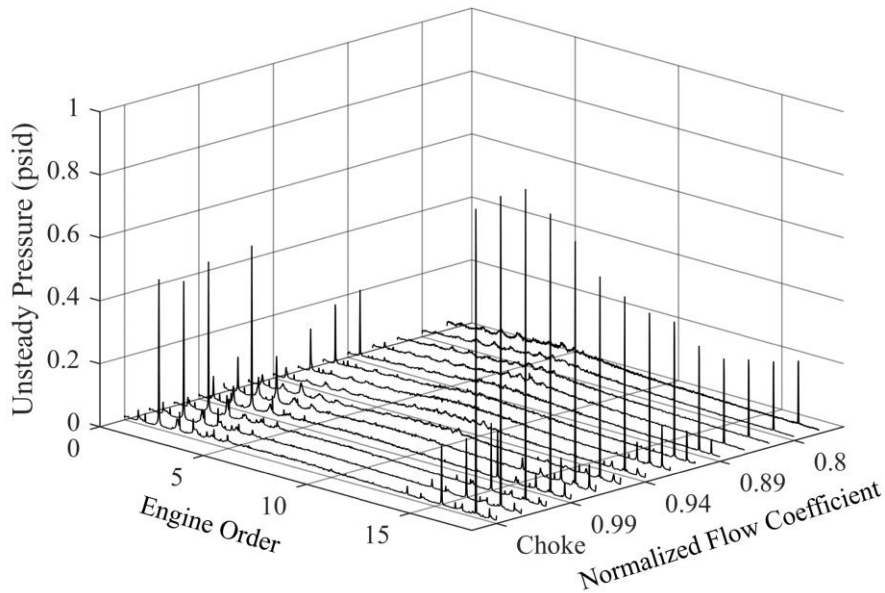


Figure 4.28 Waterfall of leading edge Kulite amplitude spectra along 85% N_c speedline showing frequency content up to 18 engine order

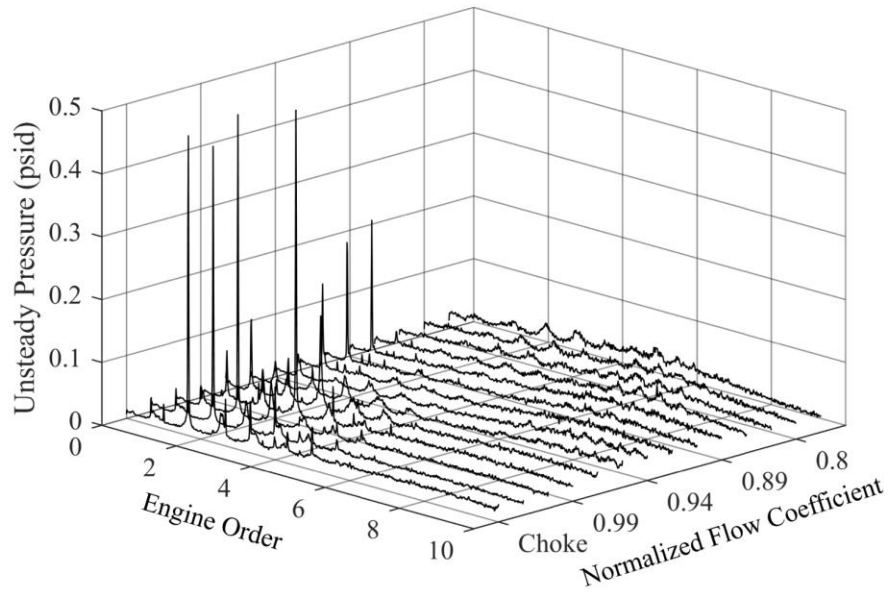


Figure 4.29 Waterfall of leading edge Kulite amplitude spectra along 85% Nc speedline showing frequency content up to 10 engine order

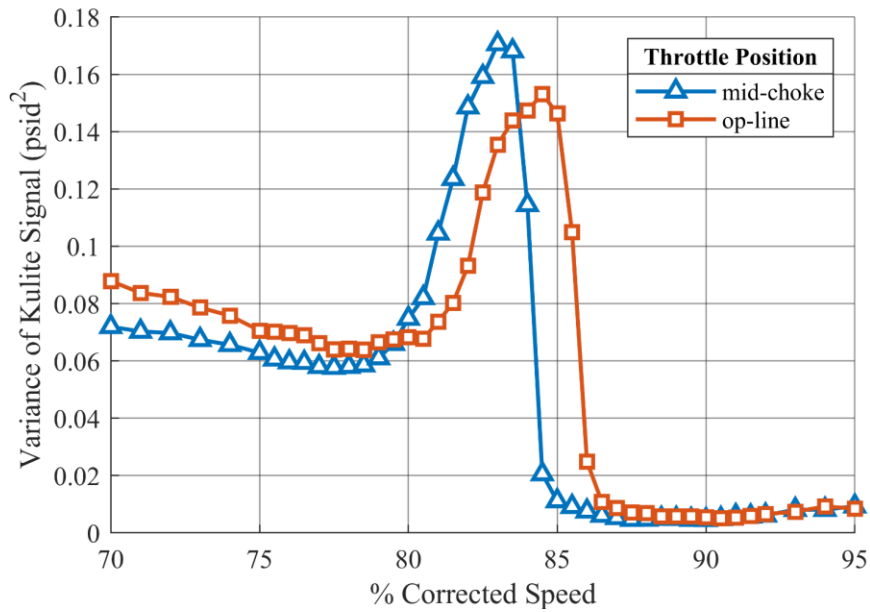


Figure 4.30 Comparison of variance in leading edge Kulite signal with changing throttle position

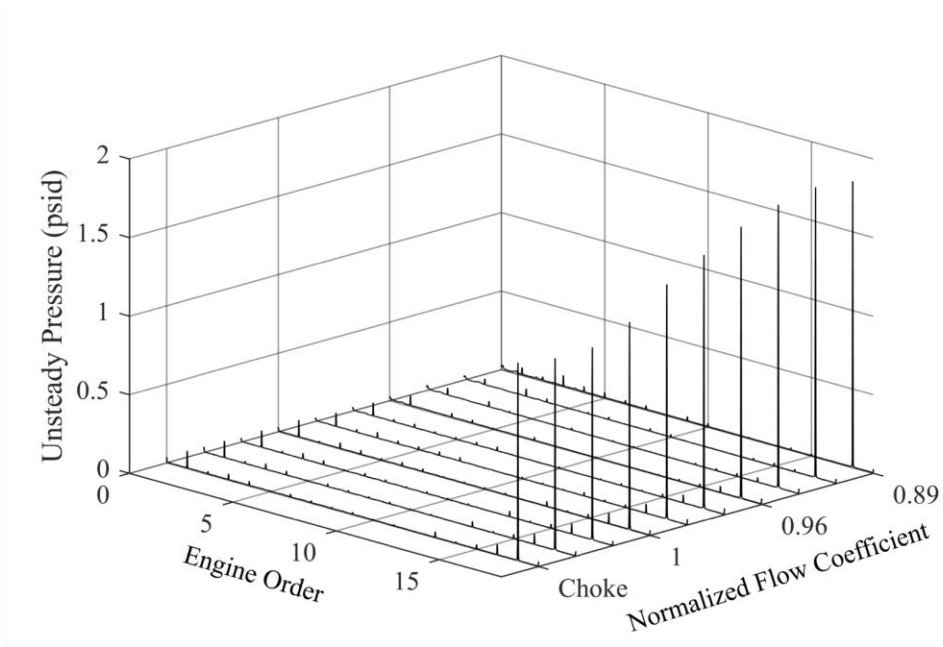


Figure 4.31 Waterfall of leading edge Kulite amplitude spectra along 100% Nc speedline showing frequency content up to 18 engine order

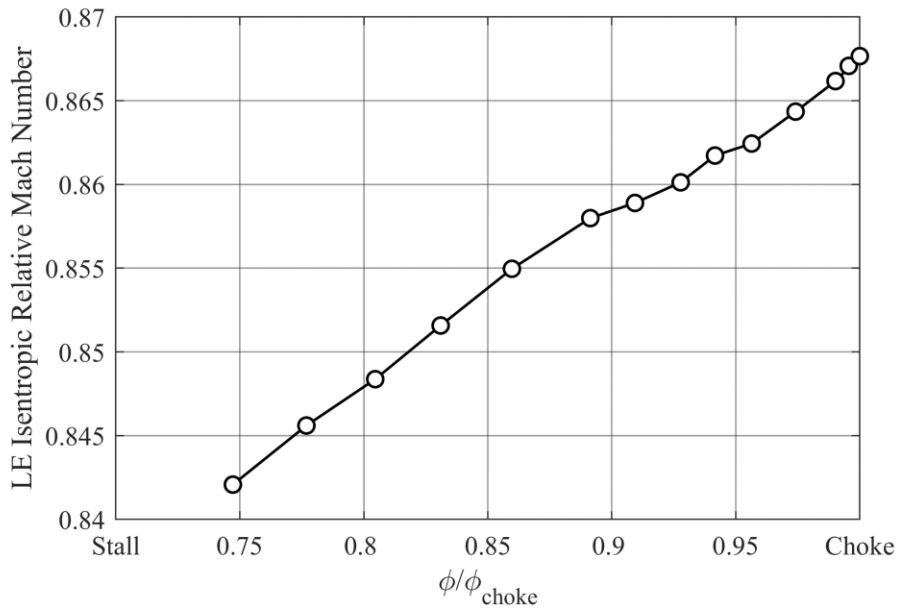


Figure 4.32 Effect of throttle position on the impeller leading edge relative Mach number

4.2.4 Component Stability

To determine which component of the compressor is driving the machine to become unstable, the static-to-static pressure coefficient is calculated using equation (4.1). As shown in

[31], [32] it is possible to determine the stability of compressor components using the slope of the pressure coefficient with respect to the compressor flow coefficient. For negative slopes, the component has a stabilizing effect on the system as whole, whereas positive slopes indicate that the component has a destabilizing effect.

$$\Psi_{(s-s, i-j)} = (P_j - P_i) / (1/2 \rho U_2^2) \quad (4.1)$$

As two surveys were taken at two different loading conditions, it is possible to calculate the slope of the pressure coefficient at all of the survey speeds, the method for which is given in equation (4.2). Since the change in flow coefficient, ϕ , will always be positive when going from a higher to lower throttle setting along a speedline (assuming the points are not both in choke), the sign of the slope is determined by the change in the static-to-static pressure coefficient.

$$(\Delta\Psi_{(s-s)})/\Delta\phi = (\Psi_{(s-s, LO)} - \Psi_{(s-s, HI)})/(\phi_{LO} - \phi_{HI}) \quad (4.2)$$

Figure 4.33 shows the static-to-static pressure coefficient slopes for six regions in the impeller and diffuser. The red and blue regions of the background represent positive and negative slope, respectively, with a positive slope indicating a destabilizing effect and negative slope indicating a stabilizing effect of the component on the compressor. It should be noted that these plots indicate the stability of the components near the op-line, and that at lower flow coefficients, the stability of the compressor is primarily governed by the diffuser for this compressor. The inducer is destabilizing for the entire speed range shown. However, there is relative maximum near the 85% N_c transition speed above which the slope drops significantly. The semi-vaneless space and vaneless space show similar decreases above the transition speed, but these regions are stable across the entire speed range. The exducer oscillates between the positive and negative slope regions and has a neutral effect on the stability of the compressor as a whole. The diffuser exit region shows a gradual increase in instability across the speed range, with a slight increase in rate of change near the transition speed but no sharp decrease. These results support the previous discussion that the stability of the inducer is strongly influenced by the formation of the shock in the impeller passage. Immediately after formation, instability is increased, which may be the result of unsteadiness in the formation or location of the shock. As the speed of the impeller is increased further, there is a significant stabilizing effect in the inducer, which propagates through the vaneless space and diffuser passage, as these regions also show improved stability. Since the

inducer has a strong influence on the operating range of the compressor [1], it is logical that an improvement in the stability of the inducer would result in an improvement of the stability of components throughout the machine.

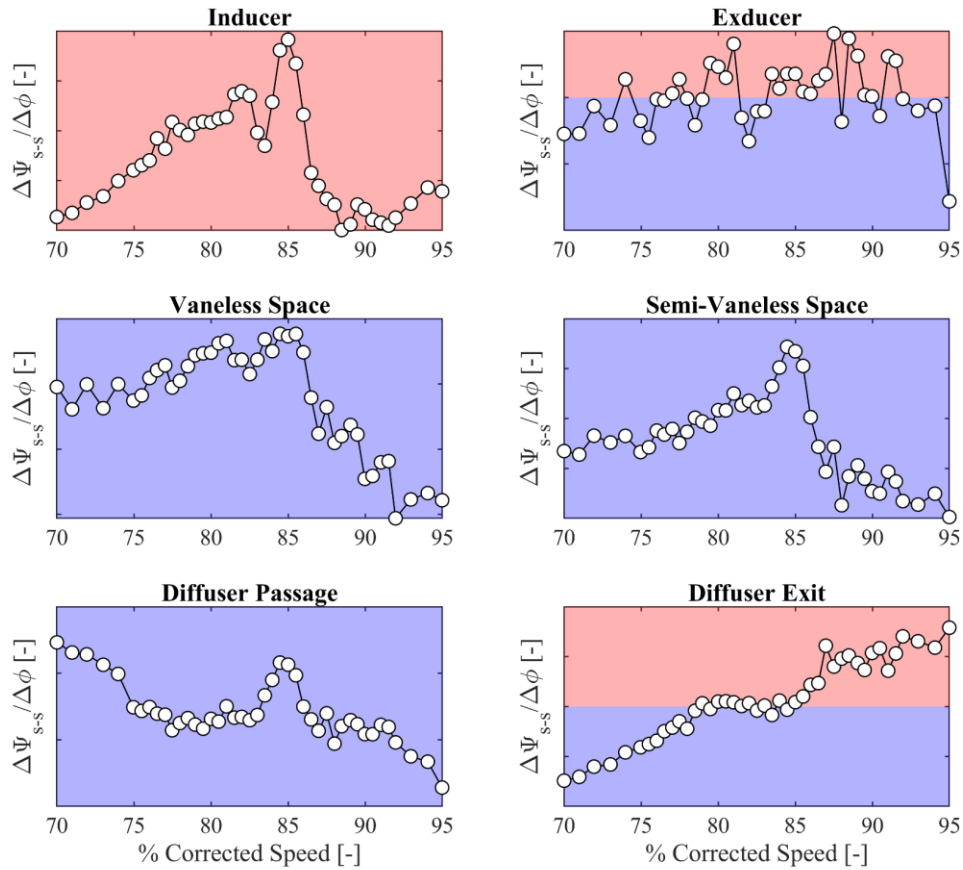


Figure 4.33 Slope of static-to-static pressure coefficient from mid-choke to op-line for multiple regions in the compressor, positive and negative slopes are indicated by the red and blue shaded regions respectively

4.2.5 Effect of Shock Formation on Tip Clearance Sensitivity

In addition to the observed changes in efficiency and stability as the compressor transitions from subsonic to transonic operation, the formation of the shock prevents transmission of information upstream through the impeller passage to the leading edge. As a result, the effect of changes downstream of the shock on the performance of the impeller will be diminished. The SSCC facility features the unique capability of varying the tip clearance of the impeller during operation, which

both allows for testing at a consistent clearance at all speed ranges as well as testing at various tip clearances to determine the effect on performance. Testing was conducted at a nominal clearance ratio, of ~4.3% the exit blade height as well as a larger clearance of ~7.2%. Because the clearance is adjusted by shifting the impeller in the axial direction, only the clearance downstream of the axial portion of the impeller is affected by adjusting tip clearance, with the inducer clearance being effectively constant. To compare the impeller performance at both clearances, points of similar loading must be selected from the two cases, otherwise effects from different incidence, etc. would muddy the results. The points were matched by selecting a point at the nominal clearance setting and then selecting the larger clearance point with the nearest throttle position. Using either the throttle position or the ratio of total pressure ratio to corrected mass flow rate resulted in the same point being selected. The tip clearance sensitivity was quantified by calculating the percent increase in impeller efficiency from the larger clearance condition to the smaller clearance as described in equation (4.3), where the subscripts TC1 and TC2 designate the nominal and larger than nominal clearances, respectively.

$$\% \text{ Increase } \eta_{imp} = (\eta_{(imp, TC1)} - \eta_{(imp, TC2)}) / \eta_{(imp, TC1)} \cdot 100 \quad (4.3)$$

This was done at the peak impeller efficiency point for speeds from 60% to 100% N_c , and the results are shown in Figure 4.34. It would be expected that the tip clearance sensitivity would increase across the speed range, as the increasing pressure differential across the blade results in increased tip leakage flow. However, the results show the sensitivity increasing up to 85% N_c , above which the sensitivity decreases to the design speed. A similar trend exists with the sensitivity of impeller total pressure ratio shown in Figure 4.35, where there is a decrease in the sensitivity to a change in tip clearance above 85% N_c . A possible explanation for this behavior is that the formation of the shock in the inducer prevents changes in the exducer flow field (that result from the changing tip clearance) from propagating upstream, thereby reducing the magnitude of the impact on performance. As mentioned previously, the tip clearance only changes in the exducer region of the flow field, and therefore, the inducer flow field would only be impacted if the flow disturbances at the exducer are able to propagate upstream through the impeller passage. As the compressor speed is increased, the inducer shock shifts downstream further decreasing the distance the downstream flow disturbances are able to propagate upstream and thereby reducing the effect of the change in clearance.

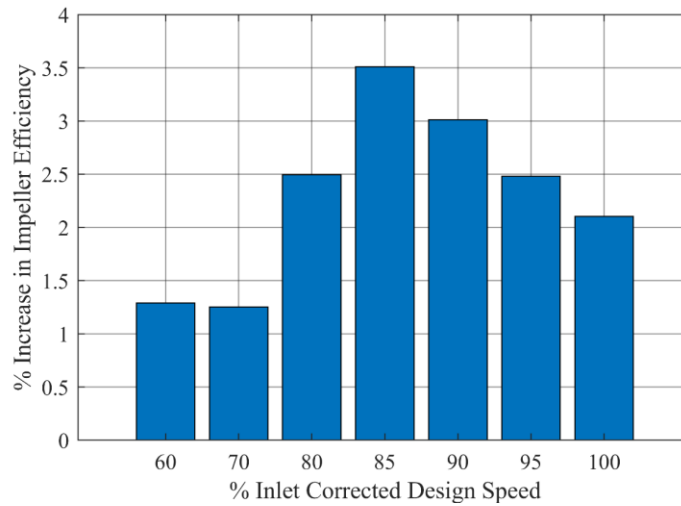


Figure 4.34 Variation in sensitivity of impeller efficiency to decreasing tip clearance for a range of operating speeds

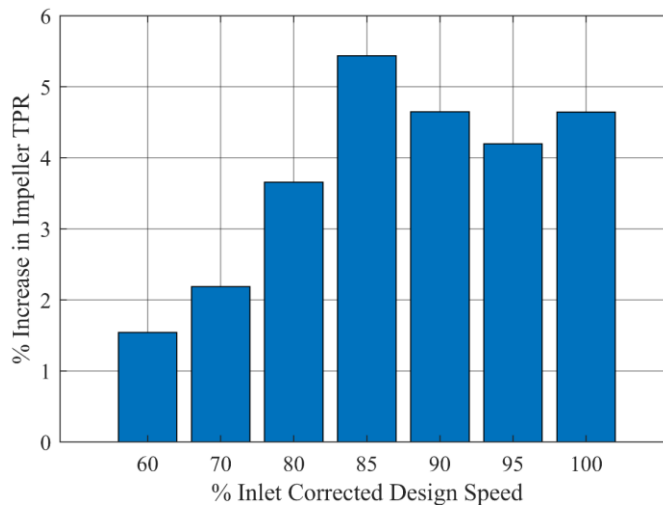


Figure 4.35 Variation in sensitivity of impeller total pressure ratio to decreasing tip clearance for a range of operating speeds

4.2.6 Inducer Flow Field

As both the efficiency and stable operating range of the impeller are determined in large part by the performance of the inducer, an understanding of the behavior thereof is of critical importance. The following section will discuss the flow structure in the inducer as well and how this structure changes as the compressor transitions from subsonic to transonic operation. In order

to visualize the inducer flow field, contour graphs of static pressure and isentropic relative Mach number are shown at various speeds using data obtained from the high frequency response Kulite pressure transducers located in the shroud of the impeller. In addition, contours of the rms pressure variation are included, which show the rms variation of the Kulite signal from the ensemble average of the signal over several hundred revolutions. This allows for observations to be made about where the unsteadiness in the pressure field is highest and how this unsteadiness changes with operating conditions. The contours of both Mach number and static pressure were made using the ensemble averaged pressure field for an impeller revolution made up of more than two thousand ensembles. There are only seven of the 17 blade passages shown to ensure that smaller flow details remain visible, and as a result of axisymmetric inflow, the passage-to-passage variation in the impeller is not significant.

Figure 4.36 is a contour of the shroud static pressure for the mid-choke operating point at 80% of the impeller design speed. A large region of low static pressure extends from the suction surface across the entire passage from the leading edge to 20% of the inducer chord. The cross-passage pressure gradient is relatively weak as indicated by the iso-pressure contour lines being nearly perpendicular to the streamwise direction. As the cross-passage pressure gradient is necessary to support the centrifugal acceleration caused by the streamline curvature required for the flow to be diffused in the relative frame, a weak pressure gradient is not desirable. Figure 4.37 depicts the same graph near the 85% N_c transition speed. The general structure of the flow field is significantly different, with a much stronger cross-passage pressure gradient, as indicated by the iso-pressure contour lines being nearly parallel to the streamwise direction. The low-pressure region is, however, still present in the blade passage near 10% inducer chord, but it is far less significant than for the 80% case.

Figure 4.38 depicts the static pressure at 90% corrected speed and is well into the transonic operating regime of the impeller. As with the 85% speed case, there is now an even stronger cross-passage pressure gradient indicating improved relative diffusion, and the low pressure region near the leading edge is now completely absent from the pressure field. Both of these changes should result in a significant enhancement of the performance of the inducer, which is supported by the impeller efficiency figures discussed in previous sections.

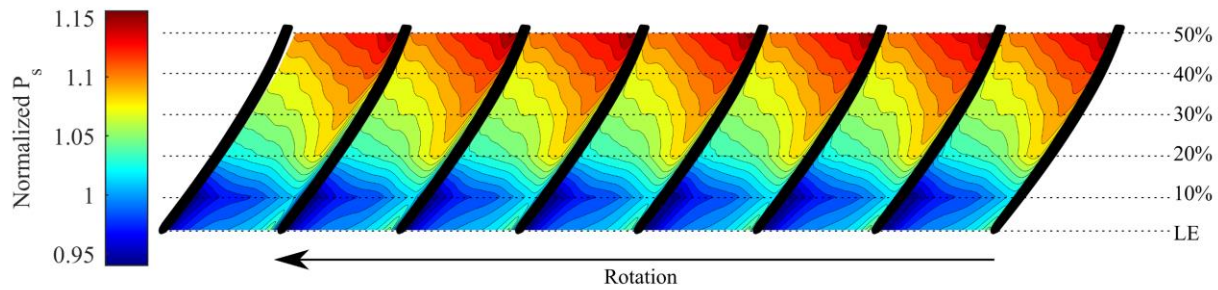


Figure 4.36 Contour of static pressure normalized by inlet total pressure in the inducer at 80% of the corrected design speed

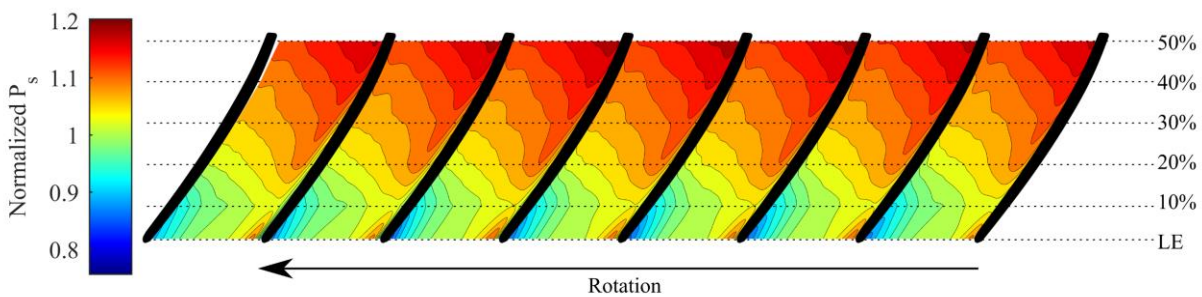


Figure 4.37 Contour of static pressure normalized by inlet total pressure in the inducer at 85% of the corrected design speed

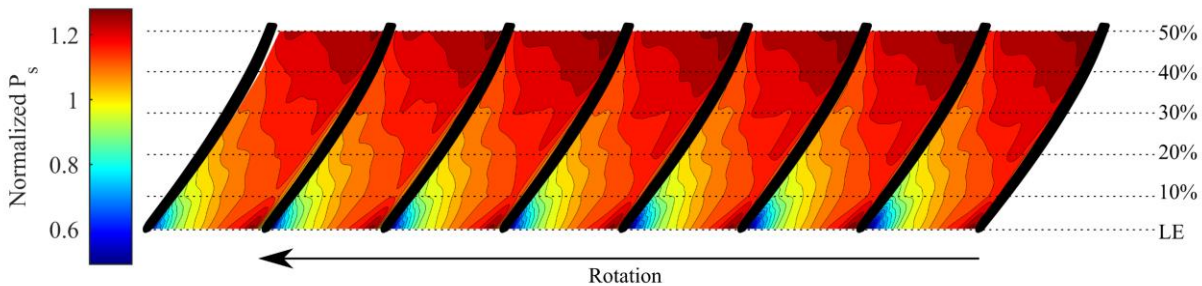


Figure 4.38 Contour of static pressure normalized by inlet total pressure in the inducer at 90% of the corrected design speed

Figure 4.39 through Figure 4.41 show contours of the isentropic relative Mach number at the inducer shroud for 80%, 85%, and 90% corrected design speed. As expected, the results show that the relative diffusion done in the inducer increases significantly with wheel speed. As with the static pressure contours, the 85% and 90% speed cases both have generally similar structures, whereas the 80% speed case shows a much weaker Mach number gradient in the inducer,

indicating less relative diffusion is being done. In Figure 4.40, the Mach number exceeds unity in some blade passages and does not in others, which could be contributing to the observed spike in unsteadiness in this speed range as the shocks are not yet fully formed for all of the blade passages resulting in significant passage to passage variation. The 90% speed case in Figure 4.41 shows the inducer doing significantly more diffusion in the relative frame as the relative Mach number decreases from a maximum of 1.4 at the leading edge to less than 0.8 at 20% chord, compared with the lower speed cases which showed significant diffusion continuing to occur at 40% chord and further downstream. Figure 4.42 and Figure 4.43 show contours of static pressure and isentropic relative Mach number, respectively, at 90% corrected speed for the last stable point on the speedline prior to stall inception. The Mach contour shows that the location of the shock has shifted upstream in the inducer to approximately 15% chord, while the Mach number near the suction surface leading edge has been reduced compared with the mid-choke case shown previously. The static pressure contour shows a large low-pressure region at 10% inducer chord, similar to the lower speed cases. It is possible that the decrease in mass flow rate is driving the inducer back to the less stable flow regime that was observed at 85% speed, which is supported by the structure of the static pressure field near the shroud more closely resembling the lower speed case.

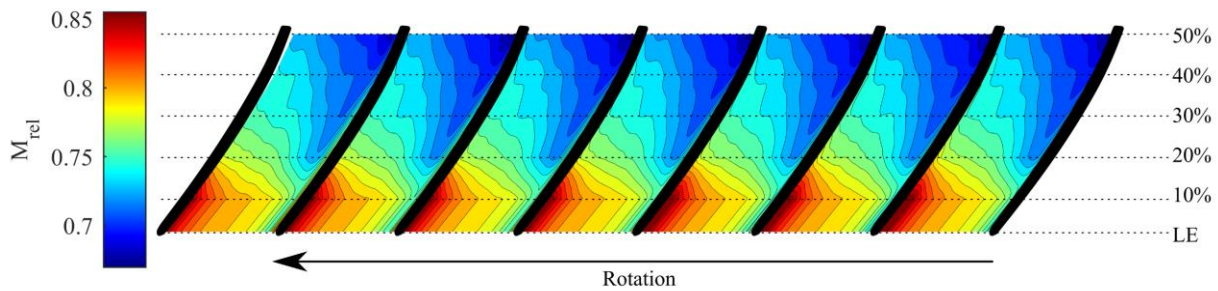


Figure 4.39 Contour of isentropic relative Mach number in the inducer at 80% of the corrected design speed

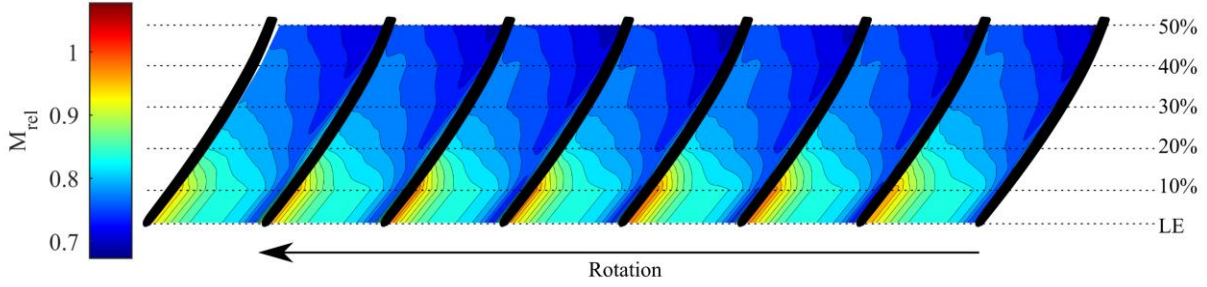


Figure 4.40 Contour of isentropic relative Mach number in the inducer at 85% of the corrected design speed

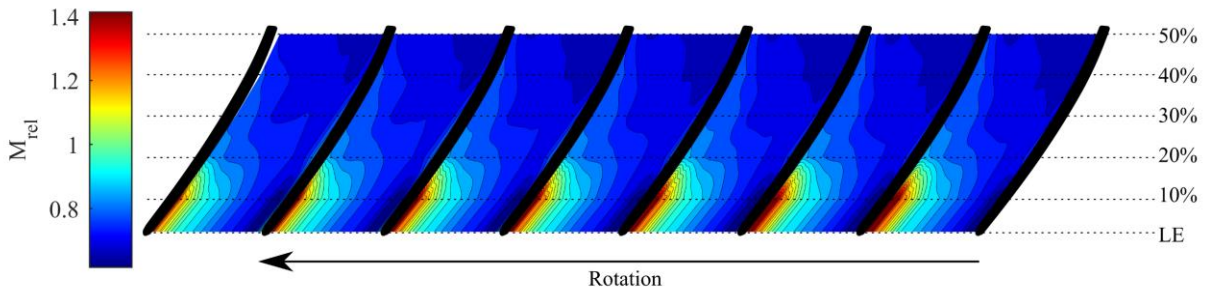


Figure 4.41 Contour of isentropic relative Mach number in the inducer at 90% of the corrected design speed

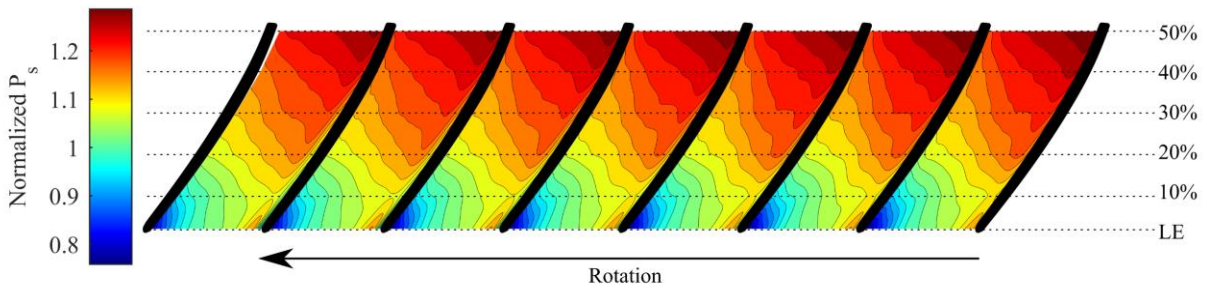


Figure 4.42 Contour of static pressure normalized by inlet total pressure in the inducer at a steady point recorded just prior to stall at 90% corrected speed

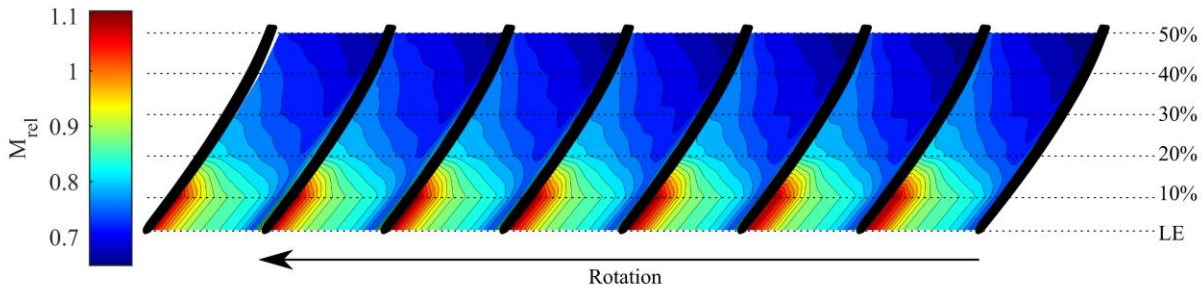


Figure 4.43 Contour of isentropic relative Mach number in the inducer at a steady point recorded just prior to stall at 90% corrected speed

Figure 4.44 depicts the isentropic relative Mach number along the impeller shroud for the mid-choke throttle setting at 80%, 85%, 90% and 95% corrected speed. The inducer is doing significantly more diffusion in the relative frame at higher corrected speeds, as would be expected. The Mach numbers shown in Figure 4.44 were calculated using static pressure taps and are, therefore, representative of the mean Mach number at a given location on the shroud, unlike that previously shown in the contours of relative Mach number.

Figure 4.45 depicts how the percentage of static pressure rise done by the inducer varies with speed. The static pressure rise in the inducer significantly increases from 75% to 85% of the compressor's design speed. This trend is virtually identical to the observed trend in impeller efficiency in the same speed range, which supports the idea that the inducer flow field is driving the observed change in efficiency. While the inducer accounts for a small percentage of the overall static pressure rise in the impeller, it is responsible for a significant amount of the loss. This is due to the fact that the static pressure rise in the knee and exducer of the impeller is largely the result of the centrifugal effect, which allows for essentially lossless pressure rise. Whereas the static pressure rise in the inducer is the result of diffusion, which is typically a more lossy process. The trend in static pressure rise can also be linked to the observed low-pressure region in the inducer, which indicates a region of high loss in the inducer that is observed to diminish as the speed is increased. Figure 4.46 demonstrates a similar trend for how the fraction of relative diffusion done in the inducer changes with speed, except rather than plateauing above 85% corrected speed, there is a dip in the amount of relative diffusion done by the inducer as the speed is increased further from 90% to 95% corrected speed. This may be the result of increased shock losses or an increase in the effects of interactions between the shock and secondary flow structures.

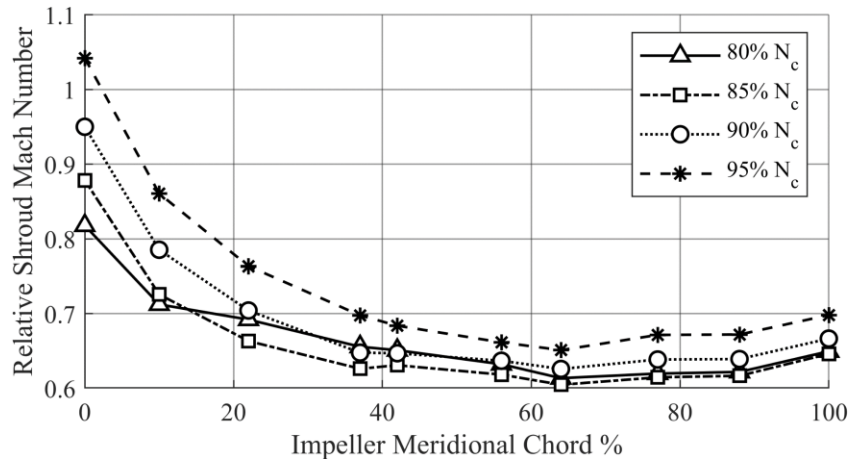


Figure 4.44 Relative shroud Mach number through the impeller at four different corrected speeds

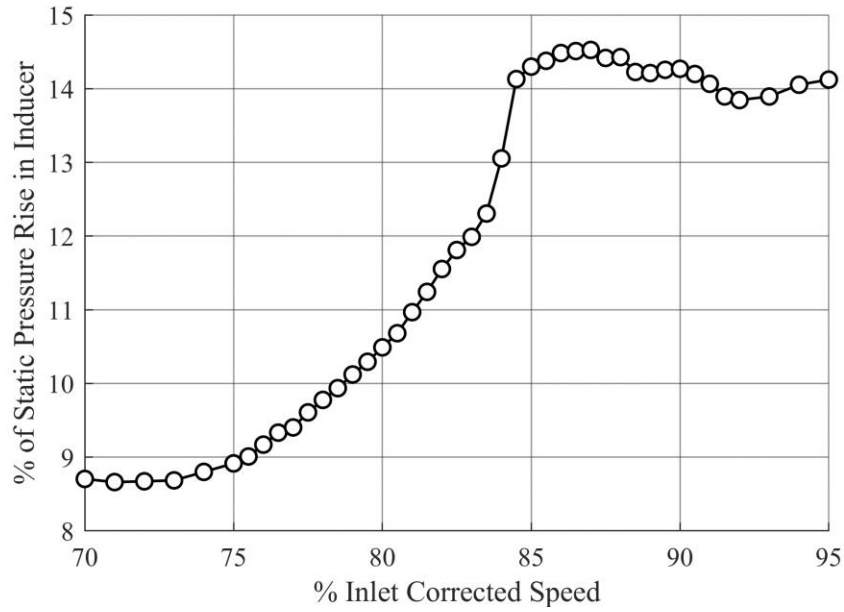


Figure 4.45 Fraction of static pressure rise in the impeller that is done by the inducer across a wide speed range

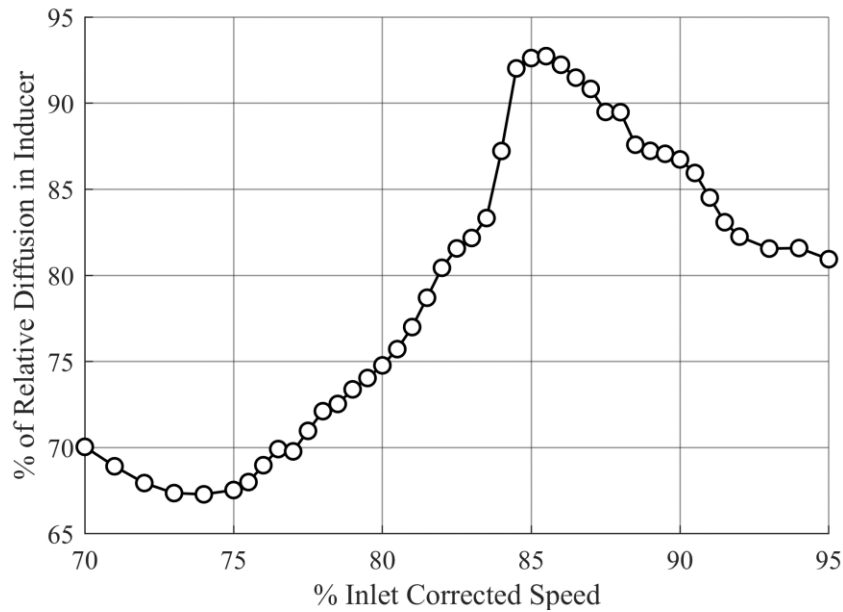


Figure 4.46 Fraction of relative diffusion in the inducer that is done by the inducer across a wide speed range

As mentioned previously, the deviation of the unsteady pressure signal from the ensemble average can be used to characterize the unsteadiness in the flow at a given operating condition. Figure 4.47 through 4.49 show contours of the rms variation in the Kulite signal from the ensemble average for 80%, 85%, 90%, and 95% corrected speeds each at the mid-choke throttle setting. At 80% of the compressors design speed, the leading edge of the pressure surface has the highest level of variation. As the speed is increased, this region shifts downstream such that at 90% corrected speed, the peak unsteadiness in the inducer occurs at approximately 20% chord. This supports the hypothesis that the formation of the inducer shock serves to shield the regions upstream of the shock from flow unsteadiness propagating upstream through the impeller passage. Also, the overall magnitude of the unsteadiness decreases as the speed is increased. The 95% speed case shown in Figure 4.50 shows much lower unsteadiness concentrated downstream of 20% inducer chord. There is a small region of higher unsteadiness at 10% chord on the main blade suction surface, which could be attributable to the interaction between the shock and the suction surface boundary layer, which will be discussed in more detail using the results of numerical simulations

in the next chapter. The magnitude and extent of this region of unsteadiness is, however, much lower than that observed in the lower speed cases.

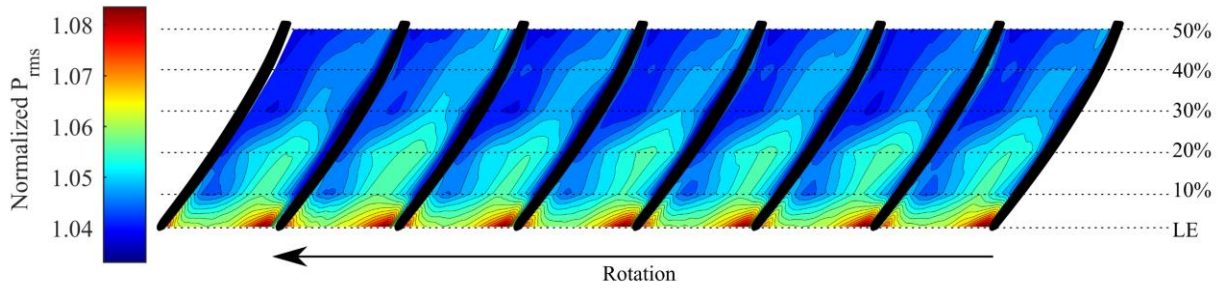


Figure 4.47 Contour of rms pressure variation in the inducer at 80% corrected speed for the mid-choke throttle setting

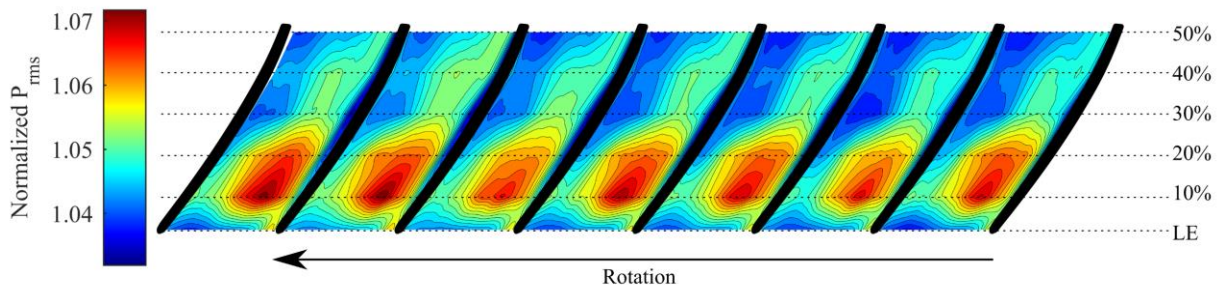


Figure 4.48 Contour of rms pressure variation in the inducer at 85% corrected speed for the mid-choke throttle setting

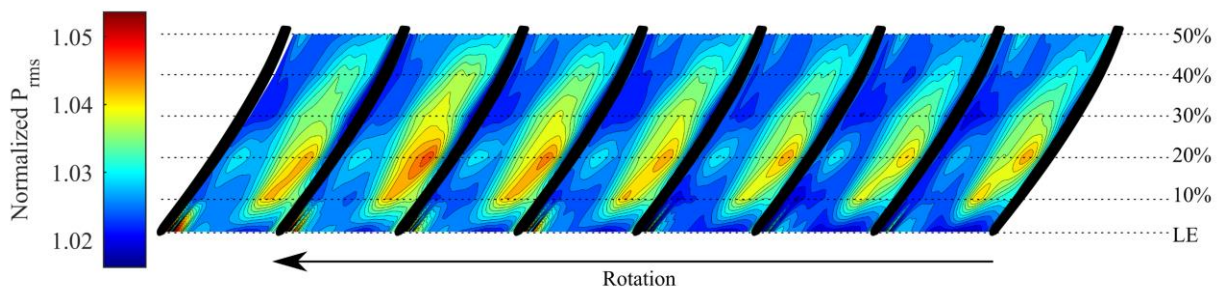


Figure 4.49 Contour of rms pressure variation in the inducer at 90% corrected speed for the mid-choke throttle setting

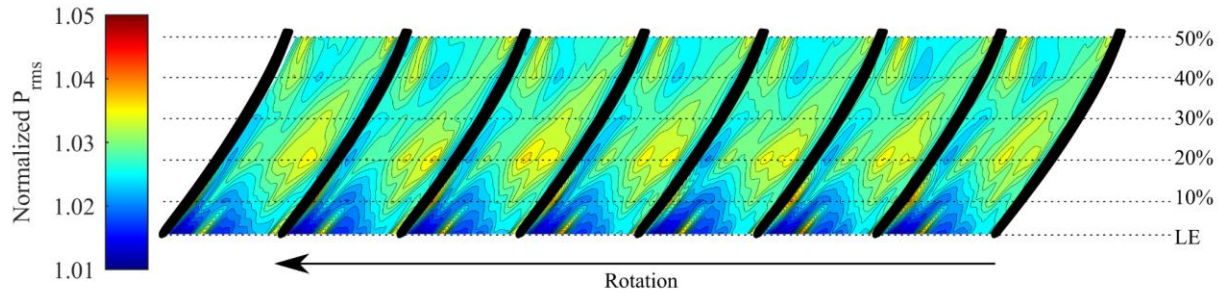


Figure 4.50 Contour of rms pressure variation in the inducer at 95% corrected speed for the mid-choke throttle setting

4.2.7 Summary of Experimental Results

Using transient data, a significant decrease in the unsteadiness in the inducer shroud pressure field occurs near the subsonic-to-transonic transition speed during speed transients from 40% to 100% of the corrected design speed. Further analysis of the frequency content revealed that this decrease in unsteadiness corresponded only to the sub blade pass frequency components of the signal. The transition speed varies depending on whether the data are collected during an acceleration or deceleration sweep or for a steady point. This variation is likely the result of heat transfer locally adjusting the Mach number in the inducer inlet, and the relative shifts in transition speed match what was expected based on a simple Rayleigh flow model, which provided further support to the theory that the step change in unsteadiness may be partially attributable to the formation of the shock in the inducer. Further analysis of the steady data showed that the decrease in unsteadiness was most significant in the inducer upstream of the shock whereas the change in unsteadiness further downstream in the impeller and diffuser was less significant. The stability of various components of the compressor were analyzed using the slopes of their static pressure rise coefficients, as was shown in [31], [32]. This analysis indicated that the inducer was the primary driver of instability at the transition speed, and the stability of the inducer improved dramatically as the speed was increased.

In addition to the changes observed in the unsteady pressure signals, there was also a significant increase in the impeller isentropic efficiency from 75% to 90% N_c . Temperature measurements of the flow just upstream of the impeller leading edge indicate significant recirculation and, therefore, loss that decreases in severity as the speed is increased above 80% N_c , which roughly corresponds to the speed at which the blade passing frequency becomes dominant

in the unsteady pressure signals. The change in efficiency was further linked to the inducer by analysis of the fraction of impeller static pressure rise and relative diffusion that is done by the inducer. These results showed an almost identical trend as that in impeller efficiency, with the performance of the inducer increasing significantly from 75% to 90% speed. Observations from static pressure contours of the inducer shroud showed a region of low static pressure at 80% N_c and 85% N_c which then decreased in both magnitude and extent when the compressor reached 90% N_c . Contours of the rms pressure variation from the ensemble averaged pressure showed a downstream shift in the location of peak unsteadiness in the inducer as the compressor speed increased, as well as a significant decrease in amplitude. This supports the idea that the formation of the shock is isolating a portion of the inducer from the highly unsteady flow field downstream of the inducer, and because the inducer is critical in determining the stable operating range of the impeller, this isolation has a marked effect on the variance of the shroud Kulite signals and the stability of the machine. This effect was also present in a change in the sensitivity of both impeller total pressure ratio and impeller efficiency to tip clearance as the impeller transitioned to the transonic operating regime. It would be expected that the sensitivity to changes in tip clearance would increase monotonically with speed due to the increasing pressure gradient across the blade tip, however the experimental results showed a decrease in sensitivity above 85% N_c , which is also believed to be a result of the shock formation isolating the inducer from changes in the downstream flow field that result from changing the exducer tip clearance. In order to better understand the behavior of the flow field, steady numerical simulations were conducted at a range of wheel speeds around the transition speed. The results of these simulations are the topic of discussion for the next chapter.

5. NUMERICAL RESULTS

Limitations that exist in the experimental instrumentation due to the small size of the flowpath relative to that of pressure and temperature probes mean that numerical simulations can allow for a much more comprehensive view of the flow field than is possible using purely experimental data. In order to ensure parity when comparing experimental and numerical results, probes are placed in the computational domain in the same locations as they are physically located in the test article. The data from these experimental probes are then processed using the same procedures that are used to process the experimental data to ensure the results are not skewed by inconsistent data reduction techniques. Simulations were performed for the same speed increments between 80% and 90% N_c as were used experimentally, however not all of the simulations reached satisfactory numerical convergence. Only results from simulations that are considered to be fully converged will be presented in this chapter.

5.1 Comparison with Experimental Results

Before using the simulation results to draw conclusions about the behavior of the flow field, it is important to show that the results of the simulation are representative of the real compressor. This will be done by comparing the performance, in terms of total pressure ratio and efficiency, as well as more detailed measurements of static pressure along the impeller shroud. As the focus of this thesis is primarily on the performance of the impeller at off-design speeds, the performance comparison will focus solely on the impeller, and the diffuser performance will not be considered.

5.1.1 Impeller Performance

Figure 5.1 shows a comparison between the numerically and experimentally calculated total pressure ratio. To ensure a representative comparison, the impeller exit total pressure was calculated using the iterative procedure described in Chapter 3, for both the experimental and numerical results. The iterative calculation assumes adiabatic flow through the diffuser and deswirl, which is only true in the case of the numerical model.

The comparison shows that the results agree reasonably well, especially above 85% N_c , where the mean deviation is approximately 0.4 points compared with 1 point for the full speed

range. Both experimental and numerical results show an increase in slope at 85%, however the numerical results show a significant change in level that is not observed in the experimental results. From the experimental unsteady data, there was a decrease in unsteadiness above approximately 85% corrected speed. It is possible that the less stable flow field at lower speeds is resulting in an underprediction of the total pressure ratio through the impeller that is reduced once the speed is increased above 85% of the design speed. This would explain the improved agreement between the experimental and numerical results at higher speeds as well as the sudden shift in the numerically calculated impeller total pressure ratio.

A similar trend exists with impeller isentropic efficiency, as depicted in Figure 5.2. In this case, both the experimental and numerical efficiencies experience a sudden increase above approximately 85% speed. However, as with the total pressure ratio, the numerical results have a much larger shift. This is again likely the result of an underprediction of the impeller efficiency in the numerical simulation resulting from the steady solver being unable to fully capture the behavior of the highly unsteady flow field that exists in the impeller during operation in the subsonic regime. Above the transition speed, there is much better agreement between the numerical and experimental results. The uncertainty associated with the experimental measurement of efficiency is significantly higher than that of the total pressure ratio measurement. This is because efficiency is dependent on temperature, which has a much higher measurement uncertainty than pressure, and is compounded by the relatively low temperature rise of the impeller at these speeds. This, combined with the incalculable uncertainty propagation associated with the iterative method for calculating the impeller exit total pressure, results in a relatively high (>4%) uncertainty in impeller efficiency. However, this uncertainty is associated with the absolute value of the efficiency, not with relative changes in efficiency. It is, therefore, impossible to say whether the experimental or numerical values are closer to a “true” value, but it can be definitively stated that the relative increase in efficiency observed at 85.5% speed is exaggerated by the numerical results.

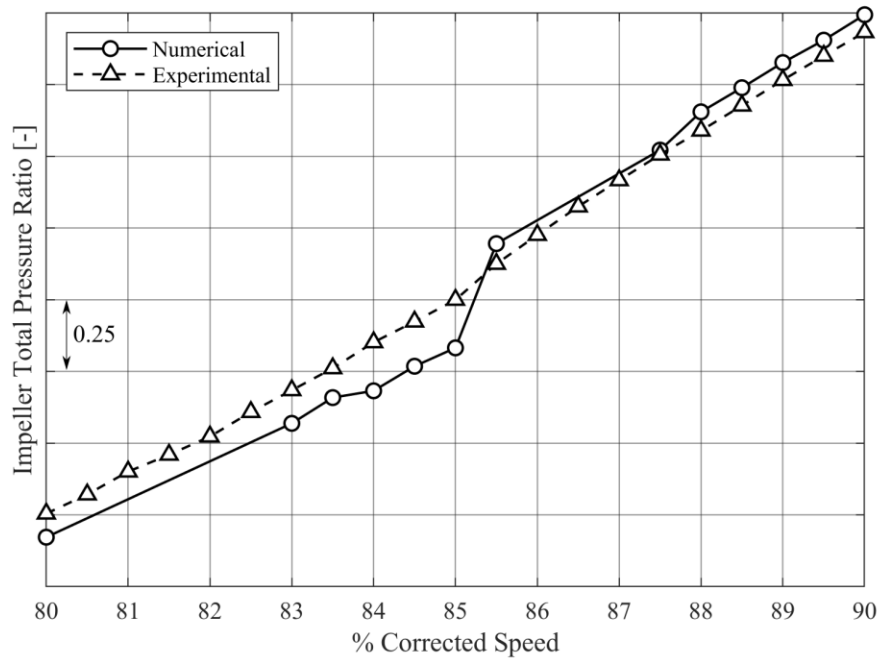


Figure 5.1 Numerical and experimental impeller total pressure ratio from 80% to 90% corrected speed

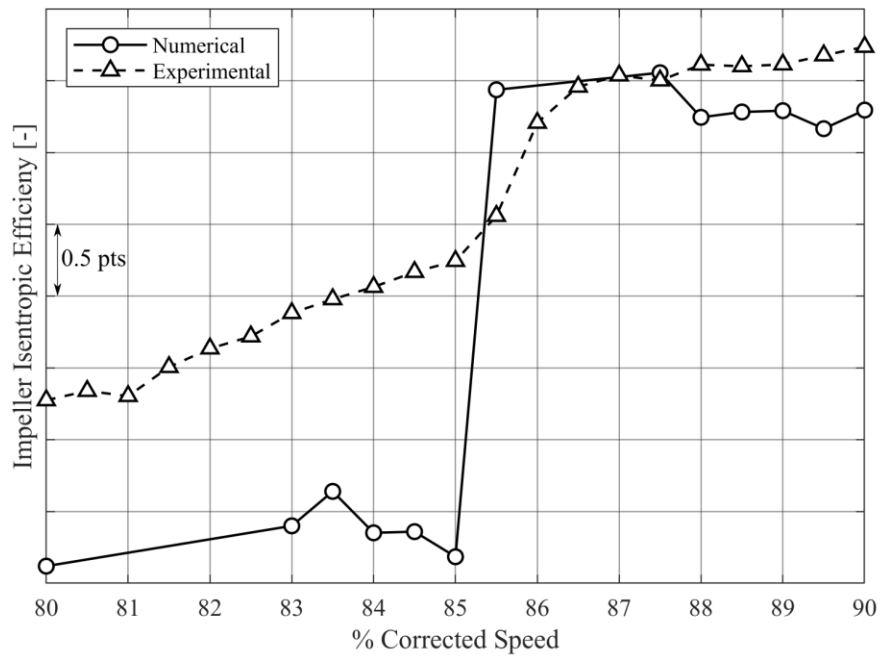


Figure 5.2 Numerical and experimental impeller isentropic efficiency from 80% to 90% corrected speed

5.1.2 Impeller Meridional Shroud Static Pressure

In addition to the overall performance of the impeller, it is necessary to compare the numerical and experimental results for detailed measurements. This ensures that the numerical solution isn't achieving a realistic answer in an unrealistic way e.g. more pressure rise being done in the inducer than is observed experimentally. This will be done by comparing the impeller shroud static pressure to ensure that the behavior of the numerical model is similar to that of the actual compressor. The static pressures in the numerical model are from the same meridional locations as the static pressure taps in the test article and are circumferentially averaged along a polyline in ANSYS CFD-Post. The results are shown in Figure 5.3, where again the model is less accurate for speeds at and below 85% N_c , but at higher speeds the numerical and experimental results agree very closely. The numerical results shown at 80% and 85% indicate less static pressure rise in the inducer than is observed experimentally. In combination with the observed discrepancy in impeller efficiency, it can be inferred that the numerical model is overpredicting the loss occurring in the inducer. While the model does not perfectly capture the impeller flow field, the trends are captured, as is indicated by both the computational and experimental results showing a significant increase in the static pressure rise in the inducer as speed increases. As was stated previously, the speed at which the numerical and experimental results fall into close agreement corresponds closely to the speed at which the unsteadiness in the Kulite signals was observed to decrease. It is therefore probable that the observed discrepancy in results at lower speeds is a direct result of the flow unsteadiness and the inability of a steady simulation to capture the unsteady effects of these flow features.

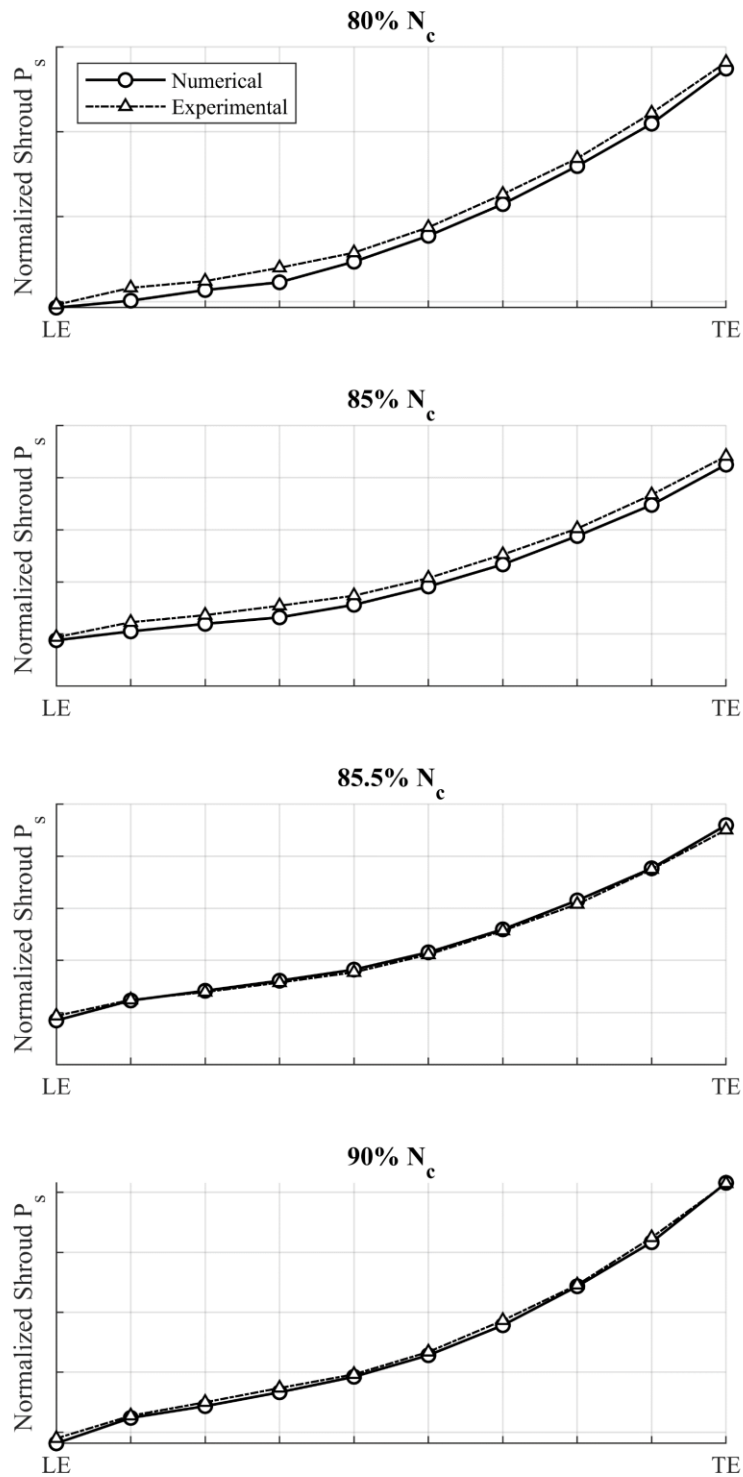


Figure 5.3 Comparison of experimental and numerical impeller shroud static pressures at four different corrected speeds

5.1.3 Inducer Shroud Static Pressure

To provide a more detailed comparison between the numerical and experimental shroud pressure fields, contour graphs of the numerical results were processed in the exact same manner as the experimental results. This was done by exporting data from the computational results along circular polylines placed at the locations of the impeller shroud Kulite sensors. Since only a single impeller passage was simulated, the numerical data were replicated to allow multiple blade passages to be shown in the pressure contour to make for an easier comparison with the experimental results.

The results for the 80% corrected speed op-line throttle condition are shown in Figure 5.4. The numerical results generally underpredict the static pressure in the inlet, as shown in the previous section. However, both contour graphs show a large low-pressure region extending from the leading edge into the impeller passage. The numerical results show the low-pressure region extending further downstream near the blade suction surface, reaching approximately 32% chord, whereas the experimental results show the low pressure region terminating at approximately 21% chord. This over-prediction of the high loss region in the inducer aligns with the previously observed underprediction in impeller efficiency. However, the general structure of the shroud pressure field is captured in the computational model. A comparison for the 85% speed case gives a similar result, as shown in Figure 5.5, where the numerical results show a larger low pressure region than is observed experimentally. However, as was observed in impeller total pressure ratio, impeller efficiency, and the impeller static pressures, the experimental and numerical results are much closer in agreement at speeds above 85%. Figure 5.6 shows a comparison of the shroud static pressures for 90% corrected speed. The results are now in very close agreement in both general structure as well as the actual values of the normalized static pressure. The primary discrepancy between the two is that the experimental results show a slightly lower pressure at the suction surface leading edge.

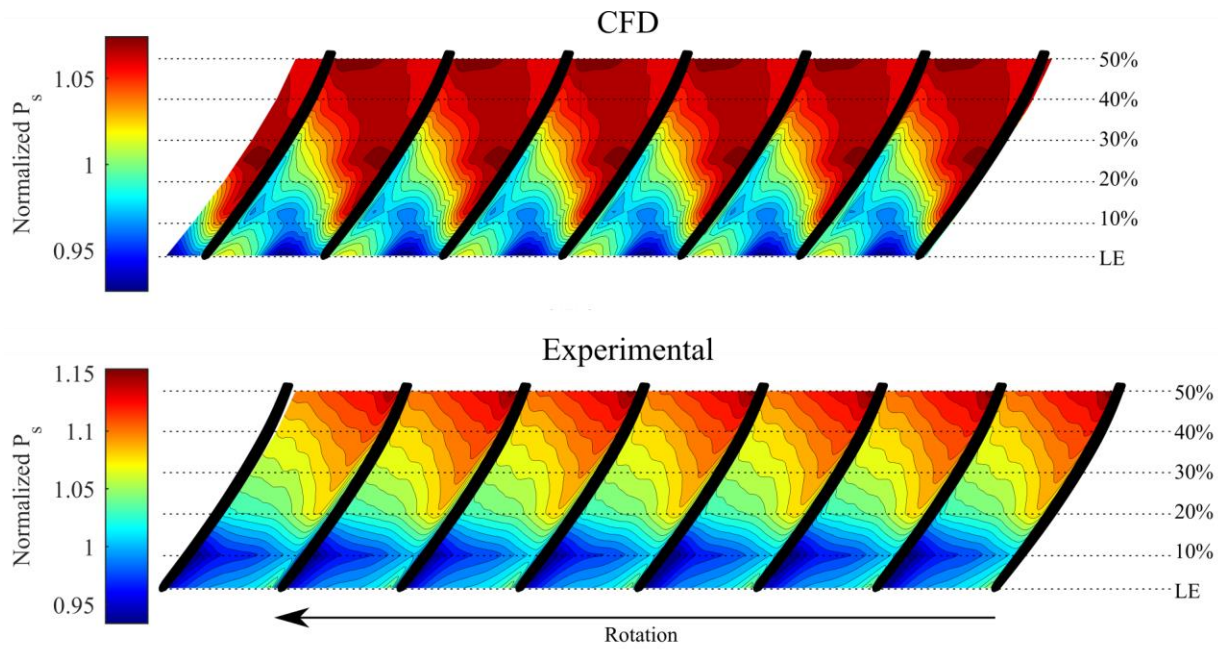


Figure 5.4 Comparison of shroud static pressure normalized by inlet total pressure for experimental and numerical results at the 80% corrected speed and op-line throttle setting

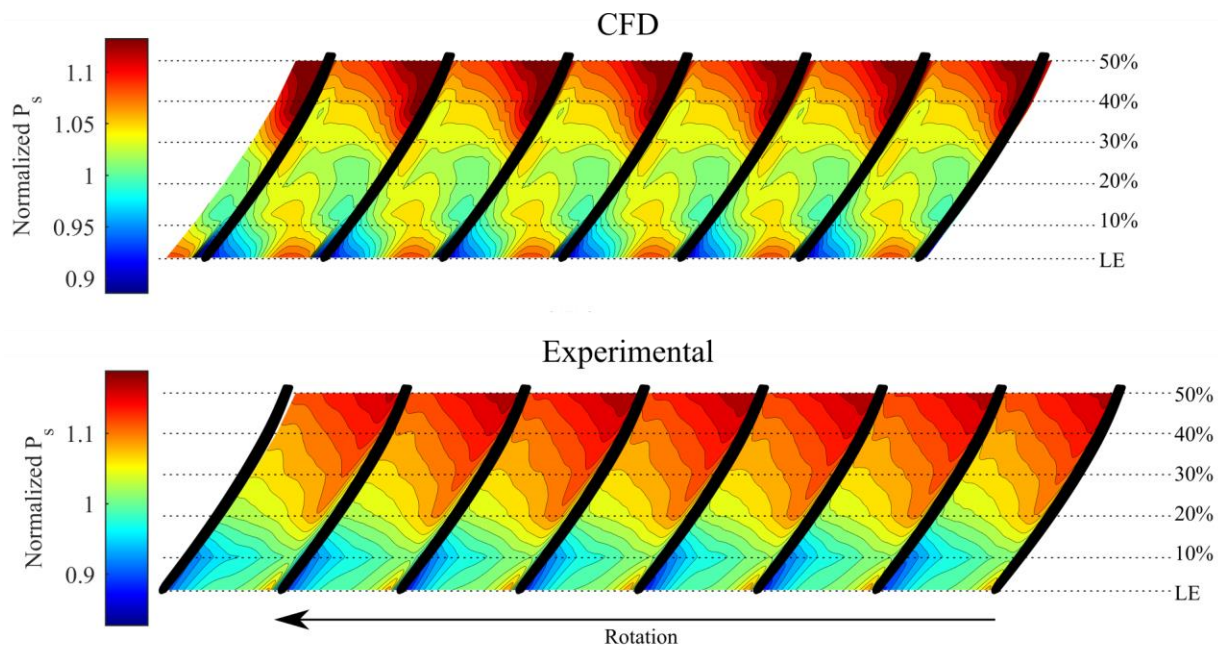


Figure 5.5 Comparison of shroud static pressure normalized by inlet total pressure for experimental and numerical results at the 85% corrected speed and op-line throttle setting

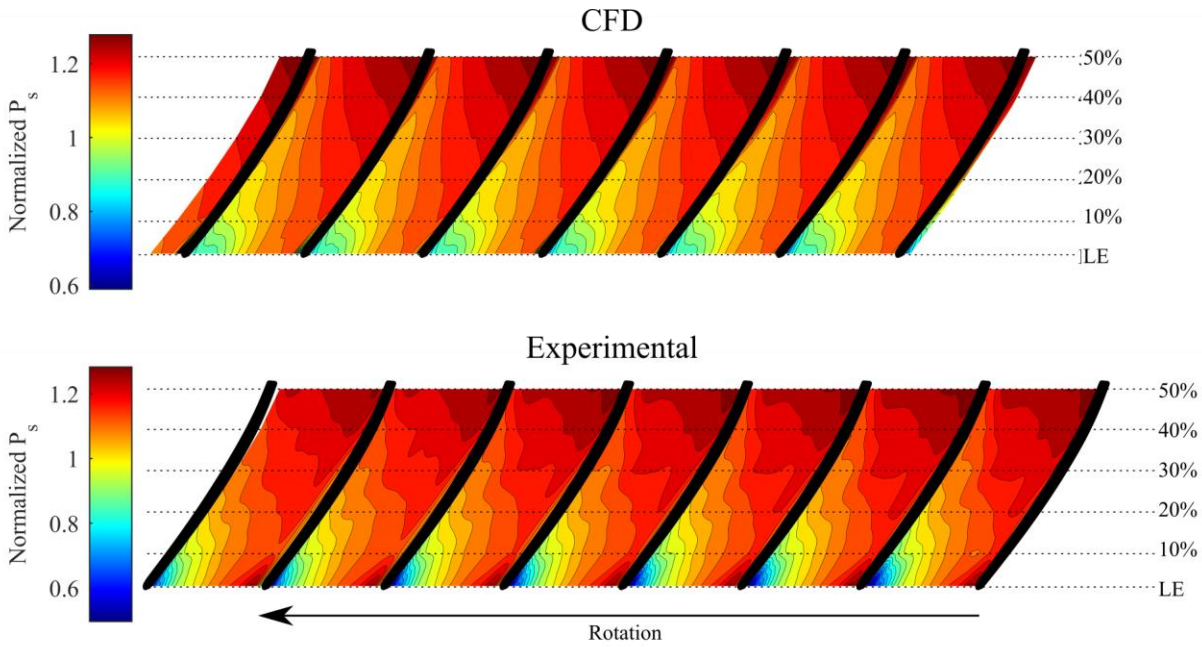


Figure 5.6 Comparison of shroud static pressure normalized by inlet total pressure for experimental and numerical results at the 90% corrected speed and op-line throttle setting

Based on the comparison of results in this section, the numerical model is considered to be sufficiently accurate to allow for a qualitative discussion about the impeller flow field to be drawn from the simulation results. Now that it has been established that the numerical model compares favorably with experimental data in regions where the data overlap, the model will be used in the remainder of the chapter for analyses that would be impossible with experimental data alone.

5.2 Impeller Flow Structure

The previous section focused on numerical results that could be measured experimentally to allow for validation of the model. However, the true value of a numerical simulation is the ability to extract extremely detailed information from the entire flow field that is virtually impossible to measure experimentally. This includes details of the tip leakage vortex behavior, the effective blockage in the impeller, and the structure, location, and interactions of the inducer shock. All of this information will allow for an improved understanding of the flow physics in the actual compressor and answer the primary question of what is driving the observed change in the performance of the impeller.

5.2.1 Tip Leakage Vortex

The inducer is believed to be the primary driver of the impeller performance in the 80% to 90% speed range and coupled with the observed pressure deficit in the inducer shroud for both experimental and numerical results, the behavior of the tip leakage vortex is of keen interest. Using Ansys CFD-post, a blade aligned surface was placed in the tip gap region at the impeller leading edge. This surface was then used as the seed point for streamlines, which allow for the visualization of the inducer tip leakage flow behavior. Figure 5.7 shows the tip leakage flow streamlines at 80% corrected speed, well within the subsonic operating regime of the impeller. The tip leakage flow is not rolling up into a coherent vortex structure, but it is instead forming a large region of recirculating, and therefore high loss, fluid near the shroud in the middle of the passage. This behavior agrees with the low-pressure region observed experimentally, indicating that the low-pressure region that is causing poor inducer performance at low speeds is the result of a large low momentum region near the shroud caused by the accumulation of the inducer tip leakage flow.

Increasing the speed to 85% results in the tip leakage structure shown in Figure 5.8. This higher speed case shows a reduction in the size of the low momentum region near the shroud, as well as a smaller pitchwise extent. This is partially attributable to the tip leakage flow trajectory being more aligned with the streamwise direction due to the higher mass flow rate and, therefore, axial velocity, of the compressor at higher speeds. However, even though the size of the recirculation region has decreased, the tip leakage flow has still not formed into a coherent vortex. Increasing the speed by just 0.5% of the design speed results in the tip leakage structure shown in Figure 5.9, where a coherent vortex has formed from the tip leakage flow as a result of the interaction with the main passage flow. It should also be noted that the tip leakage flow relative Mach number now exceeds unity near the leading edge, which was not true for the previous two cases. Due to the sudden formation of the tip leakage vortex after a relatively small increase in speed, it is difficult to conclude that the change is not the result of the formation or change in structure of the shock.

It is tempting to say that this phenomenon is purely a result of errors in the numerical model, since such a sudden change in the structure of the flow is not expected for a minor increase in wheel speed. However, this sudden change is also observed in the experimental results for both transient and steady state data. As in the experimental data, after the transition speed is crossed, the structure of the flow field remains essentially the same as speed is increased further. Figure

5.10 shows the tip leakage vortex at 90% corrected speed, and the general structure is very similar to that of the 85.5% speed case. The only significant difference is that the shock location has shifted downstream, as expected, and the vortex trajectory is slightly more aligned with the streamwise direction due to the increased axial velocity of the primary passage flow. Neither the 85.5% nor the 90% case show indications of vortex breakdown due to interaction with the inducer shock, which is not surprising due to the relatively weak shock at these speeds coupled with the low circulation of the vortex not being conducive to vortex breakdown per the understanding established by Thomer Et al. [15].

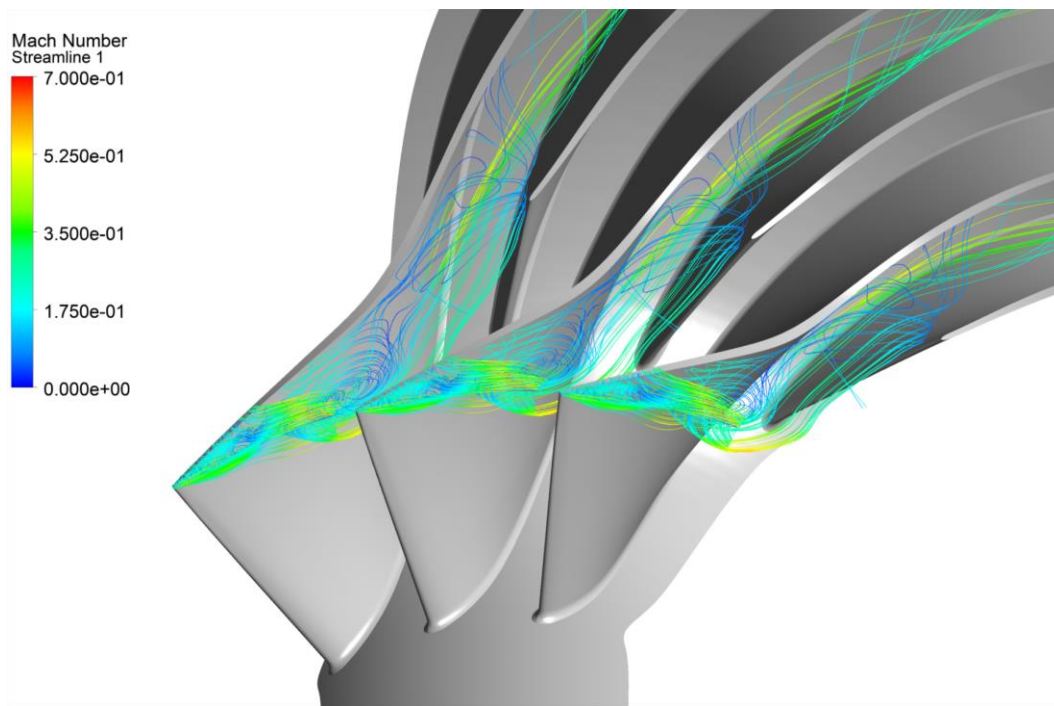


Figure 5.7 Inducer tip leakage flow structure at 80% corrected design speed, the streamlines are colored with relative Mach number to indicate the presence of a shock

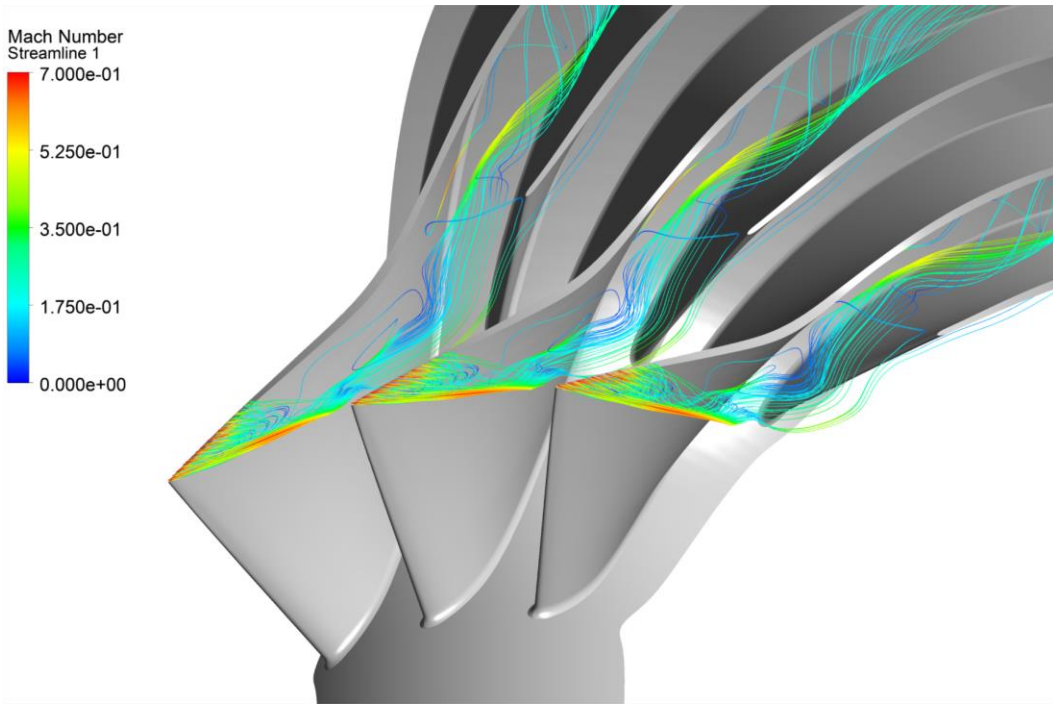


Figure 5.8 Inducer tip leakage flow structure at 85% corrected design speed, the streamlines are colored with relative Mach number to indicate the presence of a shock

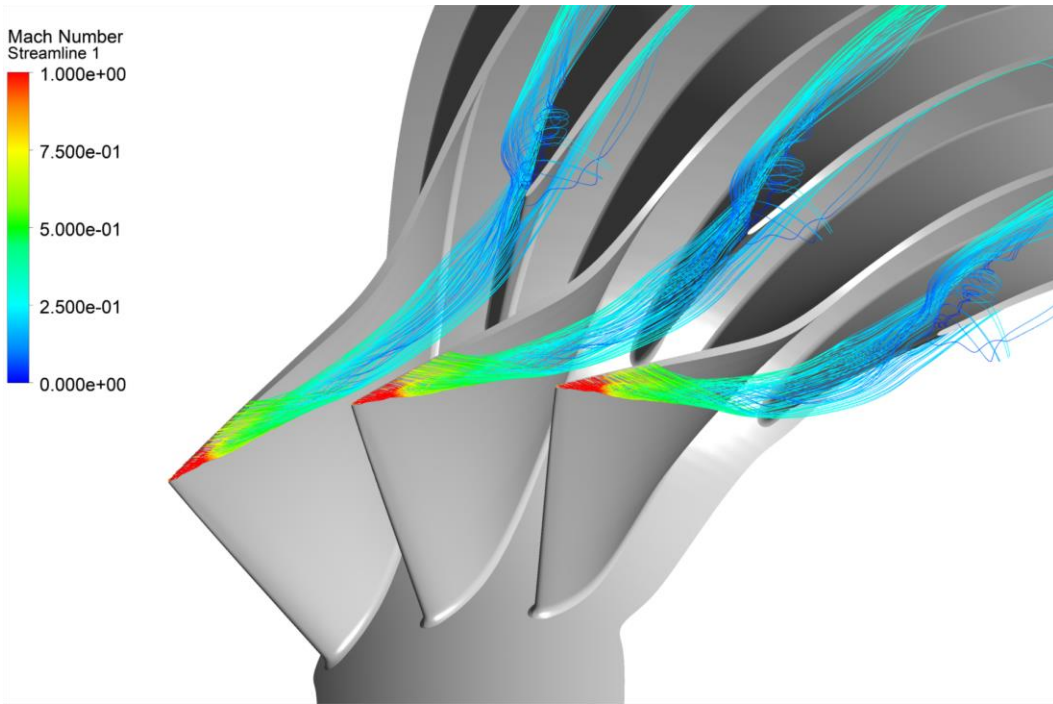


Figure 5.9 Inducer tip leakage flow structure at 85.5% corrected design speed, the streamlines are colored with relative Mach number to indicate the presence of a shock

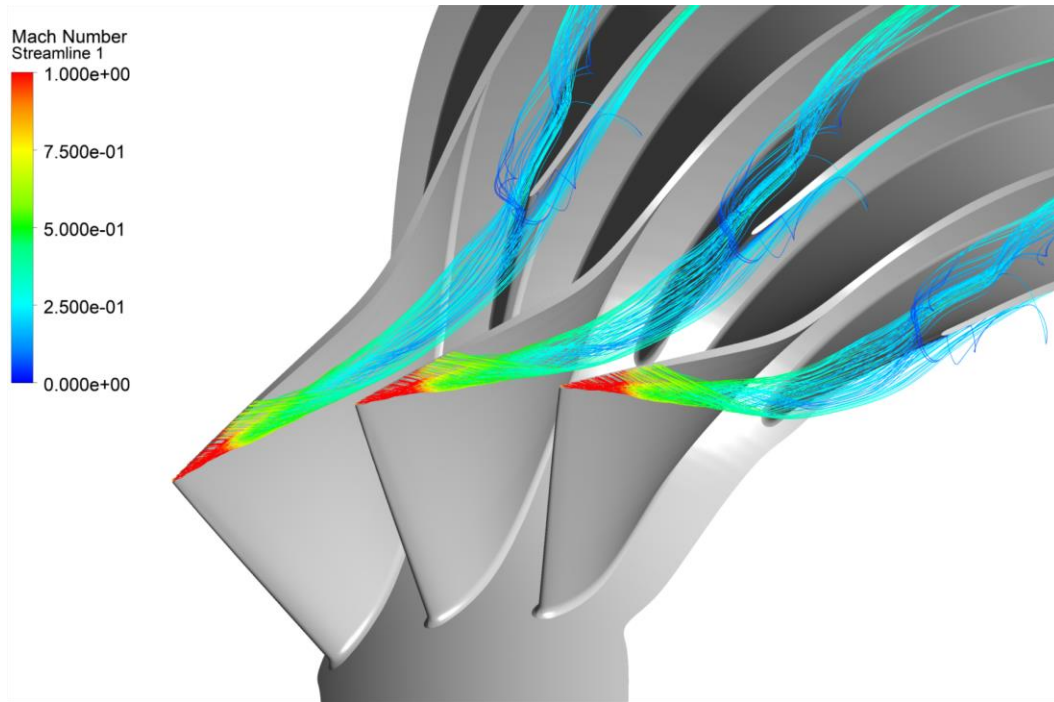


Figure 5.10 Inducer tip leakage flow structure at 90% corrected design speed, the streamlines are colored with relative Mach number to indicate the presence of a shock

5.2.2 Blockage

The size of the low momentum region near the impeller shroud may be quantified using equation (1.2). As the numerical results contain the velocity data for the entire flow domain, the blockage may be calculated at any location within the impeller. For the sake of comparison with experimental data, the blockage was calculated at 10 planes in the impeller domain, corresponding to the locations of the impeller shroud Kulites. These planes are shown in Figure 5.11.

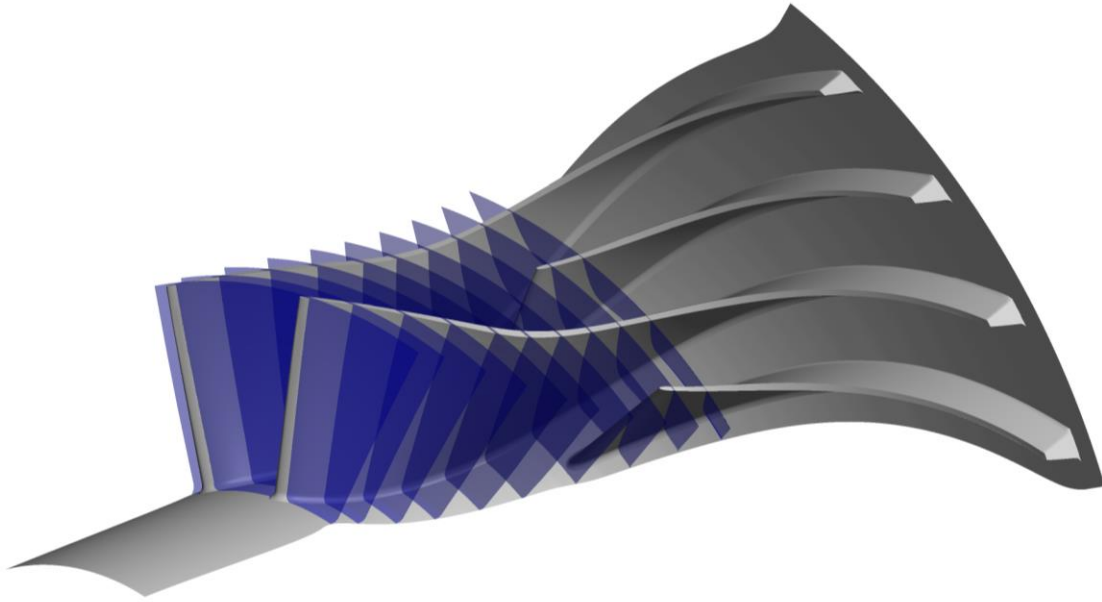


Figure 5.11 Meridional planes used to calculate blockage in the inducer

Yet again, the results show a significant change in the impeller flow field as the compressor transitions from subsonic to transonic operation. Figure 5.12 depicts the trend in blockage at the impeller leading edge for all of the simulated speeds. The blockage decreases suddenly at speeds above 85% of the design speed. Also, there is a gradual decrease prior to the sudden change, indicating that the blockage may also be diminishing both as a result of the increasing rate of mass flow through the machine and the formation of the shock in the inducer. The trend is consistent for the blockage throughout the inducer, as depicted in Figure 5.13, where it is observed that the blockage decreases with increasing speed, up to 85.5% corrected speed, at which point the blockage remains virtually unchanged to 90% corrected speed. The magnitude of the blockage at speeds less than 85.5% is likely inflated, as the steady simulation seems to exaggerate the extent and effect of the region of recirculating flow. To ascertain the nature of the low momentum region, i.e. is it a viscous or inviscid effect (or perhaps some combination of the two), the 80% corrected speed case was used for further analysis.

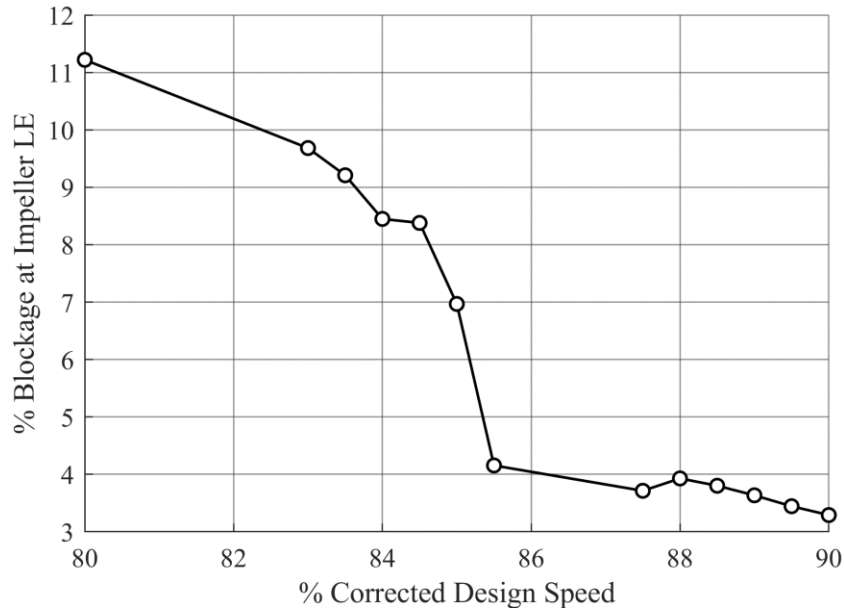


Figure 5.12 Numerically calculated blockage at the impeller leading edge for a range a corrected speeds

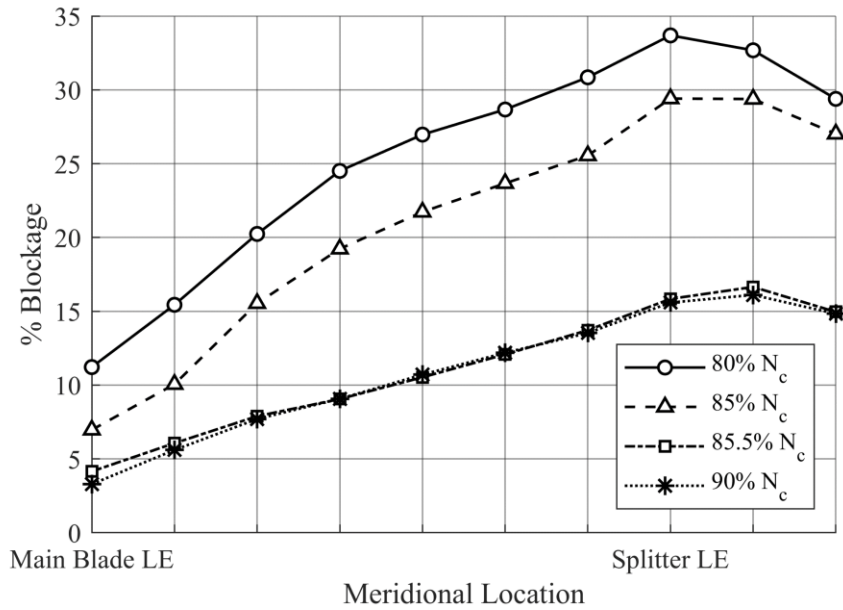


Figure 5.13 Numerically calculated blockage for locations throughout the inducer at 80%, 85%, 85.5%, and 90% corrected speeds

A contour graph of the circumferentially averaged meridional velocity for the 80% corrected speed simulation is given in Figure 5.14, where the low momentum region extends upstream of the impeller leading edge and is present throughout the inducer. The size of the low momentum region is diminished in the radial portion of the impeller as a result of the low momentum fluid being accelerated by the centrifugal force as the flow is turned to radial. In addition to giving a more complete view of the flow field than is possible with experimental data, a numerical model also allows a researcher to vary parameters that would not be possible to vary in an actual experiment. In this case, in order to ascertain whether the blockage is related to the boundary layer on the inlet shroud, the simulation was run with a free slip condition on the shroud surface upstream of the impeller leading edge. This modification to the simulation will prevent the development of a boundary layer on the shroud surface, and the effect on the inducer blockage can then be observed. The free slip condition did not extend to the impeller leading edge, and a no-slip condition existed approximately one span upstream of the leading edge. Figure 5.15 and Figure 5.16 show the effect that imparting a free-slip condition on the inlet shroud had on the calculated blockage. The low momentum region does not extend as far upstream for the free-slip case, and there is a moderate decrease in blockage near the leading edge, however the results are largely the same as the no-slip case. It is, therefore, concluded that the boundary layer on the inlet shroud shrinking with increasing speed provides an explanation for the decrease in blockage from 80% to 85% speed but cannot explain the sudden drop in blockage that follows.

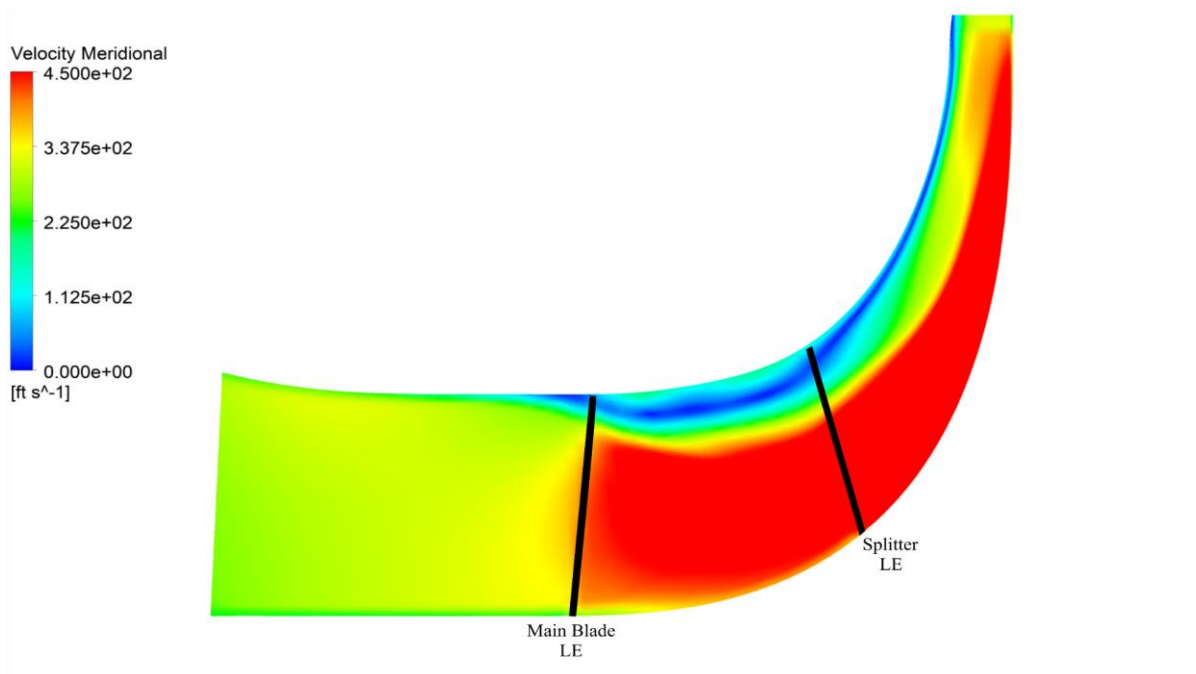


Figure 5.14 Contour of the circumferentially averaged meridional velocity in the impeller at 80% corrected speed (the image is skewed to protect the proprietary nature of the impeller geometry)

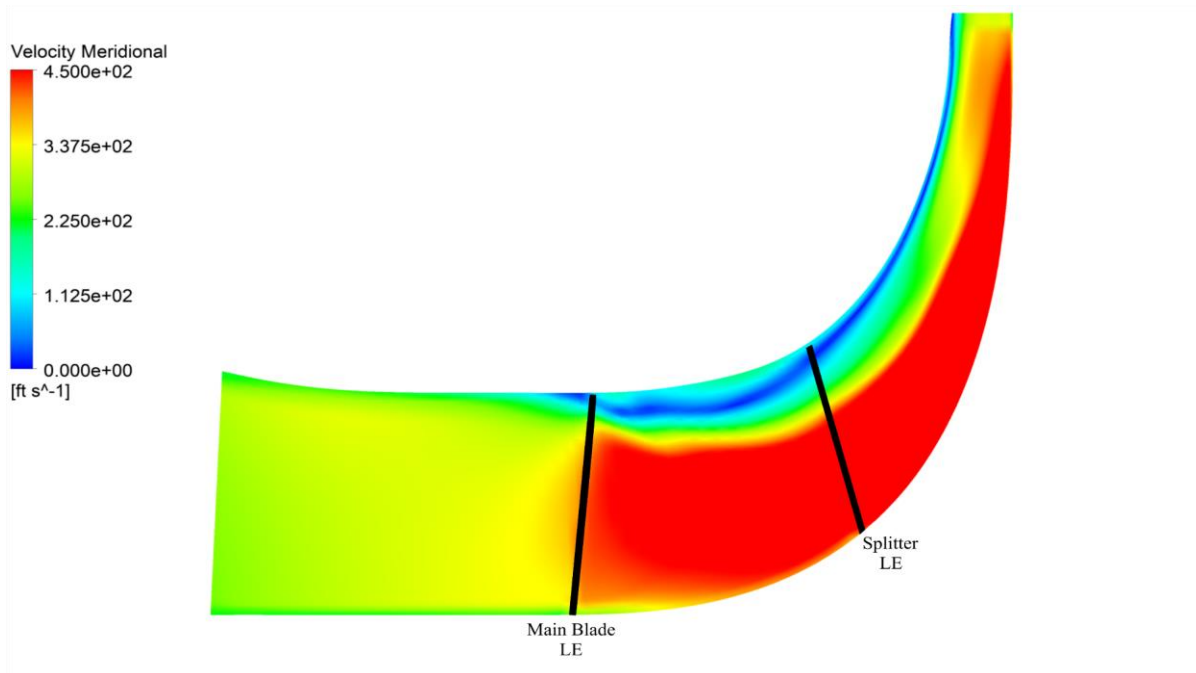


Figure 5.15 Contour of the circumferentially averaged meridional velocity in the impeller at 80% corrected speed with a free slip boundary condition on the inlet shroud (the image is skewed to protect the proprietary nature of the impeller geometry)

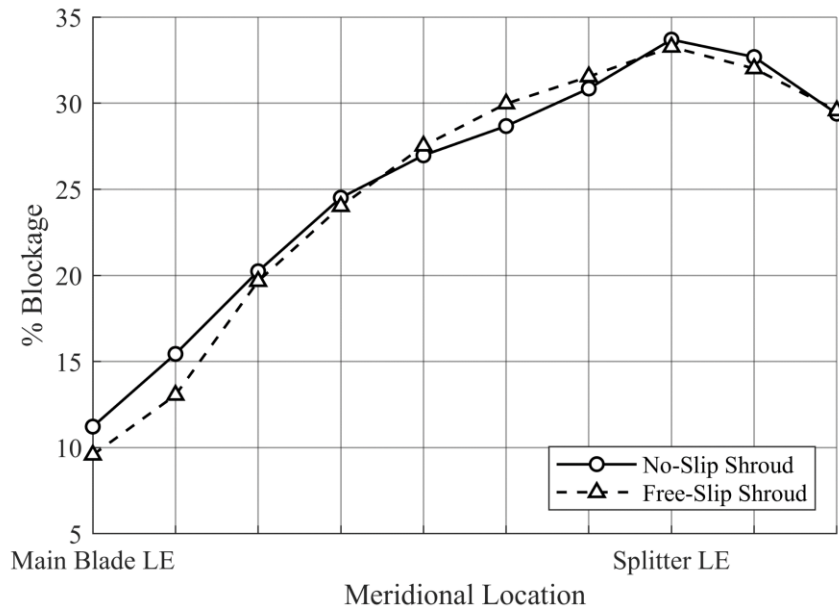


Figure 5.16 Comparison of blockage between 80% corrected speed cases with free-slip and no-slip boundaries on the inlet shroud surface

Figure 5.17 shows the meridional contour for the 85.5% speed case, after the sudden decrease in blockage, and the low momentum region near the shroud in the impeller passage no longer extends upstream of the impeller leading edge. This is likely a direct result of the formation of the passage shock near the leading edge of the inducer. Upon the expansion of the shock to the shroud, the incoming low momentum flow near the shroud boundary layer is no longer able to detect the low momentum flow near the shroud in the impeller passage and as a result the flow does not begin to decelerate until it reaches the shock near the leading edge of the impeller. This has the effect of preventing the blockage from forming upstream of the leading edge, and since the low momentum region no longer forms upstream of the impeller, it cannot interact with the tip leakage vortex, thereby explaining why the tip leakage vortex was only observed to form at speeds at and above 85.5% of the design speed. This would also, at least in part, explain the observed decrease in unsteadiness in the experimental results, as the recirculation region caused by the interaction of the low momentum flow with the tip leakage flow is in effect destroyed by the presence of the shock at the impeller leading edge.

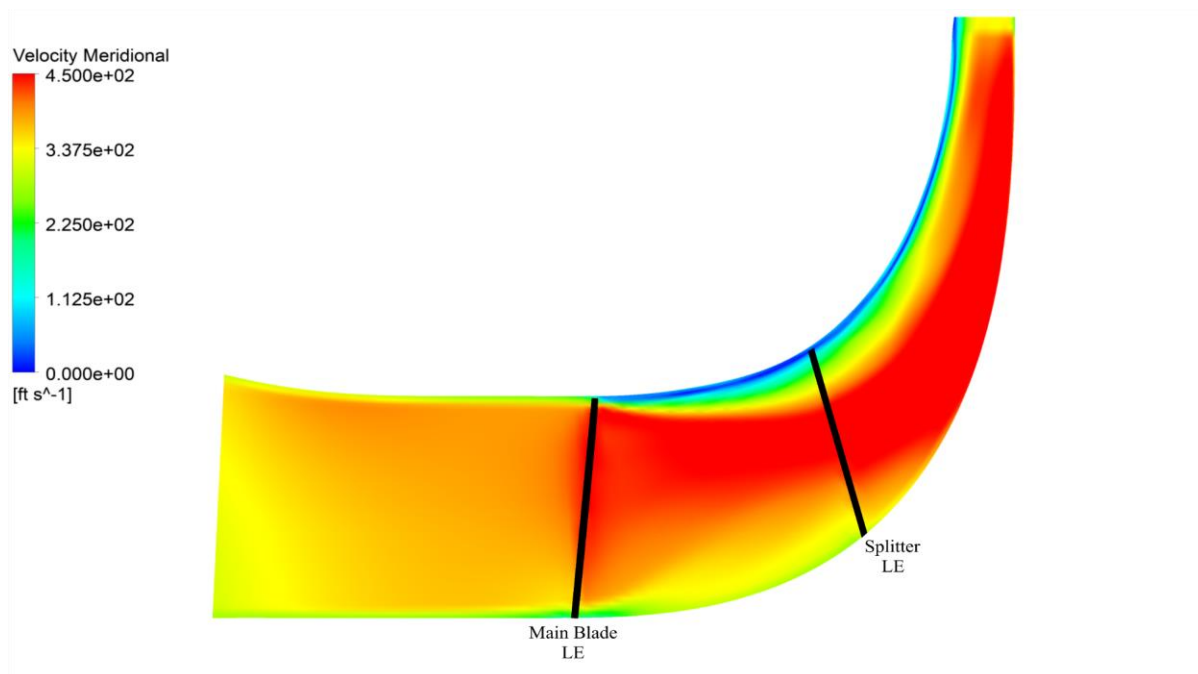


Figure 5.17 Contour of the circumferentially averaged meridional velocity in the impeller at 85.5% corrected speed (the image is skewed to protect the proprietary nature of the impeller geometry)

5.2.3 Shock Location

To conclusively determine whether the observed changes in impeller performance are caused by the transition to a transonic flow regime, the structure of the inducer shock will be investigated for speeds below and above the transition. As was previously discussed, supersonic inlet flow is unable to adjust to downstream flow features before decelerating to subsonic speeds after passing through the shock. Using the numerical results, it is possible to visualize the location of the shock near the inducer leading edge and determine if there is a significant change in the shock structure that is driving the improvement in performance. Figure 5.18 depicts the shock structure in the inducer at 85% corrected speed, where the green isosurface indicates the region where the Mach number exceeds unity, the trailing edge of which corresponds to the location of the shock. At 80% speed, the transonic region does not intersect with the 95% span plane, indicating that the shock does not fully extend to the shroud. The flow is supersonic from approximately 25% to 92% span, but the flow is subsonic in the tip region. And, it is this subsonic region near the tip that allows for the interaction between the inlet shroud boundary layer and the tip leakage vortex that results in the high-loss, low-momentum region observed both

experimentally and in the numerical results. Figure 5.19 demonstrates that by increasing the corrected speed from 85% to 85.5%, there is a sufficient increase in mass flow rate and wheel speed that the shock now fully extends to the shroud. This small increase in spanwise extent results in a significant change in the shock structure, as the incoming flow is now purely supersonic near the shroud. The flow no longer reacts to the downstream blockage, and as a result, the low momentum region in the impeller passage is largely destroyed. This causes a further increase in the Mach number and thus also increases the extent of the shock. This agrees with observations made during data collection where the compressor stability could be improved by increasing the mass flow rate through the impeller (by decreasing tip clearance or increasing bleed flow rates while speed was held constant). These small increases in mass flow were sufficient to allow the flow to become supersonic near the shroud, thus destroying the region of recirculating flow. As expected, increasing the compressor speed leads to the shock shifting further into the impeller passage and extending further in the direction normal to the blade surface. The shock structure for the 90% speed case is shown in Figure 5.20, where the shock now extends past the leading edge of the adjacent main blade indicating that in the region near the shroud, the flow is supersonic across the entire passage.

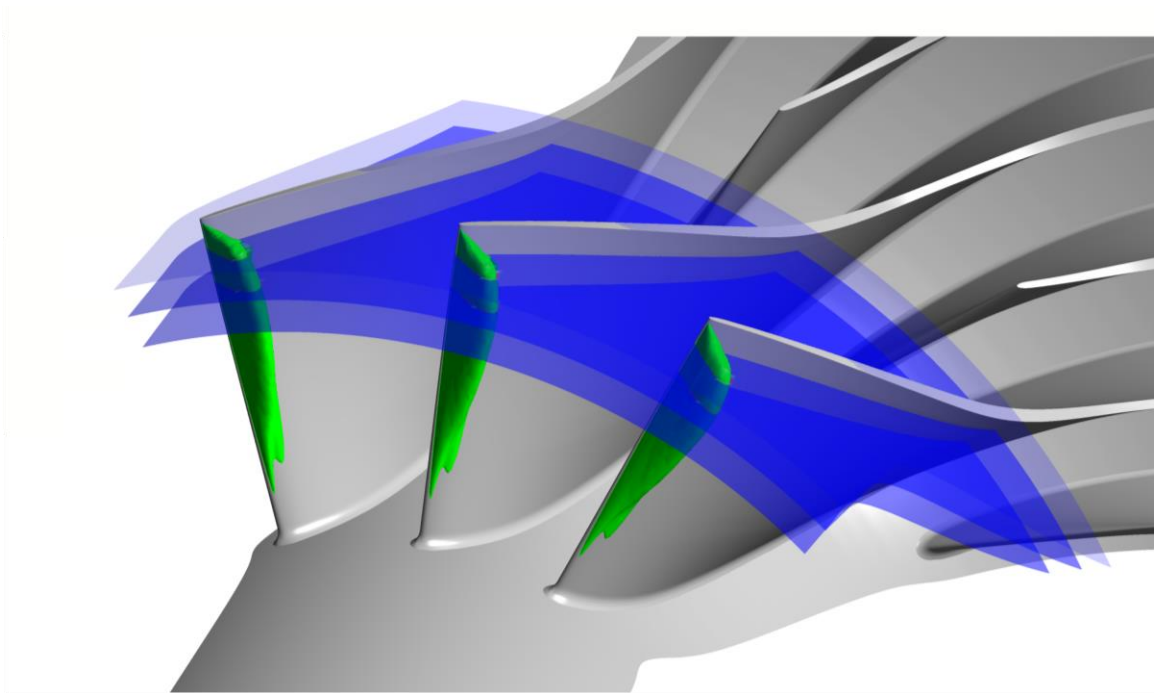


Figure 5.18 Shock structure in the inducer for the op-line condition at 85% corrected speed. Planes shown are at 80%, 90%, and 99% span, with the isosurface indicating the region where the Mach number exceeds unity.

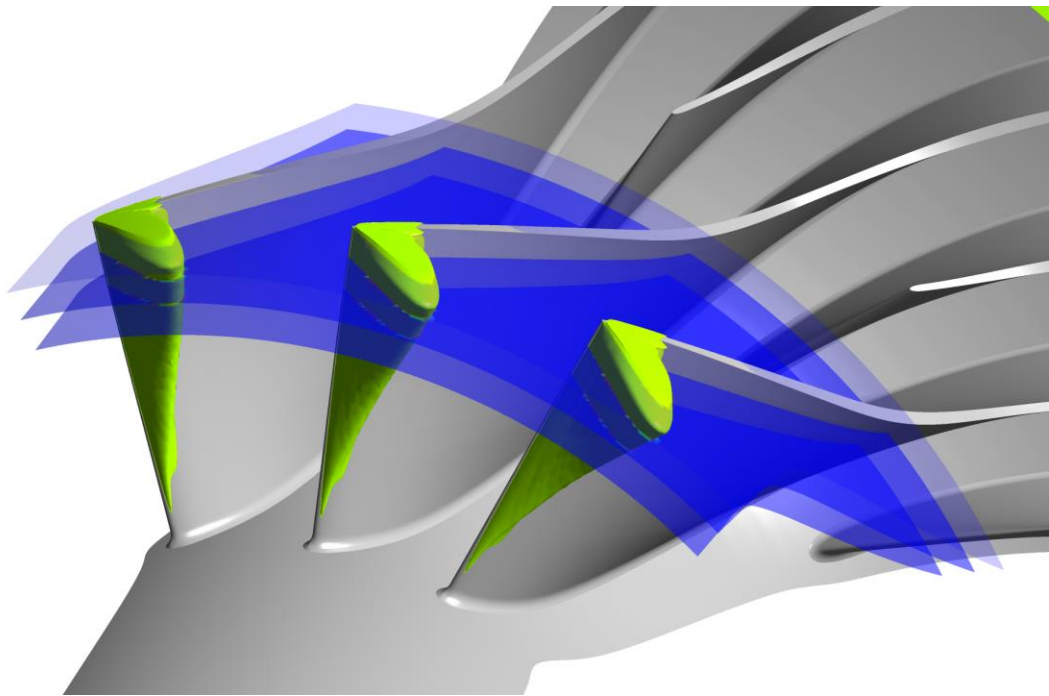


Figure 5.19 Shock structure in the inducer for the op-line condition at 85.5% corrected speed with isosurface showing the region where the Mach number exceeds unity

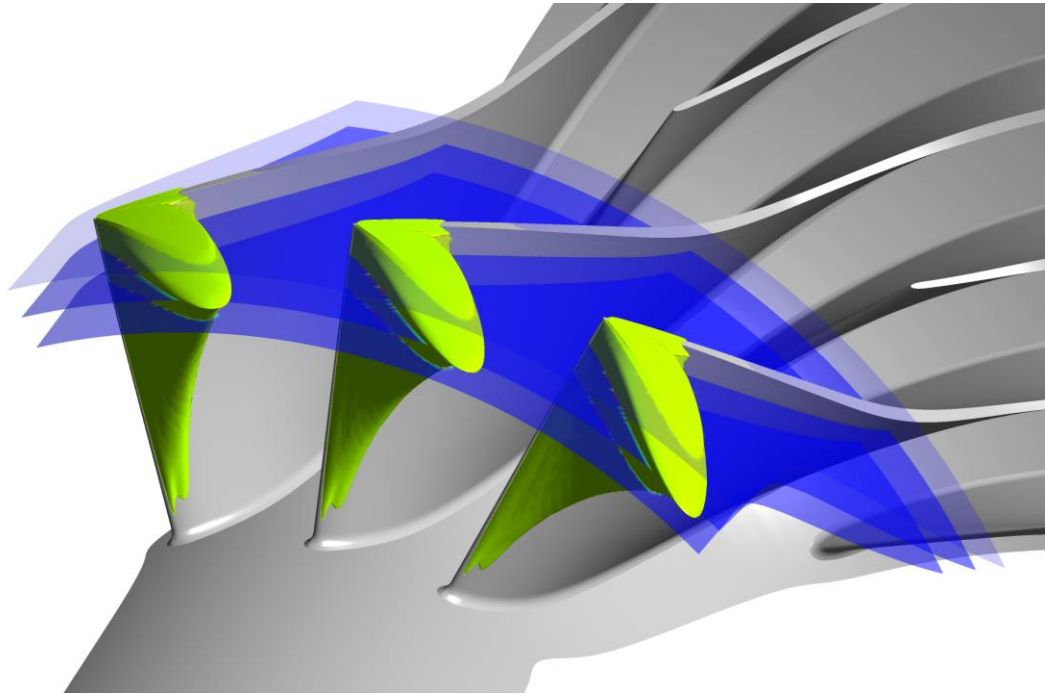


Figure 5.20 Shock structure in the inducer for the op-line condition at 90% corrected speed with isosurface showing the region where the Mach number exceeds unity

5.2.4 Shock Interactions

While the shock is observed to have beneficial effects at the transition speed as detailed previously, it is widely reported in the literature that the interactions between the shock and secondary flow structures, such as the tip leakage vortex and suction surface boundary layer, can have a severely detrimental impact on the performance and stability of the compressor. Using a numerical analysis allows for these interactions to be observed and to determine whether they have a significant impact on the compressor's behavior.

As discussed in Chapter 1, normalized helicity as defined by equation (1.3), can be used to determine if the tip leakage vortex breaks down as well as the location that breakdown occurs. The underlying principle is that for points near the vortex core, the value of normalized helicity will be near positive or negative one. Breakdown is defined as the point where the sign of normalized helicity is reversed, which indicates a reversal in the direction of the vortex's circulation. Figure 5.21 depicts the tip leakage flow streamlines colored by normalized helicity, where the breakdown of the vortex does occur. However, it is well downstream of the inducer shock, indicating that it is

not the direct result of the interaction with the shock. As breakdown is more likely to occur for stronger shocks interacting with vortices that have greater circulation, the same data are shown for a 100% speed case at a high throttle condition, for which breakdown is more likely to occur. The results, however, are largely the same as the 90% speed case, with breakdown occurring at effectively the same location downstream of the shock. Therefore, it is concluded that, for this compressor, the interaction between the tip leakage vortices and inducer passage shocks do not play a dominant role in the compressor performance.

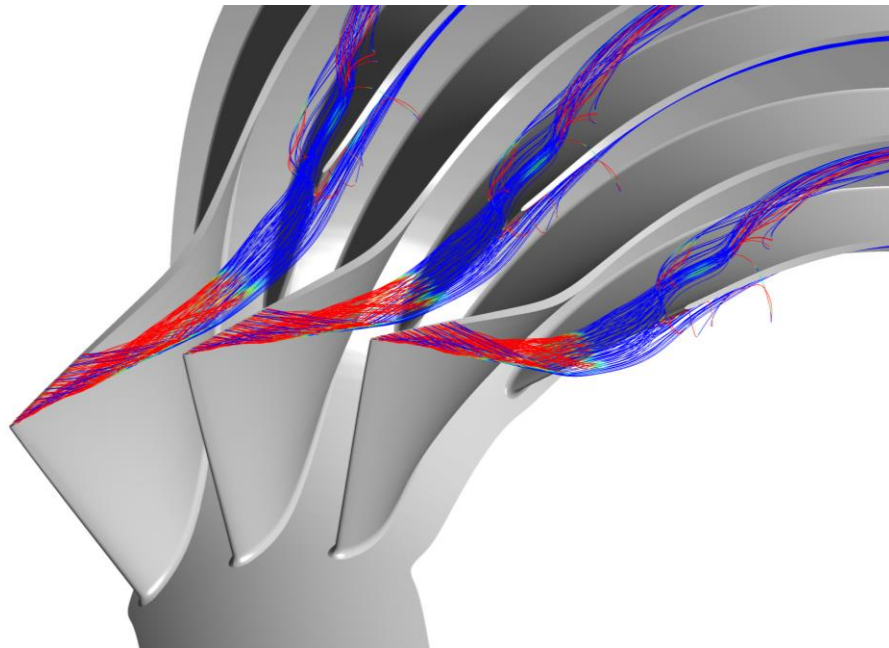


Figure 5.21 Tip leakage vortex streamlines for the op-line condition at 90% corrected speed, colored by normalized helicity, where red and blue indicate positive and negative values respectively

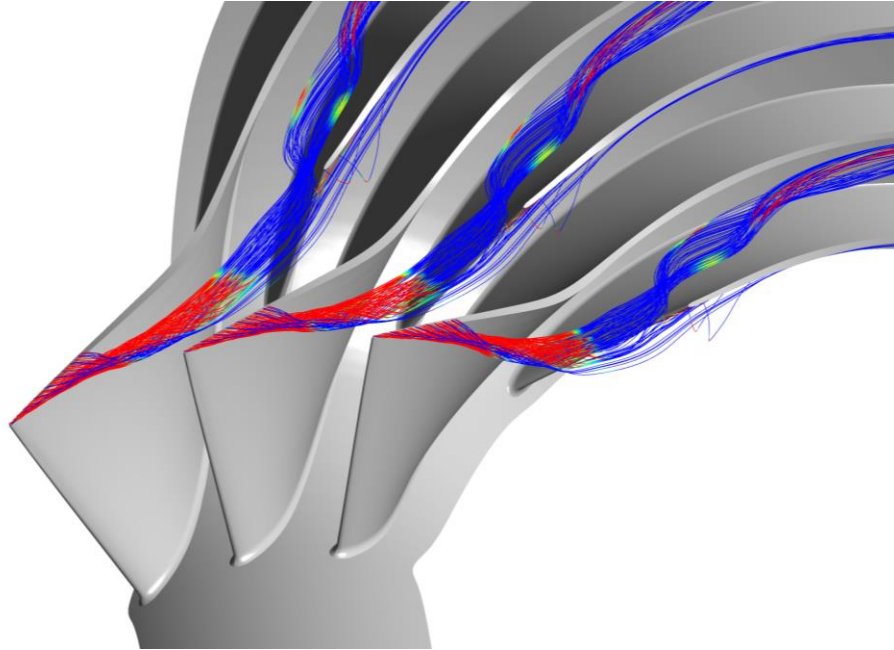


Figure 5.22 Tip leakage vortex streamlines for the op-line condition at design speed, colored by normalized helicity, where red and blue indicate positive and negative values respectively

It has also been reported in the literature that interactions between the passage shock and the suction surface boundary layer can lead to premature separation of the boundary layer causing the compressor to become unstable. Using the method of limiting streamlines to visualize the flow behavior near the blade surface, it is possible to determine if separation occurs, and if so, the extent of the separation and whether it was the result of interaction with the shock. As it is not possible to plot true streamlines on a surface due to the no-slip boundary condition, limiting streamlines are used to give an approximation of the flow behavior in the limit as the normal distance from the surface approaches zero. These streamlines are shown for the blade suction surface at 90% corrected speed in Figure 5.23, where the boundary layer separates just downstream of the root of the shock on the suction surface, with the separation region extending from approximately 40% span to the blade tip. Similarly, Figure 5.24 shows the limiting streamlines for a case at design speed, where the separation line has shifted downstream and now occupies approximately 80% of the span, which is expected as the higher operating speed will have both shifted the shock downstream as well as increased its extent in the spanwise direction. The boundary layer separation near the leading edge can be attributed to the strong adverse pressure gradient associated with the shock and results in a separation bubble that increases blockage and loss in the inducer. This,

coupled with the loss caused by the main flow passing through the shock (which also increases with speed due to increasing shock strength), are at least partially responsible for the dip in efficiency that is observed from 90% to 100% speed in the experimental results. Again, showing that while the formation of the shock is initially beneficial to the compressor's performance, the effect becomes detrimental as the spanwise extent and strength of the shock is increased. This separation also sheds light on the observations made from Figure 4.50, where a region of the pressure field near the blade suction surface showed a higher level of unsteadiness in the fast response pressure data.

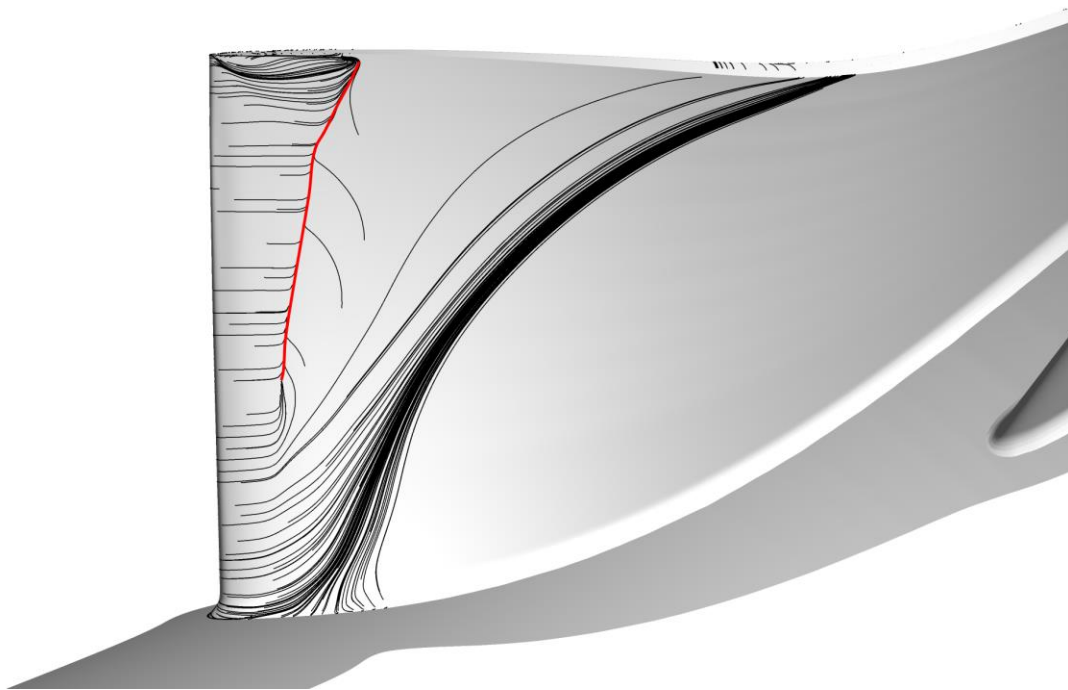


Figure 5.23 Limiting streamlines on the suction surface of the main blade at 90% corrected speed, boundary layer separation indicated by the red line

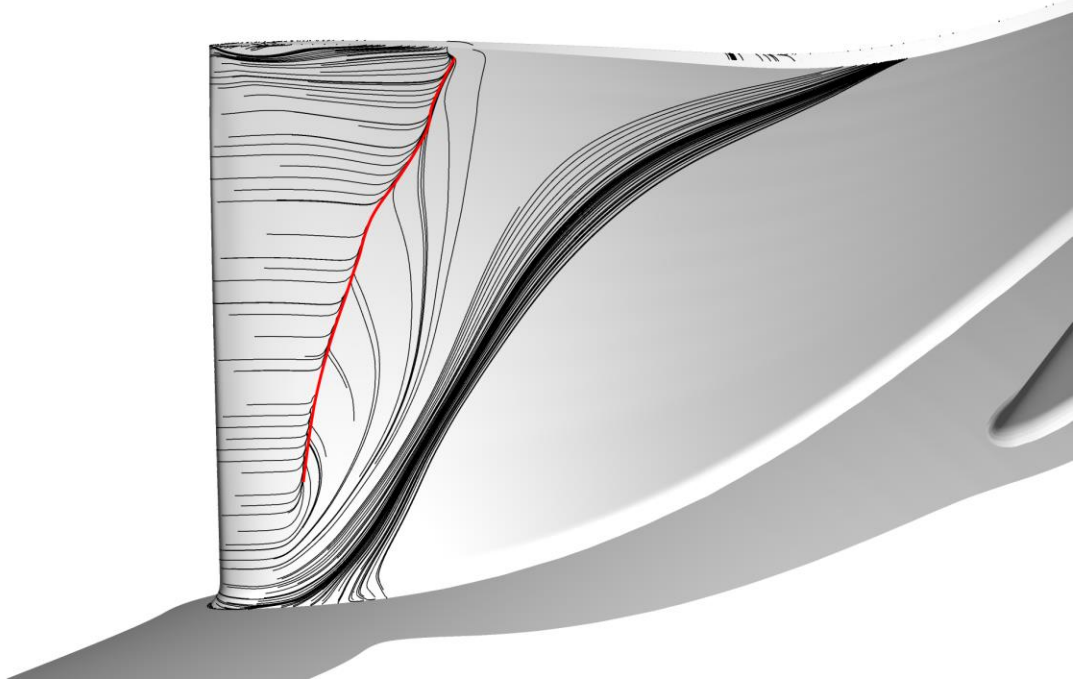


Figure 5.24 Limiting streamlines on the suction surface of the main blade at 100% corrected speed, boundary layer separation indicated by the red line

6. CONCLUSION

6.1 Experimental Data

6.1.1 Transient Data

Transient data were collected for acceleration and deceleration sweeps along two throttle conditions, at mid-choke and at the operating line. These data were then used to show that the static pressure field at the impeller shroud, specifically the unsteadiness thereof, changed significantly in the speed range between 84% and 87% corrected speed, and that the exact speed for which the transition occurred was dependent on both the direction of the sweep (accelerating or decelerating) as well as the throttle position. Further analysis of the unsteady pressure signals showed that the unsteadiness was unstructured in the frequency domain and was primarily composed of frequencies below that of the impeller main blade passing. Also, the sudden decrease in unsteadiness was preceded by an increase in the strength of the blade passing frequency component of the pressure field, indicating that a gradual improvement in the flow quality existed in addition to the more obvious step change. As the speed range associated with the change in flow behavior also corresponds with the impeller's transition from a subsonic to transonic flow regime, the phenomena were associated with the formation of the shock in the inducer passage, as shown by comparisons with one-dimensional Rayleigh flow. The transition speed corresponded with the magnitude of heat transfer, and the relative shifts in transition speed agreed with that expected from the effects of heat transfer on Mach number. Similar trends were also present for the impeller's performance, with the impeller efficiency increasing by nearly 3 points from 80% to 90% corrected speed, and the impeller total pressure ratio showing an inflection point at the transition speed, above which the total pressure ratio was observed to increase at a nearly linear rate compared with the quadratic increase that existed below the transition speed. A bare bead thermocouple located just upstream of the inducer was used to show that the unsteadiness in the shroud pressure field was also associated with a spike in the shroud flow temperature, indicating that the unsteadiness is the result of recirculation in the inducer near the shroud. The transition speed was weakly dependent on the meridional location in the impeller, with Kulites closer to the leading edge experiencing the decrease in unsteadiness at slightly lower speeds than those further downstream. It would appear that the step decrease in unsteadiness in the inducer was the result of

the formation of the shock “shielding” the upstream flow from downstream perturbations. However, it is also possible that some other behavior is resulting in the collapse of the recirculation region, which as a result decreases the blockage in the inducer and allows the shock to expand in the region near the shroud. In either case, the fact that the inducer Kulites show a significantly lower level of turbulence than those further downstream in the impeller and diffuser seems to indicate that the shock does play some role in isolating the inlet from these perturbations. As the inducer is not fully supersonic, the downstream flow would still be able to communicate upstream of the shock, however the effect would be reduced as seen in reference [26]. Further investigation is recommended to determine the degree to which the shock structure affects the recirculation region in the inducer.

Although the transient data do not allow for quantitative statements to be made about the effect of the transition on the compressor’s performance, they show that the performance is changing dramatically in a relatively small speed range and that this phenomenon appears to be related to the transition from subsonic to transonic operation. It is left to the steady data as well as numerical analyses to explain the details leading to the change in behavior.

6.1.2 Steady State Data

To allow for a more detailed analysis of the phenomena observed during speed transients, steady state data were collected along the same two throttle lines as the transient data. However, these data were collected in discrete speed steps of 0.5% corrected speed and only after the compressor had achieved thermal equilibrium, thereby limiting the effects of transients on the observed behavior. With these detailed data available, it was possible to show that the phenomena did in fact correspond closely with the impeller relative Mach number exceeding unity in the inducer. Further analysis of the steady data showed many of the same results observed in the transient flow field, primarily a decrease in the variance of the unsteady pressure field above approximately 85% corrected speed, as well as a dramatic increase in impeller efficiency, which was shown to be closely linked with the decrease in recirculation upstream of the impeller. Some increase in compressor performance with speed is to be expected due to the improved matching between the diffuser and impeller as the speed is increased. However, this change would likely be more of a gradual improvement rather than the sudden change that is observed here. Using the fast response pressure transducers located in the shroud, it is possible to reconstruct visual

representations of the ensemble averaged pressure fields, to observe how the structure of the pressure field changes as the transition speed is crossed. The most notable observation was the presence of a large low-pressure region in the inducer, which was observed to disappear upon the transition to transonic flow. Similar contours showing the rms variation in the pressure field indicated that the region of peak variation shifted downstream at higher speeds, providing further support that the formation of the shock is shielding the flow entering the inducer from the downstream flow. The presence, and later destruction, of the low-pressure region in the inducer was observed to closely correspond with the trend in the static pressure rise and relative diffusion achieved in the inducer, indicating that the increase in impeller efficiency in the 80% to 90% speed range is largely the result of the improvement in the performance of the inducer that occurs after the low-pressure region disappears.

Data were also collected at two different exducer tip clearances, a large clearance of ~7% of the exit blade height and a nominal clearance of ~4%. A comparison of the data at the two clearances indicates that total pressure ratio and impeller efficiency are more sensitive to changes in tip clearance below the transition speed, with the sensitivity decreasing significantly from 85% to 90% corrected speed. As the tip clearance only changes in the exducer of the impeller, it is possible that the decrease in sensitivity is also attributable to the formation of the shock, which, upon formation, would isolate a portion of the inducer from changes in the downstream flow field that result from changing the exducer tip clearance.

An analysis of the stability of the various components of the compressor showed that near the transition speed, the stability of the machine was governed primarily by the inducer, whereas at higher speeds, the diffuser and vaneless space are the destabilizing regions of the compressor.

6.2 Numerical Results

In order to determine the root cause of the observed changes in behavior, additional details of the flow field, beyond what could be obtained experimentally, were required. These details were obtained using a computation model of the compressor, for which simulations were performed at a range of speeds matching the higher loading line in the experimental data. A comparison with the experimental results showed that the overall trend in impeller performance was captured by the numerical model, although the simulated results tended to overpredict the extent of the low-pressure region and its effects at lower speeds. At speeds beyond the transition speed, the model

showed extremely close agreement with experimental data. The inherently unsteady flow condition that exists at lower speeds was likely the cause of the diminished quality of the results for the cases below 85.5% corrected speed. More detailed comparisons showed that, although exaggerated in the numerical results, the model also had a low-pressure region in the inducer similar to that observed in the experimental data. As in the actual compressor, the low-pressure region disappeared from the simulation as the speed was increased. The calculated blockage in the inducer also fell off precipitously after the transition speed was exceeded, which explains the marked improvement in impeller performance observed both experimentally and numerically.

The tip leakage flow near the leading edge was visualized by inserting streamlines into the model in the tip gap region. This showed that at lower speeds, the tip leakage flow in the inducer was highly unstructured and exhibited strong recirculation rather than forming a longitudinal vortex, as would be expected. However, at higher speeds, the tip leakage flow does roll up into a vortex. It is, therefore, concluded that the experimentally observed low-pressure region in the inducer is the result of the recirculating tip leakage flow, which then disappears once the flow forms a vortex. By visualizing the shock in the computational results, the sudden change in performance occurs when the inducer shock extends to the shroud, which then prevents interaction between the incoming flow in the inlet shroud boundary layer and the low momentum tip leakage flow. The blockage upstream of the leading edge is thereby drastically reduced, resulting in a significant increase in the extent of the shock in the region near the shroud.

To determine the effect of the inlet boundary layer, a simulation was performed where the inlet shroud surface had a free-slip boundary condition, preventing the development of a boundary layer. The results of this simulation showed a modest decrease in the blockage in the inducer, but the interaction with the leakage flow was still present, indicating that the more gradual decrease in blockage from 80% to 85% N_c may be due to the decreasing boundary layer thickness whereas the sudden decrease in blockage at the transition speed is likely to be inviscid in nature.

The interactions of the inducer shock with the suction surface boundary layer and tip leakage vortex were also investigated in the numerical model. The results showed no sign of vortex breakdown upon interaction with the shock; however, the main blade suction surface boundary layer separated just downstream of the root of the shock. The spanwise extent of the separation increased with speed, which likely contributes to the deterioration of impeller performance at speeds above 90% N_c .

6.3 Recommendations for Future Work

6.3.1 Experimental Suggestions

In order to further improve understanding of the compressor's behavior near the transition speed, it would be beneficial to collect additional experimental data along a third, higher throttle line. This would allow for an improved understanding of how the stability of the various subcomponents of the compressor change with speed, as the current data only demonstrates the component stability on the choke side of the characteristic, not at lower mass flow rates where stability is more of a concern. Additionally, it may be beneficial to collect steady data at both nominal and larger tip clearances to determine how closely the change in sensitivity is coupled with the transition speed, as the current data set only allows for comparison at 80%, 85%, and 90% corrected speed. Additional resolution in the transition region would be useful. Similarly, conducting surge testing for a narrow range of speeds around the transition speed would provide insights on how the surge behavior of the compressor changes as a result of the transition to a transonic flow regime, which is not available in the existing data set.

The other recommendations would require modifications to the test rig and are made with the understanding that they are not likely to be implemented, at least in the near term. In order to allow for a better understanding of the unsteady pressure field in the rotating domain, it is suggested that unsteady pressure instrumentation be added to the impeller. This additional data would provide an unparalleled view of the flow behavior in the impeller and would be invaluable, however the rotational speeds involved would make instrumenting the impeller in such a way difficult and perhaps impossible due to mechanical concerns.

As the cause of the instability near 85% speed is believed to be a result of the blockage at the impeller leading edge, it is suggested to use either bleed or flow injection in this region to mitigate the extent of the blockage and allow for increased operating range. Numerous studies have shown that both bleed and flow injection in the inducer can result in drastic increases in surge margin, and it is believed that this test article is an excellent candidate for such techniques. Similarly, the addition of casing treatment over the inducer could also improve the stable operating range, although typically with a corresponding penalty in efficiency.

6.3.2 Numerical Suggestions

As with the experimental suggestion of increased unsteady instrumentation, a better understanding of the time varying flow field within the impeller is invaluable. It is, therefore, recommended that unsteady simulations be conducted near the transition speed in order to understand the nature of the instability in the inducer. Finally, rather than undergoing the costly and time consuming modifications to the shroud to experimentally implement flow injection or bleed in the inducer, these features could be added to the computational model to both determine their effectiveness or to optimize the design before undergoing any modifications to the test article.

APPENDIX

Due to the unique capability of the Honeywell SSCC research compressor to adjust the exducer tip clearance during testing, it is critically important to have an accurate measurement of the impeller axial tip clearance to ensure consistency when taking data as well as to allow safe operation of the compressor. During testing the axial cap probes located in the shroud near the impeller exit became unreliable when operating at speeds above 90% N_c , due to the high temperatures present in the impeller exit. In order to continue collecting data at speeds at and above 90% N_c it was necessary to develop a correlation between a number of parameters and the axial tip clearance. This appendix will outline the method used to generate the correlation.

Observations of the behavior of the axial tip clearance during testing showed that it primarily varies as a function of speed and temperature, increasing speed results in transiently tighter clearances, however once a stable speed is reached the clearance decreases as the impeller shroud heats up and expands. Therefore, the parameters selected to be used in the correlation were the compressors mechanical speed, N , the shroud metal temperature, T_{sh} , the clearance measured at the impeller knee and inducer, CL_K and CL_R (which remain operational for the full speed range due to the lower temperature in that region), and lastly to capture the motion of the impeller resulting from adjusting the tip clearance, the relative axial location of the impeller was also used, LVDT (linear variable differential transformer). A general form of the correlation is given in equation A.1, where P_i represents the i -th parameter and the a 's and b 's are constants.

$$\begin{aligned}
 &CL_correlation \\
 &= \llbracket a_1 \cdot P \rrbracket _i^{(b_i)} \cdot P_j^{b_j} \cdot \dots \cdot P_k^{(b_k)} + \llbracket a_2 \\
 &\cdot P \rrbracket _l^{(b_l)} \cdot P_m^{(b_m)} \cdot \dots \cdot P_n^{(b_n)} + \dots
 \end{aligned} \quad (A.1)$$

In order to determine the coefficients that provided the closest fit between the approximated and measured clearance, as well as to determine the best form of the correlation, a genetic optimization algorithm was used.

The genetic algorithm begins with an initial “population” of sets of values for the coefficients and powers in the correlation, then based on which members of the population give the best performance, in this the smallest error relative to the experimental data, those members of the population are selected to survive and form the basis of the next “generation”. As with biological evolution the best performing members are crossed in an attempt to create an even better

set of values in the next generation. Random “mutations” are also introduced to help ensure that the results do not hit a dead end due to a poor selection of random values in the initial generation. Over the course of thousands of generations, the algorithm will eventually converge on an optimum family of coefficients, out of which the set of coefficients giving the best performance is selected. This procedure was performed for a variety of sets and combinations of parameters, and eventually the form given in equation A.2 was selected, where the values of the coefficients and exponents are listed in table A.1.

$$CL_correlation = a \cdot CL_K^{(b_1)} \cdot (N/48000)^{(b_2)} \cdot LVDT^{(b_3)} \quad (A.2)$$

Table A.1 Values of coefficients and exponents used in the final correlation

<i>a</i>	<i>b₁</i>	<i>b₂</i>	<i>b₃</i>
1.4185	1.4018	-0.0377	-0.7355

In order to obtain these values, a training set of data was required. Steady data points would not provide the necessary information to capture changes in clearance associated with speed transients, therefore transient clearance data recorded by the health monitoring computer was used to fit the correlation. This allowed the genetic algorithm to be run for data from multiple tests at a wide range of clearances at both steady and transient conditions. After the genetic algorithm found an optimum set of coefficients those were then used to calculate the approximate axial clearance for steady data for several speedlines for both the nominal and open clearance conditions. The results of this are shown in Figure A.1, where the color of the markers represents the deviation from the measured tip clearance. It should be observed that the correlation performs best at higher speeds, which is a result of the correlation being developed using more high speed data, as this is the region where the axial cap probes were no longer functional. The final correlation gave errors of less two thousandths at speeds above 90%, which was considered sufficient.

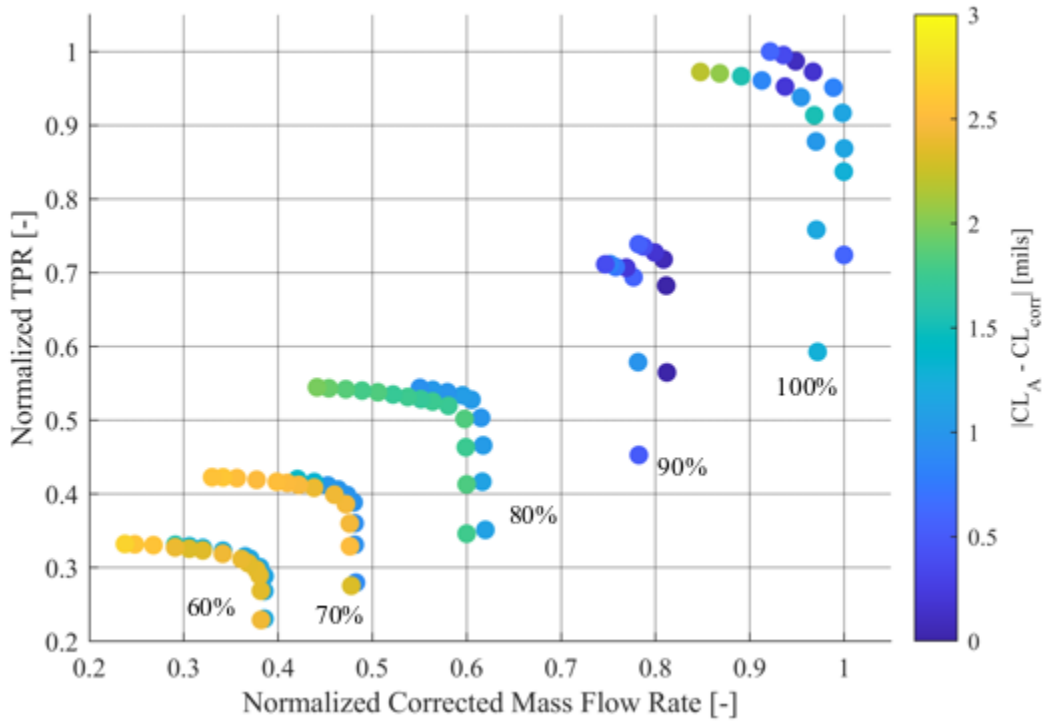


Figure A.1 Compressor total pressure ratio map showing the error in the calculated axial tip clearance

REFERENCES

- [1] C. Rodgers, “The Centrifugal Compressor Inducer,” in *Volume 1: Turbomachinery*, Stockholm, Sweden, Jun. 1998, p. V001T01A009, doi: 10.1115/98-GT-032.
- [2] K. Yamada, M. Furukawa, M. Inoue, and K. Funazaki, “Numerical Analysis of Tip Leakage Flow Field in a Transonic Axial Compressor Rotor,” p. 8.
- [3] W. H. Hoffman and J. Ballman, “Some aspects of tip vortex behavior in a transonic turbocompressor,” *ISABE Pap.*, vol. 1223, p. 2003, 2003.
- [4] S. Schlechtriem and M. Lötzerich, “Breakdown of Tip Leakage Vortices in Compressors at Flow Conditions Close to Stall,” presented at the ASME 1997 International Gas Turbine and Aeroengine Congress and Exhibition, Jun. 1997, doi: 10.1115/97-GT-041.
- [5] J. P. Johnston and S. A. Eide, “Turbulent Boundary Layers on Centrifugal Compressor Blades: Prediction of the Effects of Surface Curvature and Rotation,” *J. Fluids Eng.*, vol. 98, no. 3, pp. 374–381, Sep. 1976, doi: 10.1115/1.3448327.
- [6] H. R. Hazby and L. Xu, “Role of Tip Leakage in Stall of a Transonic Centrifugal Impeller,” in *Volume 7: Turbomachinery, Parts A and B*, Orlando, Florida, USA, Jan. 2009, pp. 1245–1253, doi: 10.1115/GT2009-59372.
- [7] R. Hunziker, H.-P. Dickmann, and R. Emmrich, “Numerical and experimental investigation of a centrifugal compressor with an inducer casing bleed system,” *Proc. Inst. Mech. Eng. Part J. Power Energy*, vol. 215, no. 6, pp. 783–791, Jan. 2001, doi: 10.1243/0957650011538910.
- [8] M. Kaneko and H. Tsujita, “Mechanism of Blockage Generation in Transonic Centrifugal Compressor at Design and Off-Design Conditions,” presented at the ASME Turbo Expo 2015: Turbine Technical Conference and Exposition, Aug. 2015, doi: 10.1115/GT2015-43126.
- [9] H. Hayami, Y. Senoo, and H. Ueki, “Flow in the Inducer of a Centrifugal Compressor Measured With a Laser Velocimeter,” *J. Eng. Gas Turbines Power*, vol. 107, no. 2, pp. 534–540, Apr. 1985, doi: 10.1115/1.3239766.
- [10] F. Lou, J. C. Fabian, and N. L. Key, “Stall Inception in a High-Speed Centrifugal Compressor During Speed Transients,” *J. Turbomach.*, vol. 139, no. 12, p. 121004, Dec. 2017, doi: 10.1115/1.4037759.

- [11] S. Ibaraki, M. Furukawa, K. Iwakiri, and K. Takahashi, “Vortical Flow Structure and Loss Generation Process in a Transonic Centrifugal Compressor Impeller,” p. 10, 2007.
- [12] S. Ibaraki, K. Sumida, and T. Suita, “Design and Off-Design Flow Fields of a Transonic Centrifugal Compressor Impeller,” Feb. 2010, pp. 1375–1384, doi: 10.1115/GT2009-59986.
- [13] H. Zhao, Z. Wang, H. Yu, C. Jiang, and G. Xi, “Numerical Investigation of Shock Effects on Performance and Flow Field in a Transonic Centrifugal Impeller,” presented at the ASME Turbo Expo 2016: Turbomachinery Technical Conference and Exposition, Sep. 2016, doi: 10.1115/GT2016-56488.
- [14] C. Hah, D. C. Rabe, and A. R. Wadia, “Role of Tip-Leakage Vortices and Passage Shock in Stall Inception in a Swept Transonic Compressor Rotor,” in *Volume 5: Turbo Expo 2004, Parts A and B*, Vienna, Austria, Jan. 2004, pp. 545–555, doi: 10.1115/GT2004-53867.
- [15] O. Thomer, E. Krause, and W. Schroder, “Interaction between Longitudinal Vortices and Normal and Oblique Shocks,” in *Vortex Dominated Flows: A Volume Celebrating Lu Ting’s 80th Birthday*, Singapore, SINGAPORE: World Scientific Publishing Co Pte Ltd, 2005.
- [16] S. Ibaraki, T. Matsuo, H. Kuma, K. Sumida, and T. Suita, “Aerodynamics of a Transonic Centrifugal Compressor Impeller,” *J. Turbomach.*, vol. 125, no. 2, pp. 346–351, Apr. 2003, doi: 10.1115/1.1540117.
- [17] H. Higashimori, K. Hasagawa, K. Sumida, and T. Suita, “Detailed Flow Study of Mach Number 1.6 High Transonic Flow With a Shock Wave in a Pressure Ratio 11 Centrifugal Compressor Impeller,” *J. Turbomach.*, vol. 126, no. 4, pp. 473–481, Oct. 2004, doi: 10.1115/1.1791645.
- [18] W. W. Copenhaver, S. L. Puterbaugh, and C. Hah, “Unsteady Flow and Shock Motion in a Transonic Compressor Rotor,” *J. Propuls. Power*, vol. 13, no. 1, pp. 17–23, Jan. 1997, doi: 10.2514/2.5145.
- [19] M. D. Langford, A. Breeze-Stringfellow, S. A. Guillot, W. Solomon, W. F. Ng, and J. Estevadeordal, “Experimental Investigation of the Effects of a Moving Shock Wave on Compressor Stator Flow,” *J. Turbomach.*, vol. 129, no. 1, pp. 127–135, Jan. 2007, doi: 10.1115/1.2370745.
- [20] B. H. K. Lee, “Oscillatory shock motion caused by transonic shock boundary-layer interaction,” *AIAA J.*, vol. 28, no. 5, pp. 942–944, May 1990, doi: 10.2514/3.25144.

- [21] Skoch and R. Moore, “Performance of two 10-lb/sec centrifugal compressors with different blade and shroud thicknesses operating over a range of Reynolds numbers,” presented at the 23rd Joint Propulsion Conference, San Diego, CA, U.S.A., Jun. 1987, doi: 10.2514/6.1987-1745.
- [22] P. A. Eynon, A. Whitfield, M. R. Firth, A. J. Parkes, and R. Saxton, “A Study of the Flow Characteristics in the Inducer Bleed Slot of a Centrifugal Compressor,” in *Volume 1: Turbomachinery*, Birmingham, UK, Jun. 1996, p. V001T01A080, doi: 10.1115/96-GT-262.
- [23] F. B. Fisher, “Application of Map Width Enhancement Devices to Turbocharger Compressor Stages,” *SAE Trans.*, vol. 97, pp. 1303–1310, 1988.
- [24] F. Lou, J. C. Fabian, and N. L. Key, “Interpreting Aerodynamics of a Transonic Impeller from Static Pressure Measurements,” *International Journal of Rotating Machinery*, 2018. <https://www.hindawi.com/journals/ijrm/2018/7281691/abs/> (accessed Nov. 18, 2019).
- [25] N. A. Cumpsty, *Compressor aerodynamics*, no. BOOK. Longman Scientific & Technical, 1989.
- [26] A. Fatsis, S. Pierret, and R. Van den Braembussche, “Three-Dimensional Unsteady Flow and Forces in Centrifugal Impellers With Circumferential Distortion of the Outlet Static Pressure,” *J. Turbomach.*, vol. 119, no. 1, pp. 94–102, Jan. 1997, doi: 10.1115/1.2841015.
- [27] R. A. Berdanier, N. R. Smith, J. C. Fabian, and N. L. Key, “Humidity Effects on Experimental Compressor Performance—Corrected Conditions for Real Gases,” *J. Turbomach.*, vol. 137, no. 3, Mar. 2015, doi: 10.1115/1.4028356.
- [28] F. Lou, H. M. Harrison, J. C. Fabian, N. L. Key, D. K. James, and R. Srivastava, “Development of a Centrifugal Compressor Facility for Performance and Aeromechanics Research,” in *Volume 2D: Turbomachinery*, Seoul, South Korea, Jun. 2016, p. V02DT42A005, doi: 10.1115/GT2016-56188.
- [29] Matthew Fuehne, “Experimental and Numerical Investigation of Tip Clearance Effects in a High-Speed Centrifugal Compressor,” MSA, Purdue University, West Lafayette, Indiana, 2020.
- [30] J. R. Brossman, “An investigation of rotor tip leakage flows in the rear-block of a multistage compressor,” Thesis PhD--Purdue University, 2012.
- [31] Z. S. Spakovsky, “Backward Traveling Rotating Stall Waves in Centrifugal Compressors,” p. 15, 2002.

- [32] T. R. Camp and I. J. Day, “1997 Best Paper Award—Turbomachinery Committee: A Study of Spike and Modal Stall Phenomena in a Low-Speed Axial Compressor,” *J. Turbomach.*, vol. 120, no. 3, pp. 393–401, Jul. 1998, doi: 10.1115/1.2841730.